Optimized scanning procedures for 4D CT data acquisition in radiation therapy

Gabriela Stroian

Master of Science

Medical Physics Unit

McGill University

Montreal, Quebec

June 2005

A thesis submitted to McGill University in partial fulfilment of the requirements of the degree of Master of Science in Medical Radiation Physics

Your file Votre référence
ISBN: 978-0-494-22769-5
Our file Notre référence
ISBN: 978-0-494-22769-5

To Aurelian, for his unconditional love and support.

ACKNOWLEDGEMENTS

It is a pleasure to thank all the people who made this thesis possible.

I would like to thank *Dr. Jan Seuntjens*, the best supervisor I could have wished for, for encouragement, sound advice, good teaching and lots of good ideas.

I am grateful to *Emily Heath* for being a friend, assisting with experimental setup and helping with many scientific and less scientific discussions. *Dr. François DeBlois* and *Dr. Slobodan Devic* are thanked for their guidance in the "jungle" of CT data transfer. Thanks are due also to *Robin Van Gils*, for assistance during measurements with the Polaris system and *Vlad Bobeş*, *Joe Larkin* and *Pierre Léger* for support in making Rando "breathe". Thanks especially to *Sharon Swan* and *Dinesh Parmar* for their patience in teaching me how to use the CT scanner and dealing with all my questions. I am thankful to *Margery Knewstubb* for helping the department to run smoothly and for assisting me in many different ways. In my office I was surrounded by knowledgeable and friendly people who helped me daily. I am grateful to *Geneviève* for all the advice, entertainment and caring she provided. Life would not have been the same without my classmates and friends *Caroline, Clarisse, Sara, Charmaine, Danielle, Matthieu* and *Rumtin.* I am grateful to them for providing a stimulating and fun environment in which to "grow" as medical physicists.

Most of all, I would like to thank those closest to me, whose presence helped make the completion of my M.Sc. studies possible: *my parents*, for their unconditional love and absolute confidence in me and *Aurelian* for his endless love, encouragement and understanding.

ABSTRACT

The goal of conformal radiation techniques is to improve local tumor control through dose escalation to target volumes while at the same time sparing surrounding healthy tissue. Accurate target volume delineation is essential in achieving this goal to avoid inadequate tumor coverage and/or irradiation of an unnecessary volume of healthy tissue. Respiratory motion is known to be the largest intra-fractional organ motion and the most significant source of uncertainty in treatment planning for chest lesions. A method to minimize effects of respiratory motion is to use four-dimensional (4D) radiotherapy.

A novel scanning procedure for 4D CT data acquisition is described in this work. Three single-slice helical scans are acquired simultaneously with the real-time tracking of several markers placed on a moving phantom. At the end of the three scans, CT data is binned into different respiratory phases according to the externally recorded respiratory signal and the scanned volume is reconstructed for several respiratory phases. The 4D CT images obtained show an overall improvement when compared to conventional CT images of a moving phantom.

ABRÉGÉ

La radiothérapie conformationnelle se propose d'améliorer le contrôle local de la tumeur en permettant de délivrer une dose élevée au volume cible tout en épargnant le plus possible les tissus sains et les organes à risque environnants. La délimitation précise du volume à irradier est essentielle pour éviter la couverture inadéquate de la tumeur et/ou l'irradiation inutile des tissus sains. Le déplacement des organes internes induit par la respiration est le plus important des déplacements intra-fraction et la source d'incertitude prédominante dans la planification du traitement pour les lésions thoraciques. La radiothérapie 4D est une méthode utilisée pour alléger les problèmes posés par la respiration en radiothérapie.

Dans cette thèse, une nouvelle technique scanographique pour l'acquisition des images scanner 4D est décrite. Trois acquisitions hélicoïdales sont faites avec un scanner monocoupe, pendant que des marqueurs placés sur le torse d'un phantome anthropomorphique sont continûment localisés par un système à infrarouge. A la fin des trois acquisitions, les images sont classées conformément à leur phase dans le cycle respiratoire et le volume scanné est reconstruit pour différentes phases respiratoires. Les images obtenues avec la scanographie 4D sont nettement supérieures qualitativement aux images obtenues avec la scanographie classique.

TABLE OF CONTENTS

LIST OF TABLES

LIST OF FIGURES

CHAPTER 1
INTRODUCTION

The advent of three-dimensional conformal radiotherapy (3DCRT) and intensity modulated radiotherapy (IMRT) has provided the tools required to shape radiation dose distribution with high precision, such that irregularly shaped tumor volumes can be treated with therapeutic doses while sparing the surrounding healthy tissues as much as possible. A prerequisite for high precision dose delivery is a high precision of targeting.

In the past few decades, 3D imaging modalities such as computed tomography (CT), magnetic resonance imaging (MRI) and positron emission tomography (PET) have allowed reasonably precise localization of the *gross tumor volume* (GTV) for many sites and for most sensitive structures. However, the location of microscopic extension of the tumor around the GTV remains uncertain. The concept of *clinical target volume* (CTV) surrounding the GTV with a margin for microscopic invasion is a best-guess scenario to overcome this uncertainty. Because the patient is not set up identically from day to day, and the position and shape of organs may shift and deform, a volume larger than the CTV, called the *planning target volume* (PTV), has to be treated. The margin of the PTV around the CTV has to account for setup uncertainty and organ motion.

In the era of conformal and intensity-modulated radiotherapy, there is an increased desire to escalate tumor dose in order to improve tumor control probability

and to decrease normal tissue dose in order to reduce treatment-related complications. Generally, increased fractionation provides a therapeutic advantage between tumor control and late complications, in that fractionation spares late-responding normal tissues more than early-responding tumors. In the linear-quadratic (LQ) formalism, fractionation spares tissues with a low α/β ratio (late-responding tissues) more than tissues with a high α/β ratio (early-responding tissues, typical of most tumors). Recent evidence indicates that some sites may respond better to higher doses per fraction. The suggestion for prostate cancers is that the α/β ratio for tumor control is considerably less (1.2 Gy) than typical values for tumors (> 8 Gy) and more comparable to values in surrounding late-responding normal tissues. Therefore, hypo-fractionated radiotherapy or high-dose-rate brachytherapy for prostate should improve tumor control and reduce normal tissue complications [14]. For late effects in lung, it is widely accepted that the value of α/β ratio is close to 3 Gy and several studies have shown a survival advantage for dose-per-fraction escalation [85] and a correlation of radiation pneumonitis with mean lung dose, volume of lung receiving more than a threshold dose (typically 20 or 30 Gy) and normal tissue complication probability [41, 118].

Thus, there is clinical evidence that technologies that allow an increased dose to the tumor whilst sparing healthy tissue will improve the balance between complications and cure. There are two general strategies that can potentially achieve this objective [74]:

1. Reduce uncertainty in the extent of microscopic disease (*i.e.*, CTV to GTV).

2. Reduce patient setup uncertainty and identify and reduce organ motion (*i.e.*, PTV to CTV).

The combination of these strategies will reduce the margins around the GTV.

1.1 Reduction of uncertainties in the extent of microscopic disease

Reducing the uncertainty of microscopic extension of the tumor is a difficult task, but imaging systems continue to improve with respect to sensitivity and specificity of diagnosis. CT alone, or fused with other imaging modalities [91], is the gold standard for delineation of most tissue structures in radiation therapy planning. Improvement in CT contrast agents has allowed much better definition of tumor boundaries and CT simulation with 3D treatment planning is now conventional practice in most radiotherapy centers. However, even with dedicated 3D imaging systems common in most clinics and a generation of radiation oncologists trained in their use, there is considerable CTV variation for prostate [143] and breast cancer [44] as well as large GTV variation for lung [35, 144] and esophageal [138] cancer.

The ability to differentiate cancer from normal tissue and non-cancerous pathologies has improved greatly with the advent of MRI, which is now the modality of choice for delineating most central nervous system malignancies [4]. Magnetic resonance spectroscopy (MRS) is being used to identify the GTV within the CTV in prostate cancer [27] and can likely be applied to many other tumor sites [102].

The role of PET will be greatly enhanced by the new generation of PET/CT scanners from which fully correlated PET and CT images are obtained. PET images will be able to delineate the extents of the GTV and CTV with much more specificity. Then, the GTV will be defined as that region where the probability of occupancy

by the tumor approaches 100%, with the CTV touching the boundary where this probability approaches zero.

As CTV margins around disease sites are reduced and doses are escalated, there must be careful monitoring to determine whether the patterns of failure are changing. Smaller margins will result in more motion blurring of the dose inside the target volume and without image-based follow-up correlated to the treatment plan to provide in vivo recurrence detection, failures could be interpreted as a consequence of inadequate dose instead of inadequate margin [65].

Shrinking the margins for the sake of shrinking the margins when there is no critical sensitive tissue to spare might lead to a decreased therapeutic ratio. *Conformal avoidance* is the complement to *conformal therapy.* The strategy of conformal avoidance is to treat the tumor with generous treatment volumes, but to carve out dose-limiting regions around sensitive structures where there is no possibility of tumor extensions. *Conformal therapy* should be used when the GTV is well delineated and the CTV extension is small. *Conformal avoidance* should be used when the GTV is not well delineated or the CTV is large (*e.g.*, in head-and-neck radiotherapy when sparing uninvolved parotid glands, auditory apparatus, mucosa and larynx). This strategy was not possible before the advent of IMRT, because it was extremely difficult to produce arbitrarily shaped treatment volumes with standard uniform field irradiation. However, carving out regions around sensitive structures will result in placing high gradients near the sensitive structures so, in order to have confidence in this strategy, the second major objective for precise delivery of radiotherapy, the

reduction of setup uncertainty and organ motion, has to be met in order to achieve accurate dose delivery.

1.2 Reduction of setup uncertainties and organ motion

The need to guarantee that the CTV is indeed being treated is as important as defining the CTV. Just as the margin extension around the GTV to form the CTV should be based on the probability of GTV inclusion, so should the definition of the PTV be based on the probability of CTV extension.

The patient anatomy and position during the course of radiation therapy usually vary to some degree from those used for therapy planning purposes. This is mainly due to patient movement, uncertainties in patient positioning and organ motion. Consequently, the actual received dose distribution differs from the planned dose distribution. Failure to properly define the PTV will jeopardize the curative intent of the treatment through either inadequate tumor coverage, or irradiation of an unnecessary volume of healthy tissue, or both. So, *setup uncertainties* and *organ motion* degrade the precision with which radiotherapy can be delivered.

1.2.1 Setup uncertainties

Setup uncertainties are related to patient-beam positioning in reference to treatment machine's coordinate system. Mechanically related uncertainties should be dealt with by an improved mechanical stability of the treatment machine whereas the patient should be set up for treatment in as reproducible a manner as possible. Patient movement and variations in patient position can be reduced via immobilization techniques and careful daily repositioning of the patient using planar (*portal* or *kilovoltage*) *images*, *ultrasound devices* and *kilovoltage*, *megavoltage* and *cone-beam*

CT scanners. Planar images are more amenable for use with rigid structures such as encountered in the sinus, whereas ultrasound and CT scanners are able to account for non-rigid setup variations.

Portal images are typically acquired on a linear accelerator with radiographic film or electronic portal imaging detector (EPID) systems [3, 134]. EPIDs are an improvement over film, because they are more efficient and offer more latitude for image enhancement, but even the best EPID image will be inferior to a typical *kilovoltage radiograph*, because there is less tissue contrast in a megavoltage image [103].

Planar images (portal or kilovoltage) are difficult to interpret because they are not directly correlated to 3D CT image sets and out-of-plane rotations of the patient are not as readily evident as translations [106]. However, 3D conformal radiotherapy planning systems can augment the poor image quality of planar radiographs and improve their comparability with the 3D CT image sets by the construction of digitally reconstructed radiographs (DRR), from CT [123] or magnetic resonance [105] image sets, in the same treatment setup and beam position as the radiographs.

Ultrasound images were among the first to be used to determine the patients internal anatomy at the time of treatment. A two-dimensional ultrasound beam can be used for scanning in the orthogonal dimension [63] or, by optically tracking the position of the transducer, a partial 3D ultrasound image of the region of interest can be rendered [13]. The ultrasound image can be compared to the planning CT scan to determine if the patients target volume is in the right place. Thus far, ultrasound systems have been used to determine the position of the prostate just

before treatment [121]. This technique could potentially be applied to other sites, but its general utility will be limited by problems associated with limited penetration through fat, bone or lung.

For some time, megavoltage image detectors have been used to acquire a set of projections around the patient so that *megavoltage CT* (MVCT) images are reconstructed [120, 137]. Cone-beam MVCTs could potentially be obtained from conventional linacs using portal imaging systems, although the dose needed to produce the same image quality would be higher [48]. There are a number of advantages of MVCT over planar megavoltage portal images: MVCT images are fully three-dimensional, have better soft-tissue contrast and are easier to compare with planning CT images.

It is possible to put a conventional CT scanner in the treatment room and to acquire a *kilovoltage CT* (kVCT) scan at the time of treatment [48, 81, 140]. The tissue contrast visible at a given resolution and given dose for a conventional kVCT is superior to that for an MVCT [48, 113].

It is also possible to put a kilovoltage X-ray tube and a detector array on board the linac to acquire CT scans. Because the gantry rotation of a linac is much slower than a CT ring gantry, flat-panel detectors are more practical from the perspective of throughput, so that a whole volume may be acquired with one or a few rotations. These so-called *cone-beam CT* scanner systems do not have as favorable imaging properties as conventional kVCT scanners, because there is more scatter arriving at the detector that degrades the image contrast [128].

1.2.2 Organ motion

Organ motion refers to the variation of the position and shape of internal organs relative to patient's bony anatomy. The various types of organ motion and deformation are usually grouped into three categories: *patient position-related*, *inter-fractional* and *intra-fractional* [62].

Organ motion and deformation related to changes in patient's position. This kind of motion/deformation arises when patient's position during treatment planning differs from patient's position during treatment delivery. Reasons for this are the use of immobilization devices or combination of prone/supine/lateral decubitus positions used during planning and delivery. Position-related organ motion/deformation may also occur in hadron therapy facilities that have fixed horizontal beam lines and where patients are often treated in a seated or standing position while the planning scan is acquired in a prone/supine position.

Even if the position-related movement of intracranial tissues is negligible, significant changes in organ position can be found in thorax and abdominal regions. In addition to organ motion, the thickness and shape of the surrounding internal structures change and this affects the radiation path length.

Position-related motion/deformation can be minimized if patient's planning scan is performed while the patient is immobilized and in the treatment position.

Inter-fraction organ motion and deformation. This kind of motion/deformation occurs when the CTV position changes on a fraction-to-fraction level and is mainly associated with organs that are part of or adjacent to the digestive system.

Changes in the patient's condition, such as weight gain/loss, can also affect the relative position of the CTV. The magnitude of the inter-fraction motion was studied as a function of daily bowel, bladder and rectum filling differences for gynecological [16], prostate [133, 160] and bladder [87, 139] tumors.

There are several ways to minimize the effect of inter-fraction motion, ranging from simple and unobtrusive to complicated and quasi-invasive. The simplest approach consists in choosing patient's optimal position and immobilization. The treatment time should not be excessive and one should ensure that the patient is comfortable in the treatment position. A preparative routine to reduce gastrointestinal, genitourinary and any other organ motion caused by physiologic changes should be systematically used.

Various imaging systems are used for *daily CTV localization* in order to verify that the delivery is carried out as planned: portal, kilovoltage and ultrasound images and kilovoltage, megavoltage and cone-beam CT scans. Tumor movements cannot usually be assessed directly by mega-voltage portal imaging since the soft tissue structures involved are generally not visible. By implantation of radiopaque markers, in or near the CTV, the internal motion can be visualized and this enables on-line positioning corrections [92]. However, this is a highly invasive procedure and there is a potential uncertainty in the migration of the implanted markers between the time they are located in the planning CT study and the time they are used for targeting.

An off-line strategy for constructing *patient-specific PTV*s was investigated for prostate cancer cases [156]. At the beginning of treatment, daily CT scans and portal images were obtained to assess target motion (1 and 2 weeks of daily CT scans for

conventional and IMRT plans, respectively). Using these scans, a patient-specific confidence-limited PTV (cl-PTV) is constructed. This cl-PTV eliminates the effect of the systematic component of the target motion and compensates for the patient-specific random target mobility. The use of this technique for 30 prostate cancer patients showed that, compared to the conventional PTV, the cl-PTV margin can be reduced, on average, by a factor of two, while maintaining the same dosimetric criterion [156].

Intra-fraction organ motion and deformation. This motion/deformation occurs while the patient is being irradiated and can be caused by the respiratory, skeletal, muscular, cardiac and gastrointestinal systems. Respiratory and cardiac motion are the main contributors to intra-fraction motion, which affects mainly organs of the thorax and abdomen. Studies dealing with the quantification of intra-fraction motion of prostate [79], kidneys [115, 136], liver [136], pancreas [15, 136], diaphragm [59, 19] and lung tumors [30, 111] have been reported.

Of all causes determining intra-fraction motion/deformation, much research and development has been directed towards accounting for respiratory motion. *Respiratory motion is known to be the largest intra-fractional organ motion and the most significant source of uncertainty in treatment planning for thorax and upper abdomen.* Respiratory motion affects all tumor sites of the thorax and abdomen – lungs, esophagus, liver, pancreas, breast, prostate and kidneys are known to move with breathing.

Breathing motion observations have been distinguished by posture (prone, supine, lateral decubitus), breathing type (chest or abdominal) and depth of respiration (shallow, normal, deep) [51]. Organ motion caused by breathing is potentially most

severe in the thorax where respiratory excursions, mainly due to muscular contraction of the diaphragm and abdominal muscles, move parts of the lung and liver appreciably [5, 114]. The greatest thoracic displacements were observed for the diaphragm, in the superior-inferior (SI) direction, with mean values between inspiration and expiration of 34.3 ± 20.4 mm [36]. During a quiet respiration cycle, the average ventilatory excursion of the diaphragm can approach 2.5 cm [60] and the lung volume typically changes by 20-25%; during full inspiration, the increase in lung volume is approximately 3-4 times that of normal breathing. The prostate may also move during breathing: patients in the prone position seem to have a larger range of prostate motion due to breathing compared to patients in supine position [21]. Generally, abdominal organ motion is in the SI direction, with no more than 2 mm displacement in the anterior-posterior (AP) and right-left (RL) directions [19, 59].

Lung tumor motions follow complicated 3D tracks and generally show a much greater variation in the trajectory of motion. The amount by which a lung tumor moves can vary widely, no correlation being found between the occurrence and magnitude of tumor motion and pulmonary function or tumor size and location [148]. In general, RL displacements are greatest for tumors near the heart or aorta [111] and the largest SI movements are related to the action of the diaphragm [36]. Shimizu *et al.* [124] reported average SI displacements of 6.2 mm (range from 2.4 to 11.3 mm) and 9.1 mm (range from 3.4 to 24.0 mm) for tumors of upper/middle and lower lobe, respectively. The same study showed that AP movement was less than 10 mm in most cases, but it was as large as 24 mm for a tumor in the lower lobe. Ross *et*

al. [111] reported significant lateral motion with cardiac contraction (average of 9.2 mm) for tumors located adjacent to the heart or aorta.

Therefore, there are no general patterns of respiratory behavior that can be assumed for a particular patient prior to observation and treatment. The many individual characteristics of breathing (quiet vs. deep, chest vs. abdominal, healthy vs. compromised) and the many motion variations associated with tumor location and pathology lead to distinct individual patterns in displacement, direction and phase of tumor motion. Therefore, ideally, *the respiratory motion pattern for each individual patient should be assessed prior to treatment* [51].

A number of techniques were investigated that aim to synchronize the diagnostic, planning and treatment procedures with breathing. These include *elimination/minimization* (shallow breathing, breath holding, respiratory gating), *correction* and *incorporation* (slow CT, real-time tumor tracking, 4D radiotherapy) *schemes.* An overview of these techniques will be given in Chapter 3.

1.3 Summary and thesis structure

Differences between the intended and the actual dose distribution within the CTV are caused by variations in the CTV position and shape during radiotherapy treatments. Various factors, including setup error and organ motion, as well as physical and geometric penumbra, limit the precision with which radiotherapy can be delivered. Where possible, setup uncertainty and organ motion should be reduced, but where not possible, treatment planning systems should include an error analysis based on the CTV positional variance, so that expected dose distributions and dose-volume histograms can be determined for the target volumes.

External setup and internal organ movement/deformation consist each of a systematic and a random component. In principle, systematic deviations of an individual patient can be estimated during the first few fractions and off-line corrections can be applied for subsequent irradiations [8, 155]. Both systematic and random setup deviations can be reduced to negligible values if on-line corrections are applied: patient position is verified at each fraction and, if necessary, corrections are applied before the remaining dose is given [24]. At the moment, however, on-line correction procedures are too time-consuming to be routinely used in clinical practice.

Although *respiratory motion is most often the largest source of treatment planning errors in thorax and upper abdomen*, organ motion/deformation due to cardiac motion, swallowing and stomach/bladder/bowel/rectal filling are also of importance. Other important errors, particularly for lung tumors, are set-up errors and GTV and CTV definition variations. Errors related to GTV/CTV definition variations may be one order of magnitude larger than that of respiration-induced motion. Also, set-up errors for lung [31, 45] and breast cancer [38, 39] may be of the same or a higher order of magnitude than respiratory-induced motion. Furthermore, patients may involuntarily change their position during a radiation treatment session because of discomfort or a prolonged treatment session, possibly leading to tumor target movement out of the radiation field [20].

This work is structured in two main parts. The first part consists of an *extensive review* of the effects of the respiratory motion in radiotherapy (Chapter 2) as well as the various strategies used to minimize these effects (Chapter 3). The second part

describes the implementation of an optimized scanning procedure for 4D CT data acquisition (Chapters 4 and 5).

Chapter 2 details the effects of respiratory motion in imaging (*Section 2.1*), treatment planning (*Section 2.2*) and radiation delivery (*Section 2.3*). *Chapter 3* describes the various strategies used to alleviate the effects of respiratory motion during radiotherapy: minimization of the respiratory motion itself (*Section 3.2*), correction of organ motion artifacts in the CT systems and incorporation of the respiratory motion into the imaging, planning and delivery steps of the radiotherapy treatment (*Section 3.3*). As several of the strategies described in this chapter require some way to observe or infer the tumor position continuously during radiotherapy, a review of direct and indirect tumor tracking methods is given in *Section 3.1*.

In this work an indirect tumor tracking method is developed and its implementation for real-time tracking of the thoracic motion is presented in *Chapter 4*. The infrared dual-sensor based tracking system is described in *Section 4.1* and an accuracy and reproducibility analysis if given in *Section 4.2*. Then the origin of crosstalk with a dual sensor infrared tracking system is explained in *Section 4.3* and methods to avoid crosstalk are given in *Section 4.4*.

The infrared tracking system was used for real-time acquisition of the external respiratory signal in the 4D CT scanning protocol presented in *Chapter 5*. The 4D CT data acquisition process is detailed in *Section 5.1*, the reconstruction of the scanned volume at eight respiratory phases is described in *Section 5.2* and an analysis of the 4D CT images obtained is given in *Section 5.3*.

Conclusions and future work directions are given in *Chapter 6*.

CHAPTER 2
EFFECTS OF RESPIRATORY MOTION IN RADIOTHERAPY

As explained in Chapter 1, both the position and the internal anatomy of a patient can change significantly with time, both between and during radiation treatments. Inter-fraction motion/deformation is usually minimized by choosing patient's optimal position and immobilization and by daily tumor localization, to verify that dose delivery is carried out as planned. The major contributor to the intra-fraction motion/deformation in the thorax and abdomen is the breathing motion and *if the breathing-induced anatomic changes are not explicitly accounted for in conformal or intensity modulated radiotherapy, errors can be introduced during the imaging, planning and delivery steps of radiotherapy.*

2.1 Effects on imaging

In lung cancer sites, where tumor mobility can be significant, *the presence of tumor motion introduces image distortions and biasing of positional and volumetric information*, therefore greatly exacerbating the problem of target volume delineation and beam targeting [109, 110, 124].

Gagné *et al.* [34] used computer simulations to investigate the fundamental nature of CT image artifacts associated with lung tumors motion and their implications in target delineation. A brief description of their investigations and results is given in the following four subsections. The reconstruction process for a *stationary*

sphere is described in Subsection 2.1.1 and represents the reference point for the subsequent study on motion-induced artifacts. As a natural division exists in computed tomography between in-plane and orthogonal motions, motion-induced artifacts are studied for *in-plane* (Subsection 2.1.2), *orthogonal* (Subsection 2.1.3) and *in-plane combined with orthogonal* (Subsection 2.1.4) *object motions.*

2.1.1 Stationary case

Numerous projections (Fig. 2–1.a) are obtained during image acquisition and may be represented graphically in sinogram format (Fig. 2–1.b).

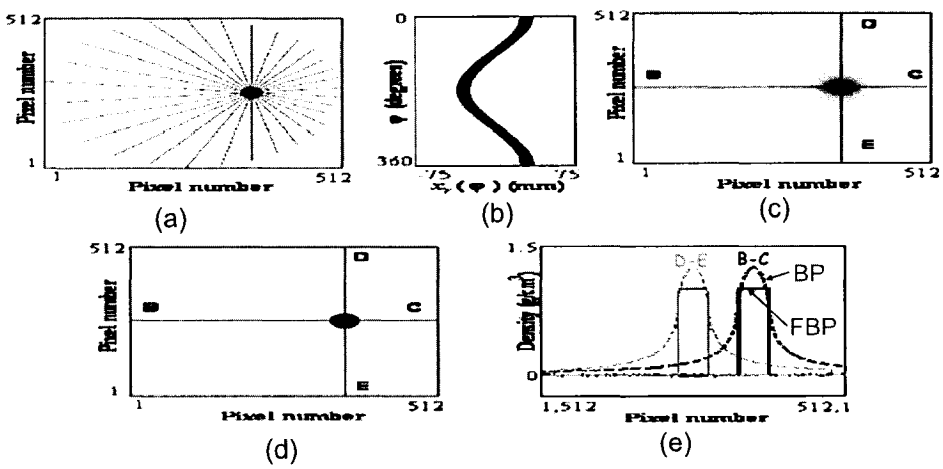

Figure 2–1: Image reconstruction illustrated for a stationary sphere: (a) projections through a specific point, (b) sinogram, (c) backprojected (BP) image, (d) filtered backprojected (FBP) image, (e) intensity profiles along lines B-C (dashed black line - BP, solid black line - FBP) and E-D (dashed gray line - BP, solid gray line - FBP). Reproduced from [34].

Simple reconstruction from backprojections (BP) results in a $1/r$ blurred image of the object (Fig. 2–1.c). Filtered backprojection (FBP) results in an image that better preserves the object's attenuation and geometric properties: the cross section

of the imaged sphere exhibits a uniform unit density while the surrounding area displays a uniform zero density (Fig. 2–1.d). Density profiles through the center of the reconstructed sphere, with and without filtering, are shown in Fig. 2–1.e.

2.1.2 In-plane motion

If the sphere moves along the horizontal axis of the imaging plane during data acquisition, the object projects to different detector positions and therefore each projection in the sinogram space keeps its original profile but is shifted in position, compared to the static case (Fig. 2–2.a).

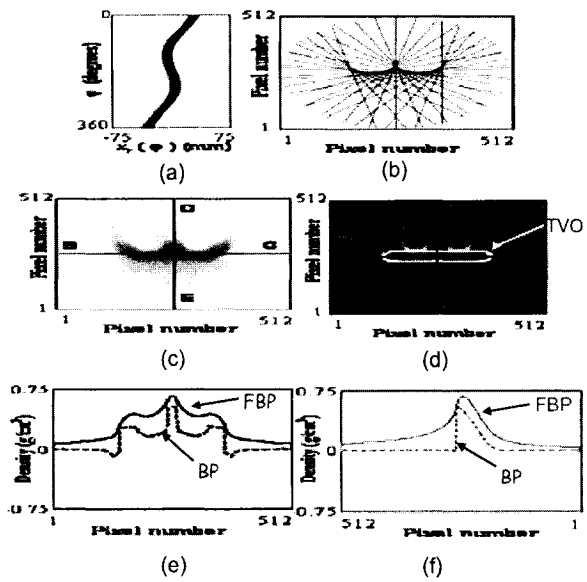

Figure 2–2: Motion artifacts in the CT of a sphere moving within the imaging plane: (a) sinogram, (b) projections through a specific point blurred due to motion, (c) backprojected (BP) image, (d) filtered backprojected (FBP) image with TVO contour (white line), (e) intensity profiles along line B-C (dashed black line - BP, solid black line - FBP), (f) intensity profiles along line E-D (dashed gray line - BP, solid gray line - FBP). Reproduced from [34].

The shape of the resultant curve is dependent upon both the trajectory and the extent of the motion captured during the acquisition. The positional shifts introduced in the sinogram lead to multiple intersection points during backprojection (Fig. 2–2.b) and their spatial distribution dictates the shape of the motion artifact. The $1/r$ blurred image density associated with a static object is now redistributed over a larger area of the image, in a pattern which no longer preserves radial symmetry (Fig. 2–2.c). The impact of filtering the motion-encoded projection data upon the reconstructed image is illustrated in Fig. 2–2.d. The reconstruction pattern deviates strongly from the corresponding total volume occupied (TVO), which describes the cross-sectional area presented by the mobile object during the imaging process. Significant density variations, characterize the cross-sectional area encompassed by the TVO contour (Figs. 2–2.e and 2–2.f).

2.1.3 Orthogonal motion

If the sphere moves perpendicularly to the imaging plane during data acquisition, the object's cross section present in the imaging plane varies during image acquisition and, hence, both width and intensity of the sinogram projections change accordingly (Fig. 2–3.a). Here the projections within sinogram space follow a similar curve to that associated with a stationary object but, in this case, the variations in the width and intensity of the projections are responsible for the motion artifacts observed in the BP and FBP images (Figs. 2–3.b and 2–3.c). In clinical situations, however, where tumor geometry is more complex, orthogonal motion will generally result in variations in both width and intensity of projections as well as in positional shifts leading to more complex motion artifacts. As with in-plane motion, profiles through

the mean position of the object in the imaging plane no longer retain the radial symmetry associated with the static object (Fig. 2–3.d). While the true total volume occupied (TVO) contour associated with this motion coincides with that of the static sphere, once again no single density value can be identified with this contour.

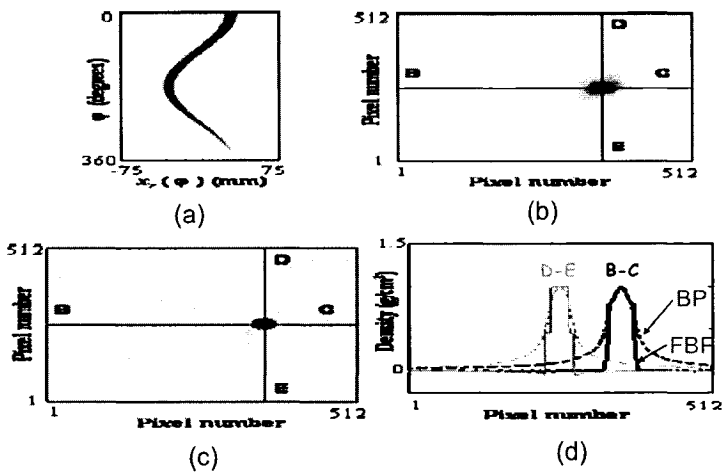

Figure 2–3: Motion artifacts in the CT of a sphere moving perpendicular to the imaging plane: (a) sinogram, (b) backprojected (BP) image, (c) filtered backprojected (FBP) image, (d) intensity profiles along lines B-C (dashed black line - BP, solid black line - FBP) and E-D (dashed gray line - BP, solid gray line - FBP). Reproduced from [34].

2.1.4 Combination of in-plane and orthogonal motion

Combining the preceding in-plane and orthogonal motions yields the sinogram of Fig. 2–4.a. The positional shifts observed in this sinogram arise due to the in-plane component of motion while the width and intensity variations result from the orthogonal component. Figures 2–4.b and 2–4.c show the resulting BP and FBP images, which now lack the symmetry observed when only the individual components of motion were present. As with the individual motion components, significant density

heterogeneity is observed throughout the image and the iso-density contours do not correspond to physically meaningful quantities (Fig. 2–4.d).

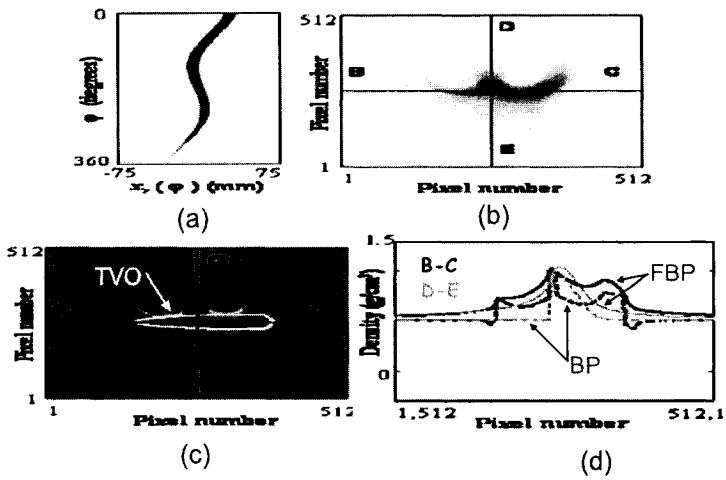

Figure 2–4: Motion artifacts in the CT of a sphere moving both within and perpendicular to the imaging plane: (a) sinogram, (b) backprojected (BP) image, (c) filtered backprojected (FBP) image, (d) intensity profiles along lines B-C (dashed black line - BP, solid black line - FBP) and E-D (dashed gray line - BP, solid gray line - FBP). Reproduced from [34].

To summarize, all current CT scans for lung radiotherapy are acquired while the tumor is non-stationary and are therefore subject to motion artifacts. From an imaging standpoint, *the mobile object is subject to a wide ranging degree of distortion from its true shape*, depending on object size, extent of motion and scan time. Barely detectable distortions are associated with rapid scans of objects whose range of motion is small in comparison to their physical size. In contrast, highly distorted images can result when the object size is small in comparison with the extent of motion. These effects are exacerbated by long scan times and can be so severe that

the reconstructed image is rendered unrecognizable. The presence of motion also impacts on the integrity of image density through partial volume effects combined with inappropriate filter application in the vicinity of the mobile object (in FBP image reconstructions). *Biased image density* renders contour delineation highly problematic because iso-intensity contours within these images cannot be guaranteed to correspond to physically meaningful cross sections. Equally, in a radiotherapy treatment planning which relies upon CT number fidelity for accurate heterogeneity correction, *false image densities within volumes surrounding the radiotherapy target* may translate directly into incorrect dose distributions.

2.2 Effects on planning

The common approach to treatment planning for mobile lung tumors uses a single CT scan acquired during quiet respiration. Margins of sufficient size to encompass all sources of planning and treatment uncertainties, including internal tumor motion, are used [104]. ICRU Reports 50 and 62 [46, 47] define the relevant terminology:

- The *gross tumor volume (GTV)* is defined as the volume containing the visible, demonstrated tumor. Labels can be used to distinguish between primary disease and other areas of macroscopic tumor involvement such as involved lymph nodes that are visible on imaging studies (*e.g.*, $\mathrm{GTV}_{primary}$ and GTV_{nodal}).
- The *clinical target volume (CTV)* is defined to enclose the GTV plus a margin to account for uncertainties in microscopic tumor spread. In specifying the CTV, the physician must not only consider micro-extensions of the disease near the GTV but also the natural avenues of spread for the particular disease and site, including lymph node, perivascular and perineural extensions.

- The *planning target volume (PTV)* is defined by specifying the margins that must be added around the CTV to compensate for the effect of organ, tumor and patient movements, inaccuracies in beam and patient setup and any other uncertainties. The PTV can be considered a 3D envelope in which the tumor and any microscopic extensions reside and move. Once the PTV is defined, appropriate beam sizes and arrangements can be selected. Multiple PTVs may be defined for a patient's radiation therapy treatment (*e.g.*, a higher dose to the PTV enclosing the GTV and a lower dose to the PTV containing the CTV).

The GTV and CTV are *anatomic-clinical concepts*, whereas the PTV is a *geometrical concept*, used for treatment planning and specification of the dose.

ICRU Report 62 [47], refined the definition of the PTV by introducing the concepts of *internal margin (IM)*, to take into account variations in size, shape and position of the CTV in reference to the patient's coordinate system and *setup margin (SM)*, to take into account all uncertainties in patient-beam positioning in reference to the treatment machine's coordinate system. The identification of these two types of margins is needed because they compensate for different types of uncertainties and refer to different coordinate systems. IM uncertainties are caused by physiologic variations and are difficult or almost impossible to control. SM uncertainties are related largely to technical factors that can be dealt with by more accurate setup and immobilization of the patient and improved mechanical stability of the machine.

How these margins should be combined is not straightforward and the selection of a composite margin and the delineation of the border of the PTV involve a compromise that relies upon the experience and the judgment of the radiation-oncology

team. ICRU Report 62 recognizes that the linear addition of the margins for all types of uncertainties would generally lead to an excessively large PTV. This could result in exceeding the patient tolerance and fail to reflect the actual clinical consequences.

The balance between disease control and risk of complications often dictates acceptance of reduced probability of cure in order to avoid severe treatment-related complications (see Fig. 2–5).

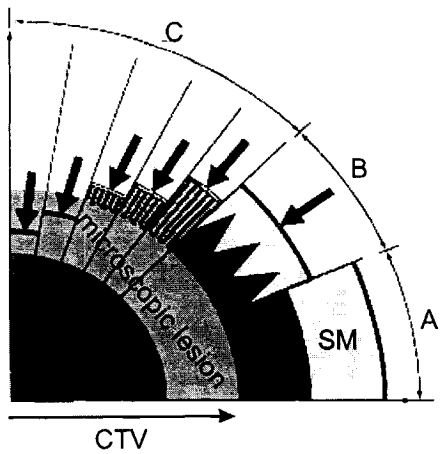

Figure 2–5: Various scenarios (A, B, C) for margin definition in treatment planning. Reproduced from [47].

Scenario A. The *linear addition* of the CTV, IM and SM define the PTV. The standard deviation (SD) of the Probability Density Function (PDF) corresponding to the total geometric uncertainty σ_{Total} is given by : $\sigma_{Total} = \sigma_{IM} + \sigma_{SM}$, where σ_{IM} and σ_{SM} represent the SDs of the PDFs for the setup error and the internal motion, respectively. As the setup error and the internal motion are generally not connected, this approach is, in general, not correct.

Scenario B. The linear addition of all factors of geometric uncertainty, as indicated in scenario A, often leads to an excessively large PTV, which would be incompatible with the tolerance of the surrounding normal tissues. In such instances, instead of adding linearly IM and SM, a compromise has to be sought and a smaller PTV has to be accepted. The SD of the PDF corresponding to the total geometric uncertainty is given by a *quadrature combination* of the SDs of the PDFs for the setup error and the internal motion: $\sigma^2_{Total} = \sigma^2_{IM} + \sigma^2_{SM}$. This approach assumes that the setup error and the internal motion are independent, which is reasonable as the internal motion is independent on where the patient is positioned with respect to the treatment beam (*i.e.*, setup error).

Scenario C. In the majority of the clinical situations, a *"global" safety margin* is adopted. In some cases, the presence of organs at risk dramatically reduces the extent of the acceptable safety margin (*e.g.*, presence of the spinal cord, optical nerve, etc.). In other situations, larger safety margins may be accepted. Since the incidence of subclinical invasion may decrease with distance from the GTV, a reduction of the margin for subclinical invasion may still be compatible with chance for cure, albeit at a lower probability rate.

Scenarios A and B provide guidelines for margin addition that are based on the assumption that the setup errors and internal motion PDFs have a normal distribution. Gaussian blurring with a combined SD of setup errors, internal motion and respiratory motion was found to be a valid approximation for the effect of random errors in fractionated radiotherapy [145]. However, while the setup error PDF has been

clinically measured to have an approximately normal distribution [23, 134], there is evidence that the internal motion PDF does not have a normal distribution [72, 83].

To better clarify the sources of geometric uncertainties, the Netherlands Cancer Institute group [146] has suggested dividing them into two categories: *systematic errors*, that is errors occuring during treatment preparation (*e.g.*, organ motion and set-up errors during CT simulation, delineation) and *random errors*, that is errors occuring daily, during treatment execution (*e.g.*, organ motion and set-up errors leading to daily variations). Inter-fraction variations (*i.e.*, day-to-day variation in patient setup or equipment) and intra-fraction variations (*i.e.*, movement of the patient or GTV/CTV within a single fraction) are both included in this last category.

Systematic errors are much more important than random errors. Systematic errors lead to a shift of the dose that will strongly affect some of the patients, if the shift is such as the CTV moves outside the high-dose region. Random errors blur the dose distribution and hence lead to a small decrease of the dose at the edge of the high-dose region. The effect of random errors can be estimated during treatment planning by blurring (*i.e.*, convolving) the computed dose distribution with the known error distribution and ensuring that the blurred dose distribution conforms to the PTV. The effect of the systematic errors will be unknown for each individual patient (insofar it has not been measured and corrected) and it must be treated statistically [135, 146]. *Most published margin recipes ignore systematic errors or fail to differentiate between random and systematic errors.* Because systematic errors have a larger impact on the target dose than execution errors, the effect of excluding preparation errors in treatment plan evaluations is that very small margins can

appear to be adequate [31, 147]. The published margin recipes that do differentiate between random and systematic errors can often be written as a linear combination of the SDs of random and systematic errors [135, 146].

As a function of the considerations on which they are based, margin recipes can be grouped into two categories: *recipes based on physical considerations*, that quantify the effects of the geometrical uncertainties on the dose coverage of the CTV and ensure a certain coverage probability [78, 135, 145] and *recipes based on biological considerations*, that evaluate treatment plans in terms of tumor control probability in the presence of geometrical errors [145, 147]. When comparing the recipes belonging to these two categories, the general trend is the reduction of the required margin when going from the physical to the biological considerations. However, as biological effects of geometrical errors depend on the model parameters used, *it is currently safer to base margin estimations on physics considerations, leading to larger margins.*

Van Herk *et al.* [145] reported on the *effect of respiration on treatment planning* and the respiration-induced asymmetric deviation in the shape of the total dose distribution. While for respiration amplitudes of 1 cm or less (SD = 0.36 cm) the asymmetry was negligible, for respiratory motion in excess of 1 cm in amplitude isodose lines were shifted in a distinctly asymmetric fashion and asymmetric margins were required. However, irrespective of the shape of the probability distributions, various SDs for respiratory motion would still add in quadrature: by adding 2.5 SD of systematic errors and 0.7 SD of random errors, the total margin obtained is about the peak-to-peak respiratory amplitude. This margin ensures the coverage of the respiratory motion and confirms the validity of this margin recipe (derived for

normally distributed errors) even in the case of an explicit non-normal distribution caused by respiration.

2.3 Effects on delivery

There are two approaches to account for motion in radiotherapy planning [11, 76] and both require some knowledge of the magnitude of the motion and some method to reduce or correct this motion.

1. The most common method consists of generating a treatment plan using a static patient model (the planning CT) but applies sufficiently large margins in the definition of the PTV, such that the CTV lies with high probability within the high dose region, even when motion is present (see also Section 2.2). The dose calculation is done using the planning CT and when evaluating the treatment plan it is assumed that enclosing the PTV within the prescribed isodose surface ensures that at least the prescribed dose is absorbed in the CTV. However, although this approach ensures good target coverage, there is no way of evaluating the effects of uncertainties on the dose to nearby non-target organs. Also, problems may be encountered when nearby critical structures have to be spared, especially when the PTV overlaps with planning organ at risk volumes, which is often the case in IMRT [80].
2. An alternative approach is to incorporate the sources of uncertainty directly in the dose calculation during the treatment planning process, thereby giving more complete and accurate information on the dose delivered to both the target volume and the nearby normal tissues [7, 73]. The treatment parameters are

then manually adjusted or automatically optimized, until the motion-modified dose distribution covers the CTV and spares critical structures as aimed.

The first approach can be viewed as basically a *"smearing" of the CTV* leading to an enlarged PTV, whereas the second approach represents a *"smearing" of the dose distribution.*

In this section, the second approach will be discussed and various theoretical and experimental studies on the effects of organ motion on dose distributions in conformal radiotherapy will be reviewed. These effects are presented in the decreasing order of their influence on the dose distributions: effects of motion on static delivery (Subsection 2.3.1), effects of motion on dynamic delivery (Subsection 2.3.2) and dose deformation effects (Subsection 2.3.3).

2.3.1 Effects of motion on static dose delivery: blurring effects

This subsection details the effects of motion on conformal radiotherapy where there are no movements of the field-shaping aperture during dose delivery, *i.e.*, conventional conformal radiotherapy with multileaf collimators (MLC), physical wedges, tissue compensators and also IMRT delivered with physical compensators.

Irradiating a patient who moves or whose inner organs move during the treatment leads to a *blurred dose distribution.* This occurs for both inter- and intra-fractional movements. With intra-fractional movements the dose delivered within each treatment will be blurred. With inter-fractional motion, the daily dose distribution will be sharp, but the total cumulative dose distribution after all fractions will be blurry.

The blurring leads to an enlarged beam penumbra at the field edge and thereby to a less conformal dose distribution (see Fig. 2–6). The amount of blurring depends on the amplitude and the characteristics of the motion and on the sharpness of the static dose distribution but it does not depend on the specific delivery technique.

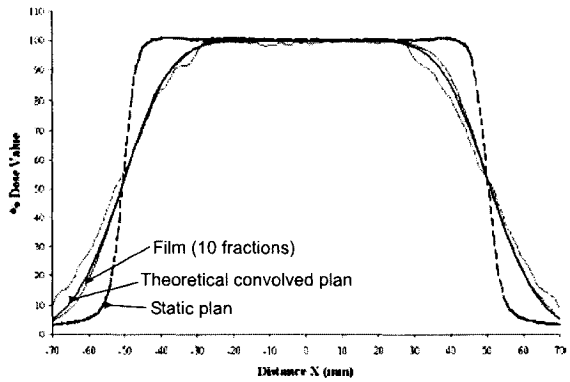

Figure 2–6: Motion during static dose delivery leads to a blurred dose distribution: solid water phantom, irradiated with 10 photon beams, shifted along a line parallel to the phantom surface according to a Gaussian distribution with a standard deviation $\sigma = 10$ mm. Reproduced from [82].

Mathematically, the blurring can be described by a *convolution* of the static dose distribution that would result without motion with a characteristic motion kernel [7]. The motion kernel itself can be interpreted as a probability density function (PDF), which describes the likelihood of different positions of tumor voxels or normal tissue voxels relative to their reference positions in the planning CT. The convolution approach is associated with two inherent assumptions that can potentially limit its usefulness:

1. In the convolution approach, the motion kernel is by definition *spatially invariant*, which implies that the shift of patient's position relative to the treatment

beams results in the delivered dose being shifted with the same magnitude in the opposite direction. The conditions for such an assumption are tissue homogeneity and flat patient surface, both hardly met in practice. If different organs move by different amounts, convolution is not strictly applicable. Rather, a superposition technique with spatially varying kernels [66] or a motion-encoded dose calculation through fluence modification [71] should be used.

2. The convolution approach assumes that the *dose distribution at a fixed point in space is not affected by surrounding organ motion.* However, this is only an approximation because motion of surrounding organs and tissue inhomogeneities distort the shape of the dose distribution to some degree [7, 31].

Despite these difficulties, the convolution approach can be easily implemented and provides a useful picture of the overall effect of motion on dose distributions.

2.3.2 Effects of motion on dynamic and step-and-shoot dose delivery: interplay effects

The dose variation at each voxel around an average blurred value can be strongly magnified through the *interplay effect*, which can occur during dynamic and step-and-shoot dose delivery, *i.e.*, when the radiation beam changes during the treatment process. This effect is caused by the interplay between intra-fraction organ motion and the motion of the radiation beam. An illustration of the interplay effect in the case of MLC delivery is shown in Figure 2–7.

Not only does the interplay effect lead to a variability of the dose delivered to each voxel, but it also leads to a spatial variation of the dose distribution in regions that would otherwise, without organ motion, receive uniform dose. When tumor motion is parallel to the leaf motion, the magnitude of the effect is determined by

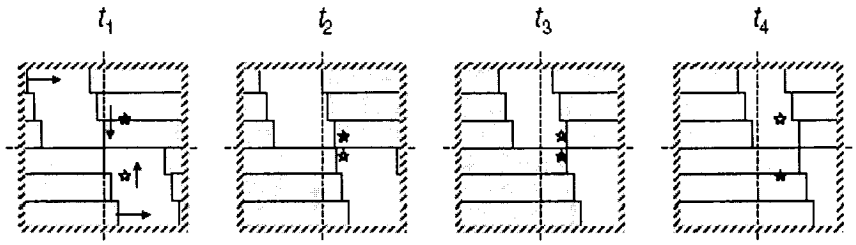

Figure 2–7: Illustration of the interplay between organ and leaf motion for the delivery of IMRT with an MLC. The leaves move from left to right. The star symbolizes a point in an organ that moves up and down and the 2 different types of stars represent 2 different phases of the motion. Depending on the phase relative to the leaf motion, the point can receive very different dose values. Reproduced from [12].

the interplay between the tumor and each leaf pair. When the tumor motion is perpendicular to the leaf motion, the effect is caused by the interplay between the tumor and the unaligned neighboring leaf end positions [49]. Bortfeld *et al.* [12] investigated the effect of intra-fraction organ motion on the dose delivered with MLC-based IMRT in a fractionated treatment. Organ movements were simulated using Matlab[1] by moving a two-dimensional calculation grid perpendicular to the beam direction in the isocentre plane. The effects of the organ motion are shown in Fig. 2–8, which displays differences between dose distributions with and without organ motion for an IMRT-MLC delivery in 30 fractions. The biggest deviations were always found at dose gradients that are oriented in the direction of the organ motion.

[1] Matlab software for technical computing, The MathWorks, Natick, MA, USA.

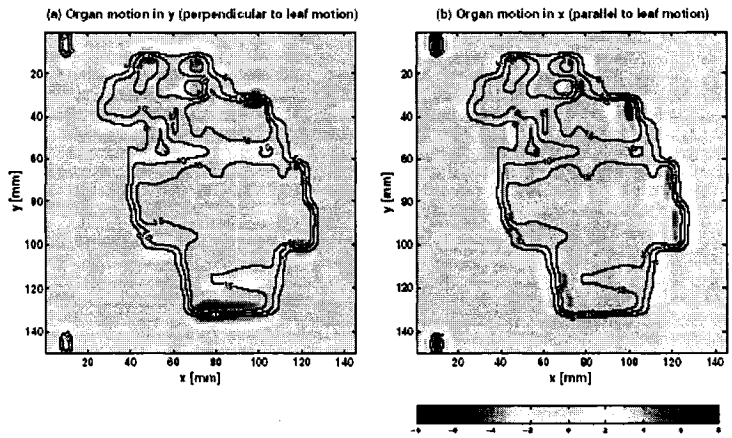

Figure 2–8: Difference between the dose with motion and without motion for MLC delivery with organ motion perpendicular to the leaf movement (a) and parallel to the leaf movement (b). The contour lines show the dose without motion. Dose differences are in Gy (see color bar). Reproduced from [12].

Bortfeld *et al.* [12] also investigated the issues of blurring and interplay effect from a theoretical point of view. Three questions were addressed by the authors:

1. The first question was about the *average dose distribution.* The statistical expectation value of the dose at a voxel is given by a convolution of the static case dose distribution with the motion PDF. Hence, the average dose distribution is a blurring of the static dose distribution and it is independent of the delivery technique: the average dose distributions for an IMRT delivery with MLC and with compensators will be the same, as long as the two techniques deliver the same dose distribution in the static case. Thus, blurring plays the same role in all treatment techniques in which organ motion is involved.
2. The second question was about the *variation of the dose around the average value for a realistic number of fractions.* It has been shown that, unlike the

average dose distribution, the variation around the average is characteristic of the interplay effect and is dependent on the treatment technique. The PDF associated with the dose deviation from the average dose in 1 fraction can have an arbitrary non-Gaussian shape, which depends on the treatment technique, the spatial PDF of the motion and the local dose gradient. However, independent of the individual dose PDF per fraction, the dose PDF after superimposing several fractions will always tend to be a Gaussian (normal) distribution (*central limit theorem*). In practice, it has been found that this is the case even after a moderate number of fractions (about 5). The relative width of the dose PDF, which is an indicator of the magnitude of the variation, is inversely proportional to the square root of the number of fractions. That means that, as more and more fractions are used, the relative variation of the dose at individual points from the blurred average becomes smaller (see also [159]). After a typical number of fractions in the order of 30 to 40, the dose PDF is very nearly Gaussian and its width is fairly small. The simulations performed by the authors showed that the SD of the dose variation after 30 fractions is 1 to 2% and less than 0.5% for IMRT delivery with MLCs and compensators, respectively.

3. The last question addressed by the authors is whether the *biologically effective dose* will be averaged out through fractionation. One consequence of the interplay effect is that the doses delivered in each fraction are no longer equal [157]. In an extreme case, the dose variation might be so large that a voxel receives the full dose in only one of the N_F fractions, and almost no dose in

the rest of the fractions. Because of the linear-quadratic biological effect, this leads to a bigger biological effect than when the same physical dose is delivered in N_F equal fractions. Using the linear-quadratic model and assuming α/β ratios between 0.5 and 10 Gy, the additional biological effect resulting from the non-even fractionation was shown to be negligible (0.5%) as long as the SD of the total physical dose from the expected value is less than about 3%. This condition seemed easily fulfilled in the majority of IMRT treatments with MLCs.

The interplay effect was studied in treatments using *enhanced dynamic wedges* by Pemler *et al.* [101]. The magnitude of the effect on the delivered dose distributions was studied for a variety of factors, including wedge angle, amplitude of organ motion, respiratory rate, asymmetry of the respiratory cycle, beam energy, and dose rate. The authors found that, for a breathing cycle with 3-cm amplitude and 6-s period, the maximum dose variation was 2.5, 7 and 16% for 10, 30 and 60° wedges, respectively.

Yang *et al.* [158] measured the interplay effect in *tomotherapy* delivered with both continuous helical and sequential segmented beams, using a computer-controlled dynamic phantom to simulate tomotherapy dose delivery and longitudinal tumor motion. It was found that, although motion reduced the dose uniformity perturbations for sequential tomotherapy, it can introduce small artifacts in dose uniformity for helical tomotherapy. With typical breathing frequency and amplitude, for a 2-cm beam width and a 4-rotations/min gantry rotation, the dose uniformity perturbation during helical tomotherapy was not significant.

All the above studies simulated tumor motion by simplistic sinusoidal models, while real patient respiratory cycles usually exhibit complicated patterns with continuously changing amplitude and periodicity, drifting baseline and hysteresis. However, all those characteristics can be incorporated into the mathematical models (PDFs) described before and therefore the qualitative findings remain unaffected. The main assumption made in the above studies is that the organ motion is random and not correlated with the beam delivery on different treatment days. The randomness is compromised, however, if few treatment fractions are used, such as in hypo-fractionation.

2.3.3 Dose deformation effects

The studies mentioned previously assume that the spatial dose distribution is invariant to displacements of the internal structures and of the whole patient. This assumption would be valid if the density of the organs were uniform. However, at interfaces between structures of different densities and/or atomic numbers, there are interface phenomena that affect the dose distribution locally. The location of these perturbation move with the moving interfaces and can lead to distortions of the dose distribution. Intuitively, dose deformation effects should be most pronounced for single field delivery and large displacements.

Engelsman *et al.* [31] studied dose deformation effects for lung tumors using a cork phantom with a spherically shaped polystyrene insertion to simulate the GTV. For a GTV displacement of 1.5 cm, the difference in dose due to the presence (or absence) of the tumor is up to 5%.

Beckham *et al.* [7] did a similar study in a unit density phantom with geometrical bone and lung inhomogenities and also found a maximum dose error of 5% for a random setup error with a SD of 1 cm.

Bortfeld *et al.* [11] performed 4D CT studies to investigate the dose deformation effect due to respiratory motion. Typically, ten CT data sets were obtained, each representing a different phase during the patient's breathing cycle. Based on this 4D CT data, it was possible to analyze the changes in deposited dose for real patient data. For a lung tumor patient, a 3D conformal 6-MV, 5-field treatment plan was designed based on a planning CT obtained under shallow breathing. This plan was then applied to the different 4D CT data sets, resulting in a dose distribution for each phase of the breathing cycle. An analysis of the 4D CT data showed that the peak to peak tumor motion was 1.35 cm. To analyze the spatial changes in dose deposition, calculated dose distributions were subtracted from each other for different breathing phases. Without the dose deformation effect, the differences should be zero. Figure 2–9 shows isolines for normalized differences between dose distributions calculated for inhale and exhale positions. The deposited dose changed within 3% because of the patients respiratory motion. Within the CTV, the changes in deposited dose were found to be within 1%.

All these studies above indicate that, for realistic displacements and multiple photon beam treatments, dose deformation effects should be rather moderate.

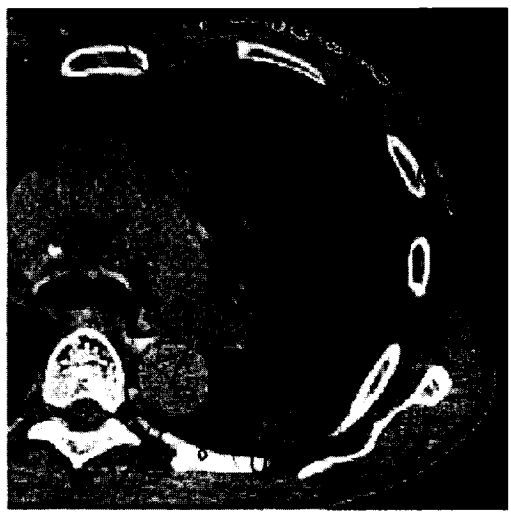

Figure 2–9: Differences between dose distributions calculated with the same treatment plan for breathing phases close to inhale and close to exhale. Plotted are the differences exhale-inhale, normalized to the doses calculated close to inhale: red 1%, green 2%, dark blue 3%, yellow 4%, light blue 5% and magenta 6%. Reproduced from [11].

CHAPTER 3
MANAGEMENT OF RESPIRATORY MOTION IN RADIOTHERAPY

Because intra-fraction organ motion can be substantial, with resultant alterations in organ volume definition and dosimetry, interventions to reduce it are required for many patients if dose escalation and reduction of dose to normal tissue are the treatment goals. Before radiation delivery, fluoroscopy, ciné CT and ciné MRI can be used to measure the magnitude of organ motion for each patient. Strategies to minimize non-respiratory organ motion include maintaining the same preparative regimen before each treatment and ensure comfortable immobilization and short overall treatment time. Interventional strategies for managing respiration in radiation treatments can be broadly separated into three major categories: *elimination/minimization schemes*, *correction schemes* and *incorporation schemes.*

The simplest approach to reduce dose margins and dose targeting error associated with breathing is to *minimize the breathing motion* itself, and the simplest way to do this is by educating the patient to breath in a shallow breathing pattern (*voluntary shallow breathing*). Jet ventilation, abdominal belts and stereotactic frames that produce firm abdominal pressure have also been used to reduce the respiratory motion of upper abdominal organs (*forced shallow breathing*). Another simple way to minimize the breathing motion is via breath holding and this can be done passively (*voluntary breath hold*) or actively (*forced breath hold*) and has been shown to reduce lung tumor position uncertainties to a few millimeters. If a patient breathing

cannot be regulated, the external beam exposure can be synchronized with the part of the breathing cycle where tumor motion is minimal (*respiratory gating*). All these elimination/minimization methods will be detailed in *Section 3.2.*

Correction schemes are used in CT imaging to reduce organ motion artifacts. A *sinogram analysis* (*i.e.*, an analysis of the tomographic projection data) identifies the net amplitude and phase of the organ motion and using this information a new sinogram with no motion effects is generated [25, 26, 69]. This approach could be applied to projection data used in transmission and emission CT, as well as in tomotherapy delivery modification and dose reconstruction. However, the application of the correction schemes requires either specialized software and/or hardware (*i.e.*, dual head CT) or invasive patient interventions (*i.e.*, gold seed implants).

Methods that *incorporate the breathing motion* into radiotherapy treatment planning can assume a number of forms. Acquiring CT images as fast as possible will minimize motion effects; alternatively *slow CT* techniques capture the full extent of movement by using long scan times which are of the order of the period of the breathing motion. *Real-time tumor tracking* is a more difficult approach, where the patient breathes freely while a tracking and control system monitors the tumor position and adapts the alignment of the radiation field continuously to follow the moving target. A third approach is *four-dimensional radiotherapy* (4D RT), where temporal changes in anatomy are taken into account during the imaging, planning and delivery steps of radiotherapy. A sequence of CT image sets is acquired for consecutive respiratory phases (4D CT), then treatment plans are optimized for each CT image set (4D treatment planning) and finally, this 4D treatment plan is

delivered continuously, in a breathing-synchronized fashion, throughout the entire breathing cycle (4D treatment delivery). Breathing motion-incorporation methods are described in *Section 3.3.*

Respiratory gating, real-time tumor tracking and 4D RT require some technique to observe or infer tumor's position continuously during treatment. The most direct method is to track the tumor fluoroscopically during treatment but, for real-time tracking of the tumor, the diagnostic x-ray exposure can be fairly high. Large fluoroscopic exposures can be avoided in principle by tracking an external breathing signal that is correlated with the tumor motion. *Direct and indirect tumor tracking methods* are the subject of the next section.

3.1 Tumor tracking methods

Ideally, information about the tumor position would come from direct tumor imaging and *kilovoltage fluoroscopy* has commonly been used to measure tumor motion at the time of the simulation. However, the use of fluoroscopy is inherently limited to structures that are sufficiently radio-opaque and multiple projections are required if organ motion is to be measured in more than one direction.

Tumors in soft tissue present a greater challenge to tracking during treatment. Occasionally, they can be discerned in radiographs but, in most instances, the tumor itself cannot be distinguished and surrogate landmarks must be used instead. If the tumor movement is closely connected to the *diaphragm*, whose edge can easily be seen in a radiograph, then the diaphragm can be used as a surrogate landmark; respiratory motion of the liver and pancreas can offer this possibility. For other soft tissue tumors, it may be necessary to implant artificial radio-opaque markers in or

near the tumor. Such markers have been used for prostate and bladder [125], lung [17], pancreas [88] and lower spine [84] cancers. Fiducial markers have the advantage that they are easy to locate with automatic image processing tools, enabling real-time fluoroscopic tracking. The disadvantage lies in the invasiveness of the procedure, which risks infection and the possibility of migrating fiducials. Also, rotation and deformation of the tumor cannot be measured with a single tumor marker; at least three markers are necessary to measure rotation and even then the deformation of the tumor cannot be detected.

The *skin dose resulting from imaging during fluoroscopic tracking*, even with high imaging efficiency and the lowest possible exposure, is up to 2 cGy per minute of treatment [127]. One commonly used criterion for judging imaging dose in a radiotherapy is to compare it with the leakage and scatter dose from the therapy beam: if it is less than the primary beam background (approximately 0.2% of the primary beam), then imaging dose can be considered to be another source of background[1] .

For a typical image-guided cranial or spinal radiosurgery treatment it is usually sufficient to detect and correct for residual motion at approximately 1-min intervals. The spine is much harder to discern than the cranium so it sets the upper bound on imaging dose. If fiducials are implanted into the spine, they can be detected with exposures of about 0.01 to 0.02 cGy. A typical radiosurgery fraction of 1500 to 3000 cGy (leakage dose of 3 to 6 cGy) will last 30 minutes and involve about 30

[1] However, the spectrum and geometry of the imaging dose is very different from the treatment beam background, making this a difficult criterion to interpret.

radiographic image pairs, for a total imaging dose of about 0.6 to 1.2 cGy. In this scenario, the imaging dose is less than the leakage dose [89].

For respiratory motion, the time scales for tumor motion and corrective response closely approximate continuous real-time tracking. Shirato *et al.* [127] have measured the imaging dose delivered during continuous fluoroscopy to track fiducial markers implanted in lung tumors. They use entrance doses of 2 cGy per fraction for a total imaging dose of 60 cGy for 30 fractions. For a total therapeutic dose of 6000 cGy, the leakage dose is 12 cGy and hence the imaging dose is 5 times the leakage dose. For a lung treatment delivered in 1 fraction the imaging dose would be 60 cGy all at once, which is not acceptable. This has led to investigation of ways to supplement imaging data with other signals of the tumor position. If the correlation is robust and reasonably stationary, the imaging frequency can be reduced from 30 frames per second to once every few seconds.

Another method of continuously tracking the organ position, which avoids large fluoroscopic exposures, has been developed by Seiler *et al.* [117]. Their technique allows the *tracking of miniaturized induction coils* with the use of magnetic fields. The induction coils can be fixed on a patient skin above the tumor, directly in the tumor or immediately adjacent such that they can move with the tumor. Alternating magnetic fields of about 12 kHz induce alternative voltages in the coils, which are measured by the data acquisition electronics. The position of the coils could be determined with a spatial accuracy of 1-2 mm and an angular accuracy of 0.5-1°.

Kubo and Hill [60] examined four respiration sensors to find the optimal sensor for monitoring the respiration cycle: a *thermistor*, a *thermocouple*, a *strain gauge* and

a *spirometer*. The thermistor and the thermocouple measure the *air flow temperature* during breathing, the strain gauge signals are related to the degree of *torso contour deformation with breathing* and the spirometer is designed to measure lung capacity by *measuring the volume of air passing through the airway during respiration.* An optimal sensor system should be characterized by reliability, accuracy, reproducibility, quick response, small drifts and large signal-to-noise ratio. Both the thermistor and the thermocouple were found to have similar response curves. The strain gauge, temperature sensors and spirometer adequately track the respiratory motion, but where patient comfort is concerned, the strain gauge and temperature sensor seemed advantageous over the spirometer. Another disadvantage of the spirometer is its baseline drift which linearly increase with time [61, 70].

Three breathing monitoring systems were used at the University of California Davis Cancer Center for breathing synchronized radiotherapy of thoracic and abdominal sites: a video camera based system, a RespiTrace system and a spirometer system [61]. The video camera monitors organ motion by *tracking two reflective markers* placed on a Styrofoam block attached to patient's torso. The RespiTrace system consists in a wraparound-inductive sensor, applied around the patient's trunk near the umbilicus, that *monitors trunk contour deformation with breathing.* The *airflow rate* through the patient mouthpiece was measured by a spirometer. The three respiration signals were well correlated, indicating that any one of these methods is satisfactory to monitor respiratory tumor motion.

Ozhasoglu *et al.* [98] investigated if the breathing motion of lung and pancreas tumors can be reliably inferred from external breathing indicators. The external motion data was collected from *optical tracking of infrared light emitting diodes taped on the patient torso* and from *measurements of tidal air volume* with a spirometer. *Fluoroscopic data* was collected by tracking fiducial markers implanted into the tumors. The external and fluoroscopic data showed a wide range of behavior in the normal breathing pattern and its effects on the tumor position. The relation between the external signals and the tumor position varies between patients and, more importantly, varies for an individual patient over a relatively short time period. The authors concluded that respiratory compensation strategies that infer tumor position from external breathing signals should be able to handle the complexities of real breathing patterns found in patients. A close spatial and temporal relationship between tumor's motion and external breathing signal should be verified.

Schweikard *et al.* [116] investigated methods to compensate for respiratory motion using robotic radiosurgery and combined *infrared tracking* and *synchronized x-ray* imaging to determine the position of the moving tumor. Six infrared emitters (three placed on the chest surface and three on the abdomen) were used to record the motion of patient's skin surface and a stereo x-ray imaging system provided information about the location of the implanted fiducial markers. During an initialization phase prior to treatment the correlation between the motions observed by the two sensors (x-ray imaging and infrared tracking) was computed and this model was continuously updated during treatment. The authors concluded that respiratory motion of internal organs can be correlated to visible external motion, provided that

the correlation model can be updated automatically in real-time by intra-operative images.

3.2 Elimination/minimization schemes

3.2.1 Shallow breathing

The simplest strategy used to reduce the effects of breathing motion is to reduce its amplitude, which can be achieved by educating the patient to breath in a shallow breathing pattern (*voluntary shallow breathing*), or by forcing this shallow breathing pattern through the use of *abdominal pressure* or *high-frequency jet ventilation.*

Voluntary shallow breathing. Patients who can maintain a calm respiration during simulation and treatment can be candidates for this treatment. Patients are instructed to perform shallow and fairly rapid respiration and are usually helped to maintain it during the positioning and treatment with an oxygen mask (3000-7000 cc/minute). Uematsu *et al.* used this approach for the stereotactic radiation therapy (SRT) of lung carcinomas: tumor motion was monitored and evaluated daily with the X-ray simulator, then direct CT positioning and immediate irradiation were performed [140, 141]. Shallow breathing, with or without an oxygen mask, led to a decrease in target motion of less than 5 mm in 42% of patients, 5 to 10 mm in 30% of patients and more than 10 mm in 28% of patients.

Advantages: easy to implement; reduces tumor motion to a range of 5-10 mm.

Disadvantage: difficult to achieve in patients with a compromised lung function.

Abdominal pressure. To reliably force the patient to avoid deep breaths, an abdominal pressure device, set up individually [140] or fixed reproducibly to a stereotactic body frame [40, 93], may be used.

The stereotactic body frame was originally developed at Karolinska Hospital, Sweden for hypo-fractionated extra-cranial stereotactic radiotherapy [64]. According to the Swedish concept, the stereotactic body frame is not only meant to be an immobilization device but is also a philosophy for treatment application: the stereotactic system of coordinates is used as reference system for the target position instead of anatomical landmarks such as bony structures or skin markers often used in conventional radiotherapy. Typical targets for extra-cranial stereotactic treatment are small tumors or recurrences of tumors of the lung, lung metastases, liver metastases, abdominal tumors, pelvic recurrences of rectal or cervical cancer and bone metastases. Unlike the situation in intra-cranial stereotactic radiotherapy, the use of hypo-fractionated stereotactic radiotherapy for extra-cranial targets has to consider motions of the target which is usually close to radiosensitive organs at risk (*e.g.*, mediastinal structures, stomach, duodenum, small or large bowel, rectum, urinary bladder, nerves or spinal cord).

The stereotactic body frame consists of 3 parts: a body shell, laser markers and a small abdominal pressing plate[2] . The body shell consists of a rigid frame and a vacuum pillow attached to the inside of the rigid frame. The laser markers are attached to the rigid body frame and project marks on the chest and legs of the patient; reference skin marks are drawn on these laser marks and are used for

[2] Elekta Instruments, Inc. commercially produces the body frame and the pressure plate system.

patient repositioning in the body frame. The small abdominal pressing plate presses the patient upper abdomen to reduce tumor movement during respiration.

Negoro *et al.* [93] evaluated the reduction in respiratory tumor movement using a stereotactic body frame in conformal therapy for solitary lung tumor. The abdominal press was successful in reducing the respiratory tumor movement from a range of 8 to 20 mm to a range of 2 to 11 mm. Herfarth *et al.* [40] evaluated respiratory movement of liver metastases treated with stereotactic single dose radiation. The use of abdominal pressure reduced the SI movement of the liver to a range of 3 to 13 mm.

Advantages: significant AP tumor motion reduction; tumor motion reduced to a range of 2 to 13 mm.

Disadvantages: fairly uncomfortable for the patients; residual SI tumor motion.

High-frequency jet ventilation. This is an artificial respiration technique performed under general anesthesia. The patient is intubated and the lungs are ventilated by an oscillating air flow, leading to a virtually complete loss of lung movement. High-frequency jet ventilation uses high respiratory rates (more than four times the normal rate), passive expiration and very small tidal volumes[3] (3-4 mL/kg) to achieve adequate oxygenation and ventilation.

Hof *et al.* [43] used high-frequency ventilation to reduce respiratory motion in stereotactic single-dose radiotherapy of lung cancer. An almost complete cessation of

[3] Volume of air which passes in and out of the lungs during breathing. Normal tidal volumes vary between 10 and 20 mL/kg.

the lung motion was reached, but the authors noticed that reliable tumor positioning could be a problem, because differences in lung inflation levels between the treatment planning CT scan and actual treatment could not be avoided.

Advantages: almost complete reduction of tumor motion.

Disadvantages: performed under general anesthesia; problematic inter-fraction tumor positioning; requires high logistic efforts.

3.2.2 Breath hold techniques

Another approach used to reduce the effect of breathing motion in radiotherapy is to perform treatment simulation and delivery while the patients hold their breath [51]. Breath holds can be *voluntarily* or *externally* regulated, provided the patients are able to comfortably maintain a stable breath hold of about 15 s.

Kim *et al.* [56] studied the reproducibility of lung cancer patients breath holds at four different points in the breathing cycle: normal and deep inspiration and normal and deep expiration. Although these positions represent the naturally occurring endpoints in the breathing cycle, deep inspiration and expiration tend to provide the best positional reliability. However, the *deep inspiration breath hold* (DIBH) technique is more advantageous for the treatment of thoracic tumors through its two distinct features: deep inspiration, which reduces lung density; and breath hold, which immobilizes the tumors targeted. Reduction of the tumor motion should permit either dose escalation or the same target coverage with a reduced field aperture. The reduced density of normal lung can reduce the amount of normal lung tissue in the high-dose region, thus reducing morbidity and improving the possibility of dose escalation.

Voluntarily breath hold. A *spirometer-monitored DIBH technique* was developed and clinically implemented for lung cancer conformal radiation treatments at the Memorial Sloan-Kettering Cancer Center (MSKCC) [37]. Patients breathed through a mouthpiece connected to a spirometer and nose breathing was prevented by the use of a nose-clip. Patients were coached through the following manoeuver: normal breathing, maximum inspiration, maximum expiration, maximum inspiration, breath hold. Simulation took approximately 2 hours and included the DIBH practice session and 3 helical CT scans (one normal breathing scan, and two spirometer-monitored scans, split into breath holds of 10 to 12 seconds each: one at DIBH and one at shallow inspiration). Patients performed the DIBH manoeuver for all treatment fields and portal images, all of which were delivered at maximum dose rate. An intra- and inter- breath-hold diaphragm position reproducibility of 1.0 $\pm$ 0.9 mm and 2.5 $\pm$ 1.6 mm, respectively, were reported. Lung density was reduced with 28% to 37% relative to normal breathing, thus reducing the fraction of normal lung tissue irradiated (see also [112]). However, approximately 60% of the lung cancer patients at MSKCC could not perform the DIBH maneuver reproducibly enough to permit its use.

Berson *et al.* [10] implemented a *self-held expiration breath-hold technique* using infrared tracking of markers placed on patient's abdomen. Automated voice instructions were used to facilitate synchronization of CT simulation and treatment with the exhale portion of the respiratory phase. During CT simulation, helical CT scans (split in 6 to 10 breath holds of 7 to 15 s each) were acquired. Orthogonal portal images were taken before treatment at least once per week and before each treatment

for patients treated with hypo-fractionation and/or complex treatment field arrangements. The entire prescribed set of MUs was typically delivered in one breath-hold, using a dose rate of 600 MU/min. Using this technique, the diaphragm deviation was reduced from 0.2 ± 0.7 cm during free-breathing to 0.0 ± 0.4 cm during breath-hold.

Kim *et al.* [56] reported a 16-patient feasibility study of a *self-initiated breath-hold technique*, in which patients were instructed to hold their breath without the use of external monitors or breath-holding devices. When the patient felt that the breath hold was sustainable, he or she would activate an interlock of the CT simulator or of a modified linac and then the therapist could either start the CT acquisition or turn on the radiation beam. A subsequent study by Barnes *et al.* [6] examined the tumor movement reduction and the dosimetric benefit of this technique in lung cancer treatments. Self-initiated breath-hold at DIBH was possible for 8 of the 10 patients that entered in the study. The average SI tumor movement determined from fluoroscopy was 12.9 mm during normal breathing (range of 2 to 31 mm) and 2.8 mm during DIBH (range of 1 to 3.8 mm). Two spiral CT scans (a normal breathing scan and a DIBH scans, usually split in 2 to 3 segments) were acquired for each patient and using this data, a normal breathing plan and a DIBH plan were generated for each patient. The mean percent lung volume receiving a dose higher than 20 Gy was reduced from 12.8% during normal breathing to 8% during DIBH. Onishi *et al.* [97] reported on a similar technique implemented on 20 lung cancer patients where the mean differences in tumor position with patients' self-breath-holding were 2.2, 1.4 and 1.3 mm in the SI, AP and RL directions, respectively.

Advantages: average SI tumor motion of less than 3 and 4 mm during deep inspiration and expiration breath hold, respectively; normal tissue protection at DIBH.

Disadvantages: limited by patient compliance and active participation; requires special staff effort and participation, as therapists must be trained to coach and advise the patients; longer simulation and treatment times; increased imaging dose (fluoroscopy or/and at least two planning CTs); spirometer-monitored technique is fairly uncomfortable for the patients; self-initiated breath-hold technique requires modified CT scanner and linac.

Active breathing control (ABC). The ABC method was developed at William Beaumont Hospital and is currently commercialized by Elekta, Inc. as the Active Breathing Coordinator. ABC consists in breath holds that are controlled, triggered and monitored by a caregiver. The ABC device consists of a mouthpiece connected to a spirometer and the air flow across the spirometer is integrated and displayed on a computer monitor. The operator uses a computer-controlled valve to close the flow of air to the patient at a predetermined point in the breathing cycle, effecting a controlled breath hold. The duration of the active breath-hold is that which is comfortably maintained by each individual patient and planning scans and radiation delivery are performed only during breath holds [51].

Wong *et al.* [154] studied the reproducibility of deep inspiration ABC for 12 patients with Hodgkins disease, lung or liver cancer. An average intra-fraction (30 min apart) and inter-fraction (1 week apart) diaphragm excursion of 1.5 $\pm$ 1.8 mm and 4 $\pm$ 3.3 mm, respectively, was reported for deep inspiration breath hold.

Dawson *et al.* [22] studied the reproducibility of normal exhalation ABC for 262 fractions of radiation in 8 liver cancer patients. From analysis of 158 sets of positioning radiographs, the average intra-fraction SI reproducibility of the diaphragm and hepatic fiducial markers position relative to the skeleton was 2.5 mm (range of 1.8 to 3.7 mm) and 2.3 mm (range of 1.2 to 3.7 mm), respectively. Based on 262 sets of positioning radiographs, the average inter-fraction SI reproducibility of the diaphragm and hepatic fiducial markers was 4.4 mm (range 3.0 to 6.1 mm) and 4.3 mm (range 3.1 to 5.7 mm), respectively. The authors concluded that radiotherapy using ABC for liver cancer patients is feasible, with good intra-fraction reproducibility of tumor's position using ABC. However, the inter-fraction reproducibility of organ position with ABC suggests the need for daily on-line imaging and repositioning, if treatment margins smaller than those required for free breathing are a goal.

The reduction in normal tissue irradiation was studied in radiotherapy using ABC-assisted DIBH for Hodgkins disease [132] and breast cancer [129] patients. For Hodgkin's disease, Stromberg *et al.* [132] reported a 12% average reduction in irradiated lung mass and a decrease of irradiated heart volume from 26% (free breathing) to 5% (ABC-assisted DIBH). Sixel *et al.* [129] reported decreases in heart volume receiving more than 25 Gy of more than 40 cc in tangential breast radiation therapy.

ABC-assisted breath holds at 75% maximum capacity has also been reported and used for treatments of breast cancers. Remouchamps *et al.* [107] used moderate deep-inspiration breath holds (mDIBH) with an ABC device in the treatment of patients with early-stage, left-sided breast cancer, using external beam radiation

therapy delivered to the whole breast. The authors showed that a 75% mDIBH achieved substantial internal organ displacement while maintaining patient comfort. A comparison of treatment plans performed on breath-hold and free-breathing CTs showed that ABC treatments achieved a mean absolute reduction of 3.6% in heart volume receiving 30 Gy and 1.5% in the heart normal tissue complication probability.

Advantages: intra-fraction diaphragm excursion of 1.8 to 3.7 mm; normal tissue protection at DIBH; standard operation of the CT scanner or linac.

Disadvantages: applicability limited by patient ability to hold breath comfortably for at least 20 s; poor inter-fraction organ reproducibility; longer simulation and treatment times; recommended imaging prior to each radiation treatment and therefore increased imaging dose.

3.2.3 Respiratory gating

Respiratory gating involves imaging and radiotherapy treatment delivery within a particular portion of the patients breathing cycle, commonly referred to as the *gate* [51]. The position and width of the gate within a respiratory cycle are determined by monitoring tumor's respiratory motion, either using *real-time tracking of implanted fiducial markers* or relying on *external respiration monitors* to infer the position of the tumor (see Section 3.1).

Gating systems that use real-time tracking of implanted fiducials. The most efficient respiratory gating is expected from gating on a direct image of tumor motion. However, because the tumor is often not visible in fluoroscopy or portal radiographs, tumor tracking requires implantation of radio-opaque markers into the tumor. In the absence of implanted markers, one must rely on a readily discernible

anatomic surrogate such as the diaphragm or the anterior chest wall. While the diaphragm correlates well with liver tumors [22], the correspondence of lung tumor motion with the diaphragm or the chest wall motion should be measured for each patient [98, 131].

Hokkaido University developed, in collaboration with Mitsubishi, a gating system *Real Time Tumor-Tracking Radiation Therapy* (RTRT), using real-time tracking of implanted fiducials [58, 119, 125, 126]. The RTRT system consists of four sets of diagnostic x-ray TV systems (two of which offer an unobstructed view of the patient at any time), an image processor unit, a gating control unit and an image display unit. The system recognizes the position of a 2-mm gold marker in the human body 30 times per second. The marker is inserted in or near the tumor and the linac is gated to irradiate the tumor only when the marker is within a given tolerance from its planned coordinates relative to the isocenter.

A set of three CT scans is acquired: a free-breathing CT scan and two breath-hold scans (one at inspiration, one at expiration). Of the three CT scans, the scan that yielded the best plan (based on tumor coverage, normal tissue sparing and treatment efficiency) is chosen as the planning CT scan. Because of the technical complexity, staffing requirements and the low duty cycle of this technology, lung and liver patients have been treated by hypo-fractionated stereotactic small-field irradiation [119]. Treatment times range typically from 30 to 45 min and the duty cycle varies greatly by patient. For each patient, the duty cycle is determined by the amplitude of the breathing motion and the extent of the volume representing

the permitted displacement. For lung cancer patients, Shirato *et al.* [127] reported a duty cycle ranging from 26 to 57%.

Shimizu *et al.* [126] analyzed 4 out of the 20 lung patients treated with the RTRT gating system between 1999 and 2000. The 4 patients were selected to represent 2 good and 2 poor cases of marker visualization for tracking. Marker movement during the beam-off period ranges from 5.5 to 10.0 mm, 6.8 to 15.9 mm and 8.1 to 14.6 mm in the RL, SI and AP directions, respectively. Marker movement during the beam-on period was reduced to less than 5.3 mm in all directions, for all patients.

Advantages: intra-fraction tumor movement is reduced to approximately 5 mm.

Disadvantages: based on invasive fiducial markers implanting; markers are not always inserted into the tumor so the measured tumor motion may not correspond to the real tumor motion; markers can migrate; tumor rotation and deformation cannot be detected with a single marker; requires a complex treatment hardware; increased treatment time; increased x-ray exposure.

Gating systems that rely on external respiration monitors. Various external respiration signals were described in Section 3.1 but, of all these techniques, optical tracking is currently the only commercially available system.

Clinical programs of respiratory gated radiotherapy were introduced in 1989 in Japan, where the Tsukuba Proton Medical Facility reported on a combination of an airbag and strain gauge to gate a proton beam [96]. In the United States, the University of California at Davis reported on the first feasibility study of gated radiotherapy in 1996 [60]. Subsequently, they described a gated radiotherapy system, developed jointly with Varian Medical Systems, which accepts respiratory signals from either a

video camera or a strain gauge [61]. The gating system that uses respiratory signals recorded by a video camera is now commercially available as *Varian's real-time position management respiratory gating system* (RPM) and it became the most widely used respiratory gating system.

The RPM system permits breathing-synchronized conventional or CT simulation, as well as gated treatment on a linear accelerator [51, 150, 153]. To monitor respiration, a lightweight block containing 2 passive reflective markers is placed on the patients chest or abdomen. Infrared light from an illuminator is reflected from the markers and detected by a charge-coupled-device video camera. The upper marker serves to track respiratory movement, whereas the lower marker serves to calibrate the system. A vendor-supplied program running on a desktop computer processes the video signals and sends on/off control signals to the simulator or the linear accelerator, synchronous with the patient's respiratory cycle.

During simulation and treatment, radiation is delivered only if breathing is regular and while the breathing waveform is inside the gate. If the breathing waveform becomes irregular, as a result of patient moving or coughing, the irradiation is immediately disabled and re-enabled only after breathing is again regular.

Patient training is important to allow familiarization with the breathing technique and to evaluate the patient ability to achieve a reproducible respiratory signal. Audio and visual coaching may improve patient's breathing regularity and hence improve the performance of the RPM system by decreasing the incidence of radiation hold-off from irregular breathing. Audio coaching can increase the regularity

of the breathing period, whereas video coaching aids in reproducing the breathing amplitude [61, 75, 150].

For planning of a gated treatment, it is essential to acquire a CT scan at the same part of the respiratory cycle as the treatment. Patients receive a single gated CT scan in the axial mode with the same parameters as those used for regular helical CT scans. The time required to acquire a gated CT scan depends on the respiration period of the patient, since there is one slice triggered per breathing cycle. Typical acquisition times are 3 to 4 times longer than conventional non-gated helical CT acquisition. Irregular breathing can further prolong the CT acquisition.

To minimize residual organ motion the gated treatment is usually centered at end-expiration [75]. Normal expiration during quiet breathing is a passive process during which the inspiratory muscles relax, resulting in a more reproducible anatomic position at end-expiration than at end-inspiration. However, gated treatment at end-inspiration can be more appropriate for lung carcinoma treatments because of the increased lung volume resulting in a lower dose to normal lung.

The choice of the gate's width is a tradeoff between minimizing motion within the gate and completing treatment in a realistic time. There is little respiratory motion within a narrower gate but this implies a long delivery time and overly long treatment times may give rise to setup errors because of motion of an uncomfortable patient. However, treatment times may be reduced by using higher dose rates. Mageras *et al.* reported gated treatments at 600 MU/min for both static and IMRT fields [75].

A key issue in gated treatment using external respiratory monitors is the accuracy with which the internal target position is predicted. Fluoroscopic studies with

the RPM system have shown high short-term (0.5 to 1 min) correlation between the respiratory signal (external chest displacement) and tumor motion in most cases [78, 150]. However in some cases and over longer observation times (1 to 10 min) the tumor position may have a poorer correlation with the external chest displacement [98]. Internal/ external correlation can be disturbed or lost completely by transient changes in breathing [98] or drifts of the external signal may occur, caused by patient movement [17].

Another key issue in gated treatments involves the reproducibility of the internal organ position between simulation and treatment. Although external monitors may correlate well with the respiratory motion of the target within a single session, the relationship between the external signal and the internal target position may change between sessions. It is therefore essential to have a program of frequent gated portal imaging of the target throughout the treatment to measure inter-fractional variations.

Wagman *et al.* [153] studied the clinical impact of the RPM respiratory gating system in the treatment of 8 liver cancer patients with end-expiration gating. Average SI diaphragm motion was reduced from 22.7 mm, without gating, to 5.1 mm, with gating. The reproducible decrease in organ motion with gating enabled reduction in GTV-to-PTV margin from 2 to 1 cm and allowed for dose increases of 7 to 27%.

Ford *et al.* [33] evaluated RPM effectiveness in the treatment of 4 lung and 4 liver cancer patients with respiratory gating applied at end-expiration (6 patients) and end-inspiration (2 patients). The patient-averaged mean displacement of the diaphragm from the planning position was 0.0 ± 3.9 mm.

Advantages: more generally applicable as potentially less demanding for the patient which breaths normally; intra-fraction diaphragm excursion of about 5 mm.

Disadvantages: some patient effort and concentration are required to follow the breathing coaching; requires modifications to the CT scanner or linac; commissioning of the gated radiotherapy system is required; longer simulation and treatment times; positional relation between tumor and surrogate may change over the treatment.

3.3 Incorporation schemes

Slow CT. In the slow scanning method, the CT scanner gantry rotation time is increased such that multiple respiration phases are recorded per slice. For lung cancer patients, conventional planning CT scans cover the entire thorax and are performed during quiet respiration with 3-mm slice thickness, 2.5-mm index and 1-sec/slice gantry rotation time. *Slow scans* typically cover the region around the tumor and are performed with 4-mm slice thickness, 3 mm-index and 4-sec/slice gantry rotation time. The image of the tumor obtained with slow scanning shows the full extent of the respiratory motion and consequently, slow CT scans produce larger target volumes than conventional CT scans. A further advantage of slow scanning over conventional scanning is that dose calculation is performed on a geometry which is better representative of that occurring during treatment.

Van Sornsen de Koste *et al.* [148, 149] evaluated the target coverage for the radiotherapy of 7 lung cancer patients using conventional and slow CT techniques. Their analysis showed that planning CT scans alone are insufficient for generating PTVs for peripheral lung tumors and can result in significant geographic miss.

Advantages: slow scanning is available on most CT scanners; PTVs derived using slow CT scans consistently produce superior target coverage than PTVs derived using conventional scans; dose calculation is performed on a more realistic geometry; treatment time is not increased.

Disadvantage: significant motion-induced image distortion.

Real-time tumor tracking. Arguably, the best way to accommodate intra-fraction tumor motion would be to realign continuously the beam so as to follow the tumor's changing position. Under ideal conditions, continuous real-time tracking should eliminate the need for a tumor motion margin in dose delivery, while maintaining a 100% beam duty cycle for efficient dose delivery. To be successful, a tracking system must be able to do four things: (1) *determine the tumor position*, (2) *anticipate the tumor motion* to allow for time delays in beam realignment, (3) *reposition the beam* and (4) *correct the dosimetry for motion effects.* All of this must be done automatically and in real time [51].

All approaches to real-time tracking require the *determination of the tumor position* on a time scale faster than the motion itself. In the case of breathing motion, because of the induced tumor velocity, nearly continuous position information is required. Ideally, the tumor motion would be observed continuously by *fluoroscopic imaging of the tumor itself*. This would provide the most direct and unambiguous measure of tumor position, but most soft tissue tumors will not present a well-defined, high-contrast contour suitable for automatic segmentation and image registration. Therefore, it is usually necessary to *track fiducial markers* that are

implanted in or near the tumor [17, 127]. During conventional 20-fraction radiotherapy treatments, the imaging dose resulting from continuous fluoroscopy, while high, can be considered tolerable compared to the therapeutic dose per fraction. However, during hypo-fractionated radiotherapy or single-fraction radiosurgery, even with high imaging efficiency and the lowest possible exposure, continuous fluoroscopic tracking would lead to an imaging dose beyond the generally accepted levels (see also Section 3.1). For this reason, researchers are developing *hybrid tumor-tracking techniques* that combine episodic radiographic imaging and continuous monitoring of external breathing signals, based on the premise that external motion surrogates can accurately predict the internal tumor position for the time interval between image acquisitions [17, 98, 116]. The external signal can be the chest or abdomen movement (measured with optical detectors [17, 61, 116] or strain gauges [60, 61]), the breath temperature (measured with temperature sensors [60]) or the tidal volume (measured with a spirometer [60, 98]). The feasibility of correlated tracking strategy depends on the strength and stability of the correlation between the 3D tumor motion and the respiratory surrogate signal. If the correlation is robust and stationary, it can be sufficient to evaluate it before the treatment (*e.g.*, by fluoroscopy) and then use it to predict tumor motion during treatment. However, this assumes that the correlation observed before treatment remains unchanged during the treatment and the physiology of breathing motion suggests that this is not necessarily a safe assumption [98]. If the correlation is not stationary, then it should be monitored and updated during treatment by acquiring images of the tumor position synchronously with the respiratory signal [116]. The *non-radiographic tracking* of an active or passive device

implanted in the tumor could provide an alternative to the use of radiological imaging to track the tumor position. Seiler *et al.* [117] described the electromagnetic tracking of miniature, implantable induction coils.

Real-time respiratory tracking requires that the beam realignment be synchronized with a fairly fast moving target [111]. Therefore, the tracking algorithm must be able to *predict the future position of the target* by an amount equal to the delay in beam realignment. Superficially, the respiratory cycle has a regularity that suggests that predicting it a few fractions of seconds in advance should be feasible. In reality, the problem is complicated by several factors: the breathing cycle is not strictly regular, but varies in amplitude and period from one cycle to the next; most of the target's motion occurs during a short segment of the breathing cycle; target position measurements have uncertainties and if target position is deduced from a surrogate breathing signal, the uncertainty in relating target and surrogate motion adds up to the uncertainty in predicting the tumor's position. There are two basic strategies to predict the breathing motion: develop a mathematical model that represents the respiratory cycle as a parameterized periodic function [94, 119] or use signal-processing algorithms (adaptive filters) that predict future motion based on a running sample of past motions [122, 151].

Real-time tracking requires the ability to *automatically adjust the position of the beam relative to the moving target*, allowing for all of the target's significant degrees of freedom. There are four possible ways to do this. For making intermittent adjustments to the patient's position in response to slow random or systematic movements, *automatic couch repositioning* may be used [9]. Charged-particle beams (*e.g.*, proton

beams) can be almost instantaneously redirected by *electromagnetic beam steering* [67]. *Shifting the aperture of a remotely-controlled collimator* (*e.g.*, MLC) was studied by Keall *et al.*, Neicu *et al.* and others [52, 94]. When shifting the MLC aperture of a conventional gantry-mounted linac, the beam alignment can be maintained only in the plane of the treatment field. *Automatic repositioning of a linear accelerator* has been clinically implemented with the CyberKnife radiosurgery system [1]. In this approach, a lightweight 6-MV X-band LINAC is mounted to an industrial robotic arm that can freely move and orient the x-ray beam with six degrees of freedom. A dual-camera x-ray imaging system monitors the target position and automatically sends position information to the robotic arm, which redirects the treatment beam as the target moves. The CyberKnife was used for frameless image-guided cranial [2], spine [90], pancreatic [88] and lung [17] radiosurgery.

The various approaches used to *correct the dosimetry* for breathing effects were discussed in Section 2.3. The planning CT scan, used to calculate the dosimetry, captures the anatomy in one static configuration, but patient's anatomy changes continuously with breathing. This perturbs the attenuation of the treatment beam and changes the relative positions of tumor, normal tissue and critical structures. Therefore, dosimetry needs to be corrected for the effects of all these changes.

In its primary clinical application, image-guided tracking allows neurosurgeons to perform cranial radiosurgery without the severe constraints imposed by a stereotactic frame. Head movement can be constrained by simple noninvasive restraints, and the residual target motion can be compensated by a tracking system that makes episodic measurements and corrections for the target position. This was the first

and remains the most common application of real-time tracking. Spine sites are very difficult to immobilize and thus are rarely treated with conventional frame-based radiosurgery. With the development of image-guided radiosurgery, it has become possible to treat sites along the spine without rigid immobilization. As with the cranium, these sites only move sporadically for a patient resting in simple conformable supports and thus can be tracked using simple episodic imaging and tracking.

The success of image-guided cranial and spine radiosurgery has stimulated the development of more sophisticated tracking procedures to deal with the more complex problem of respiratory tumor motion. For respiratory motion, the time scales for tumor motion and corrective response require continuous real-time tracking of the tumor motion. As radiography remains the main tool for directly monitoring the tumor position, continuous tracking would lead to a non-negligible accumulation of imaging dose during the treatment. If the tumor position is interpolated using some external respiratory signal, the correlation between this signal and the tumor movement must be robust and stationary. However, the relationship between lung tumor motion and external breathing signals is much more complex as periods, amplitudes, and phase differences change with time.

Advantages: clinical state of the art in image-guided cranial and spinal radiosurgery; under evaluation for image-guided radiosurgery in the chest and abdomen.

Disadvantages: increased imaging dose; the use of real-time tracking for torso image-guided radiosurgery relies on the assumption that the correlation between internal breathing-induced 3D tumor motion and respiratory surrogate signal is robust and stable.

Four-dimensional radiotherapy (4D RT). Four-dimensional radiotherapy (4D RT) is the explicit inclusion of the temporal changes in anatomy during the *imaging*, *planning* and *delivery* of radiotherapy [54].

Generally speaking, CT data sets with minimal motion artifacts can be acquired in three ways: (1) using techniques that shorten the scanner rotation times during image acquisition (*i.e.*, *fast scanning*); (2) using *prospective* gating to obtain a CT image set of a single breathing phase (*i.e.*, *respiratory gating*); (3) using *retrospective* gating to obtain CT image sets for multiple respiratory phases (*i.e.*, *4D CT*): as the patient is scanned, a respiration signal is simultaneously acquired and at the end of the scan the images are post-processed into individual 3D image sets according to the respiratory phase at the time each image was acquired.

After CT data acquisition, data registration into respiratory phases is based on either an internal anatomical match [99] or an external respiratory signal (RPM system [32, 53, 99, 152] or spirometer [68, 70]). The need for a respiratory monitor system can be removed by extracting the breathing signal directly from the projection data and performing the retrospective sorting in the projection space [130].

There are several approaches used for acquiring 4D CT data sets.

The use of a *single-slice CT scanner, operated in helical mode* [32, 152] usually results in gaps between images acquired at the same phase and these gaps become larger as the period of the respiratory cycle increases. The CT parameters are chosen to optimize the temporal resolution while minimizing the spatial gap between slices acquired at successive respiratory cycles: 0.5 pitch, 0.5-mm slice spacing and 1.5-s gantry rotation time. Major limitations of this approach are the scan extent

(restricted to the region of interest because of the x-ray tube heating) as well as the low spatial (4-6 mm) and temporal ($\approx$ 1 sec) resolutions for the reconstructed 3D scans. These limitations can be overcome by using a multi-slice CT scanner.

A *multi-slice CT scanner, operated in ciné mode*[4] has been used at Washington University [68, 70] and Massachusetts General Hospital [99, 108]. Currently, one 4D CT system is commercially available [99] that uses a ciné scanning protocol with retrospective gating to achieve 4D CT imaging in about 2 min with a 4-slice and 1 min with a 8- or 16-slice CT scanner. The clinical application of using the new 4D CT system has also been reported [142]. In this approach scans are acquired either *continuously* (for a time interval $\geq$ the average respiratory cycle plus the time needed for an image reconstruction) [99] or in an *image by image mode* (during 2 to 4 breaths) [68, 70], at each table position. The x-ray is turned off during CT table translation and acquisitions are repeated until the prescribed volume is completely scanned. The continuous mode shortens the scan duration (scanning 20 cm takes 1 min with an 8-slice CT or 2 min with a 4-slice CT) but the reconstruction quality relies more on the breathing consistency since data from only one breathing cycle is available at each couch position [99, 108]. In the image-by-image mode, it takes 3 to 5 min to cover the entire thorax but the over-sampling of several breaths at each slice position and the fine slice spacing allow high spatial (1.5 mm) and temporal (0.75 sec) resolutions for the reconstructed 3D CT scans [68, 70].

[4] A ciné scan is an axial scan with more than one gantry rotation per table position.

Keall *et al.* [53] developed and clinically implemented a method to acquire 4D CT scans using a *multi-slice CT scanner, operated in helical mode*. A 16-slice CT scanner was used (0.125 pitch and 0.5-s gantry rotation time) and 4D CT scans were reconstructed into 8 discrete breathing phases. The pitch is sufficiently low such that projection data for a full respiratory period is acquired per slice location. Current CT scanners usually do not readily support such low pitch values under normal operations and if the pitch is too high to collect data of a full respiratory period, missing slices within the 4D CT volumes will occur [53].

Pan [100] compared the acquisition time, slice sensitivity profile, dose efficiency[5] and ability to cope with an irregular breathing for ciné and helical acquisitions with multi-slice CT scanners. The major *advantages of the ciné 4D CT scan* are the slice thickness (equal to the slice collimation), 100% dose efficiency and better coping with irregular breathing cycles. The *advantage of the helical 4D CT scan* is about 10% speed-up in scanning but *major disadvantages* are the dose efficiency (96% for 4-slice scanners and 92% for 8- and 16-slice scanners) and the broad slice sensitivity profile.

A *respiratory correlated cone beam CT* yielding a 4D CT data set was clinically implemented at the Netherlands Cancer Institute [130]. The procedure consists of

[5] Dose efficiency is defined as the duration of the x ray used in the image reconstruction to the total x ray on time in the data acquisition. The dose efficiency for the ciné 4D-CT is 100%, *i.e.*, all the data collected can be used to generate images. The dose efficiency for the helical 4D-CT is $\frac{T_t - T_b}{T_t} \cdot 100\%$, where T_b is the breathing period and T_t is the total acquisition time of the scan.

retrospective sorting in projection space, yielding subsets of projections that each corresponds to a certain breathing phase. Subsequently, these subsets are reconstructed into a 4D cone beam CT data set. The breathing signal, required for respiratory correlation was directly extracted from the 2D projection data, removing the need for a respiratory monitor system.

A limitation of 4D CT is that this technique is strongly affected by variations in respiratory patterns during acquisition. Irregular respiration during CT data acquisition will compromise the quality of the resorted volumes. Training patients to breath in a regular fashion (by providing audio instruction or/and video feedback) can contribute to the regularity and reproducibility of the external respiratory signal and also increase the reproducibility of internal anatomy motion [57]. When using 4D CT data for target volume definition under respiratory motion, it should be emphasized that 4D CT volumes represent respiratory motion assembled over several breathing cycles on a specific day at a specific point in time. Changes in respiration are possible from day to day and even within minutes.

Once the 3D CT scans at multiple respiratory phases are obtained, the next problem is how to use this data for *4D treatment planning*. Because the amount of data is multiplied by the number of respiratory phases reconstructed, there is about an order of magnitude increase in the amount of work required to obtain a 4D treatment plan. Therefore, 4D planning requires automation and the tool that facilitates this automation is *deformable image registration* [18, 42]. This technique allows the volumetric mapping of a 3D CT image set from one respiratory phase to another respiratory phase. Once the transformations between the breathing phases are known,

processes such as anatomic contour definition, treatment planning and treatment evaluation on the multiple 3D CT image sets can be automated [29, 55]: *contours* are drawn on one reference 3D CT image set and then, using known transformations between breathing phases, contours are automatically drawn on the remaining respiratory phase CT image sets; similarly, a *treatment plan* is created on the reference 3D CT image set and then automatically created on the remaining respiratory phase 3D CT image sets, based on the beam arrangement and dose prescription in the reference plan; Monte Carlo *dose calculation* is simultaneously performed on each of the 3D image sets and the dose distribution obtained for each respiratory phase CT image set is mapped back to the reference CT image set for analysis. With this automation, the work-flow from a user interaction point of view is expected to be similar for 3D and 4D treatment planning.

The *delivery of the 4D treatment plans* require *real-time tumor tracking* and this approach to dose delivery was developed in the previous paragraph.

Advantages: *4D CT* - can be implemented on most CT scanners; motion artifacts are reduced and organ motion information is encoded in the 4D CT image set. *4D TP* - dose calculation includes temporal changes in anatomy. *4D dose delivery* - see previous paragraph on real-time tumor tracking.

Disadvantages: *4D CT* - increased CT simulation time; increased imaging dose; increased data volume; patient respiration reproducibility during the image acquisition is critical. *4D TP* - errors are introduced during deformable image registration. *4D dose delivery* - see previous paragraph on real-time tumor tracking.

CHAPTER 4
REAL-TIME TRACKING OF THE RESPIRATION-INDUCED THORACIC MOTION WITH AN INFRARED-BASED SYSTEM

Respiratory motion is known to be the largest intra-fractional organ motion and the most significant source of uncertainty in treatment planning of thorax and upper abdomen lesions. As radiotherapy tends towards increasingly conformal fields and delivery of higher doses over fewer fractions, the effects of respiratory motion have become more important. A review of the strategies used to reduce dose margins and dose targeting error associated with respiratory motion was given in Chapter 3 and several of these strategies require a means of observing or inferring the tumor position continuously during treatment.

Tumor motion may be observed directly by continuous fluoroscopic tracking of the tumor itself or of fiducial markers implanted in or near the tumor. However, in order to keep the imaging dose to acceptable levels, hybrid tumor-tracking techniques have been developed, which combine episodic radiographic imaging and continuous monitoring of external breathing signals. A review of the different methods used to acquire external breathing signals was given in Section 3.1. Infrared tracking systems track infrared light emitting diodes [86, 116] or reflective markers [28, 61, 150]. Whereas no tracking problems have been encountered with the use of infrared light emitting diodes, great care is needed in the positioning of the reflective markers in order to avoid "crosstalk" when a dual sensor tracking systems is used [28].

This chapter describes the implementation of a dual sensor-based Polaris tracking system [95] as a real-time tracking device for the thoracic motion. A description of the Polaris system (*Section 4.1*) is followed by an analysis of the accuracy and reproducibility of the measurements (*Section 4.2*). The origin of crosstalk with a dual sensor infrared tracking system is explained (*Section 4.3*) and methods to avoid crosstalk are discussed (*Section 4.4*). These results will be used in the real-time tracking of the breathing-induced torso motion for the 4D CT scanning protocol described in Chapter 5.

4.1 The NDI Polaris system

The Polaris system [95] is capable of tracking in real-time the motion of objects in three dimensions with three degrees of rotation. There exist two types of Polaris systems: passive Polaris systems, which track passive tools and hybrid Polaris systems, which track both active and passive tools.

Tools are solid objects to which at least three markers are attached and they are tracked by optically measuring the positions of these markers. Knowing the tool marker geometry, both the position and orientation of the tool can be determined. Active marker tools (Fig. 4–1.a) can have from 3 to 20 active markers (infrared emitting diodes, Fig. 4–1.b). Passive marker tools (Fig. 4–1.c) can have three to six passive markers (retro-reflective spheres or disks, Fig. 4–1.d) placed in a unique geometry, they are wireless, easier to construct and track fast motion more effectively than active marker tools.

The hybrid Polaris system used in this study consists of a position sensor and a tool interface unit which is connected to a host computer. The position sensor (Fig.

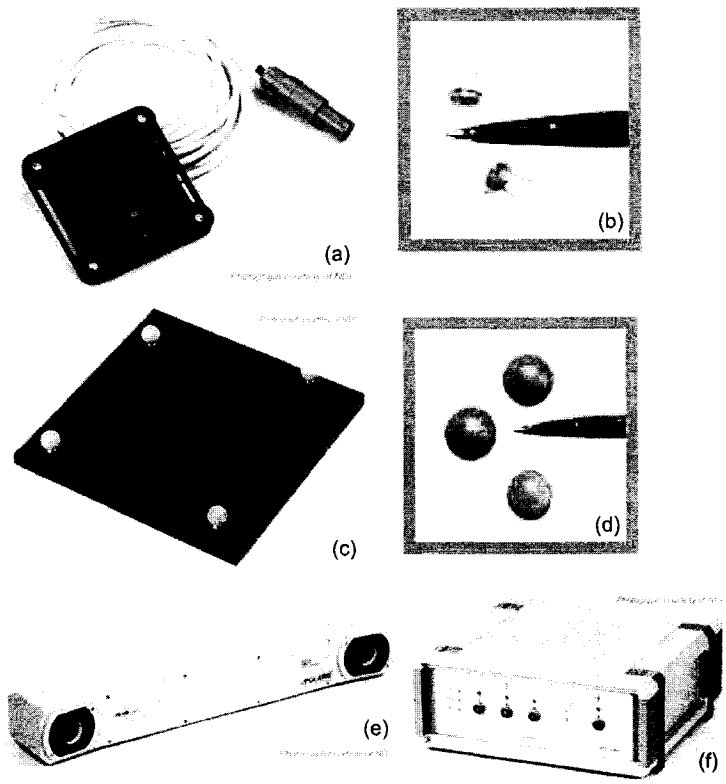

Figure 4–1: Hybrid Polaris system: active marker tool (a); active markers (b); passive marker tool (c); passive markers (d); position sensor (e); tool interface unit (f).

4–1.e) incorporates the illuminator rings which emit infrared light that is reflected back to the position sensor by the passive markers. The position sensor measures the intensity and position of infrared light that is either reflected from passive markers or emitted from active markers, calculates the translation and rotation of each tool and transmits the data to a computer for collection and display. The position sensor also interfaces between the host computer and the tool interface unit (Fig. 4–1.f) which supplies power to both position sensor and active markers and also controls the firing sequence of active markers when necessary.

The *field of view* is defined as the total volume in which the Polaris system can track a marker. Measurements must be made within a pyramid shaped measurement volume which extends from 1 to 2.5 m in front of the position sensor. This *pyramid measurement volume* is calibrated to an accuracy of 0.35 mm and a reproducibility of 0.2 mm.

The Polaris system is designed to be used for tracking tools, therefore the software provided by NDI is mainly tool oriented. In this work combined revision 018 firmware was used to report the 3D position for individual, passive markers and Matlab (The MathWorks Inc.) to generate the command sequence through a RS-232 serial interface, to collect the data and to display the results.

4.2 Accuracy and reproducibility of the Polaris system

Northern Digital Inc. (NDI) uses the 3D root mean square (RMS) error to characterize Polaris system's accuracy and reproducibility. The *accuracy* describes the degree of conformity of a measurement to an accepted standard value whereas the *reproducibility* describes the degree of agreement of repeated measurements. In this case both these quantities are described as averages over the measuring volume and termed "volumetric accuracy" and "volumetric reproducibility". According to NDI's technical specifications, the 3D volumetric accuracy acceptance criterion for the Polaris position sensors is ≤ 0.350 mm, based on a single marker stepped through more than 1200 locations throughout the measurement volume, using the mean of 30 samples, at 20°C. The 3D volumetric reproducibility acceptance criterion is ≤ 0.200 mm, based on a single marker stepped through more than 1200 locations throughout the measurement volume, using the mean of 30 samples, at 20°C.

In order to determine the accuracy of measurements made with the Polaris system, a single passive marker was placed on a mechanical workbench that allows translations in three dimensions with an accuracy of ± 0.01 mm and the displacements reported by the Polaris system were compared with the displacements measured on the workbench. The accuracy and reproducibility were determined in three different planes inside Polaris pyramid measurement volume (Fig. 4–2). In each plane, the reflective marker was translated along the X, Y and Z axes and the displacements (varying from 0.1 to 50 mm) were measured on the workbench. Then the accuracy and reproducibility of the displacements reported by the Polaris system were determined from 50 samples at each position.

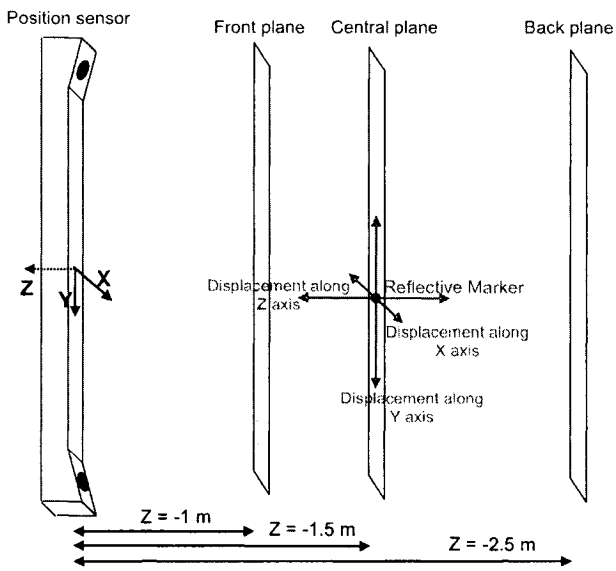

Figure 4–2: Setup used to determine the accuracy and reproducibility of the displacements reported by the Polaris system. Shown are three planes used in the measurements of accuracy and reproducibility of the Polaris system.

The accuracy and reproducibility in the pyramid measurement volume are shown in Figs. 4–3.a and 4–3.b, respectively. Both accuracy and reproducibility are reduced as the distance between marker and the position sensor increases. However, the deterioration in accuracy for increasing distances between 1 and 1.5 m is larger than the corresponding deterioration in reproducibility for the same distance variation. The distance dependence of the reported marker z coordinate is larger than that of the x- and y-coordinates. The measured reproducibility and accuracy values are better than quoted by NDI [95], but NDI stated the accuracy for absolute locations of a given marker. The goal in this analysis was to determine relative displacements of a given set of markers and not their absolute location, hence the accuracy for locations of the marker relative to an initial location was evaluated. In addition, NDI provides the accuracy and reproducibility acceptance criteria for 30 samples; in this analysis, 50 samples were used to ensure that the reproducibility will not affect the measurements of accuracy for small marker displacements.

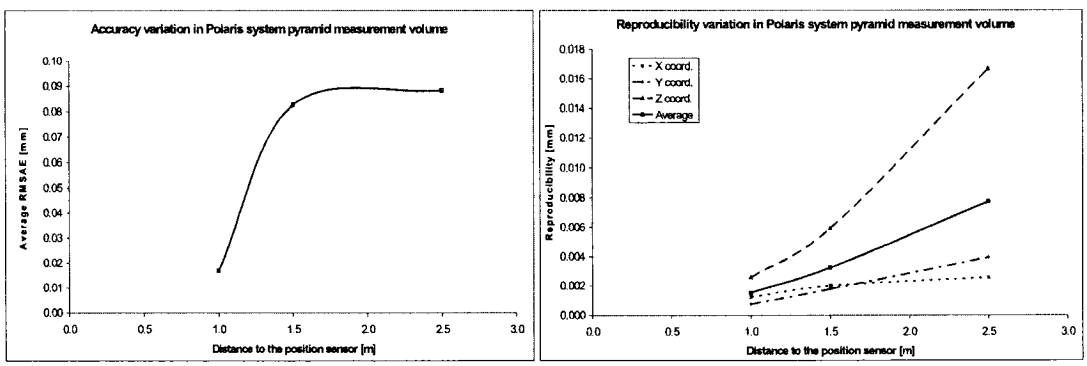

Figure 4–3: Accuracy (a) and reproducibility (b) variations in Polaris system pyramid measurement volume.

4.3 Use of the Polaris system in tracking multiple individual reflective markers

Ghost markers appear when two or more markers are coplanar with each other and with the two camera sensors of the Polaris system. This results in multiple mathematical solutions for each marker position. For example, in the case of two coplanar markers, there will be four mathematical solutions: two are the actual marker locations and the two others are ghost marker locations (Fig. 4–4). With no *a priori* knowledge about the position of the real markers, no distinction can be made as to whether a marker is real or virtual since swapping real and virtual markers produces exactly the same configuration. The number of ghost markers will increase with the number of coplanar markers which, for two sensor-based systems amounts to $n(n-1)$, where n represents the number of real markers.

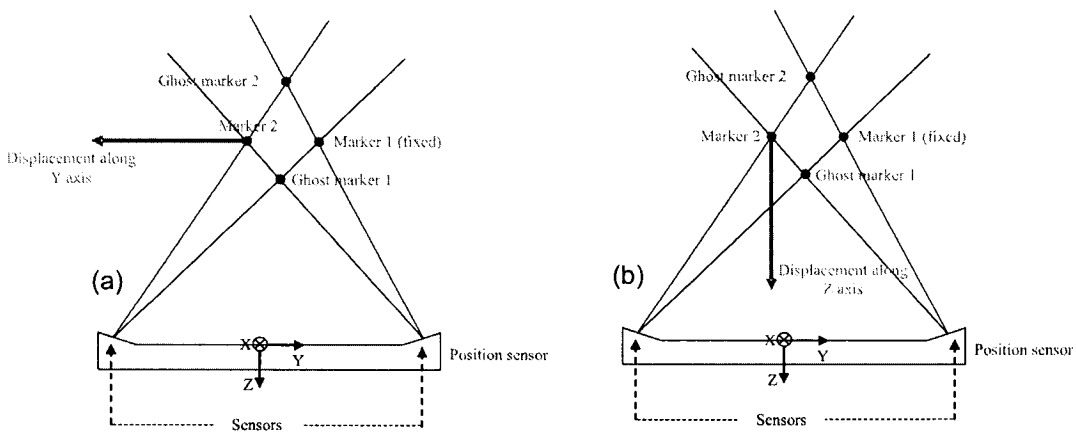

Figure 4–4: Marker configurations that lead to ghost markers. If the two passive sphere markers and the two sensors are coplanar, the position sensor will report four marker positions, two of which are ghost markers. Displacement of one of the passive sphere markers along position sensor Y axis (a) and Z axis (b) is shown.

When the Polaris system is used to track tools it can eliminate ghost markers by matching the marker position solutions to the known marker geometry. The six degrees of freedom transformation for the tool is determined and the unused ghost marker solutions are discarded. When the Polaris system is used to report the position of multiple passive sphere markers it reports all mathematical solutions for all the marker positions, hence the need to eliminate ghost markers with user software.

When the position sensor is used to track the position of independent passive sphere markers it will report these positions in a global frame of reference. This global frame of reference is established at the factory and its origin is centered on the front face of the position sensor. The exact location of the origin of the global frame of reference or the coordinates of the dual sensors in the global frame of reference are not known. If the sensor location in the frame of reference of the position sensor were known, for a given passive sphere marker, the existence and position of ghost markers could be predicted by evaluating whether the second passive sphere marker belongs to the plane determined by the two sensors and the first passive sphere marker.

In order to determine the location of the two sensors in the frame of reference of the position sensor, one can use the fact that the lines which join the sensors to the passive sphere markers intersect in four points (two real markers M_1 and M_2 and two ghost markers Gh_1 and Gh_2) and the position sensor gives the coordinates of these four points. Using this information the location of the right sensor can be determined as the intersection of the lines Gh_2M_1 and M_2Gh_1 and the location of the left sensor is given by the intersection of the lines Gh_2M_2 and M_1Gh_1 (Fig. 4–4).

Ideally, if all four objects (two reflective spheres and two sensors) were mathematical points, ghost markers should appear only if these four points are coplanar. However, the fact that ghost markers appear not for a unique marker-sensor configuration but for a set of configurations suggested that neither the markers nor sensors are points but have a finite "extent". Given that the position sensor reports the location of the center of the reflective sphere markers, the markers were considered as points and a geometrical extent was attributed to the sensors, which is hereafter referred to as *sensor extent.*

To determine this extent, a setup consisting of one fixed and one mobile passive sphere marker was used. The mobile marker was first moved to different locations along the position sensor Y axis (Fig. 4–4.a) followed by different locations along position sensor Z axis (Fig. 4–4.b). For each of these locations the mobile marker was also moved along the position sensor X axis. The range of positions along position sensor X axis for which ghost markers appeared were recorded. As a result of the finite sensor extent, the ghost markers appeared not always in pairs, but rather the total number of markers appeared in a 2-3-4-3-2 sequence rather than a 2-4-2 sequence. This sequence is represented in Fig. 4–5.a for three different locations of the mobile marker along position sensor Y axis and in Fig. 4–5.b for four different locations of the mobile marker along position sensor Z axis.

The range of mobile marker positions along position sensor X axis for which ghost markers appear is given in Tables 4–1 and 4–2, for several locations of the mobile marker along position sensor Y and Z axes, respectively.

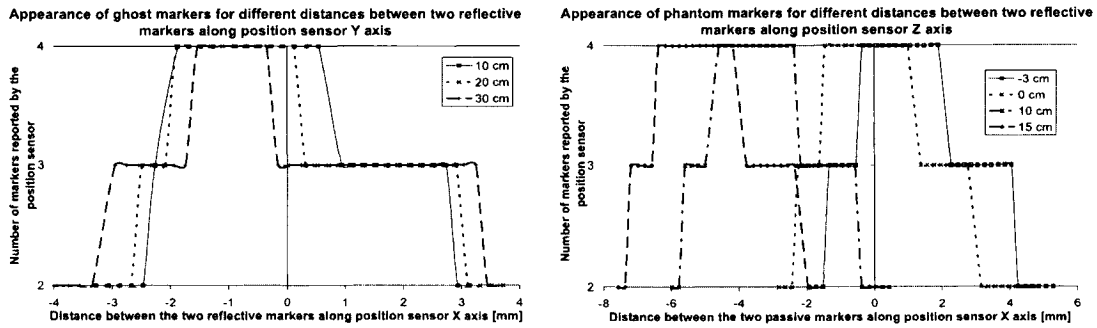

Figure 4–5: Sequence of markers reported by the position sensor when the mobile marker is moved along position sensor X axis: (a) different locations along position sensor Y axis and (b) different locations along position sensor Z axis.

Table 4–1: Ranges of ghost marker appearance for different locations of the mobile marker along position sensor Y axis.

Distance between the two passive sphere markers along position sensor Y axis (cm)	5	10	15	20	25	30
Mobile passive sphere marker X coordinate variation during the entire 3-4-3 marker sequence (mm)	4.83	5.00	5.00	5.40	5.80	6.20
Mobile passive sphere marker X coordinate variation during the 4 marker sequence (mm)	2.61	2.41	2.42	2.01	1.60	1.18

The location of the two sensors was calculated for each occurrence of the four-marker sequence as the intersection of the four lines joining the two real markers to the two ghost markers. Since the existence of four markers is required to uniquely calculate the location of the sensors, when three markers were observed, the sensor extent was extrapolated. Variation of sensor extents with constant step increments

Table 4–2: Ranges of ghost marker appearance for different locations of the mobile marker along position sensor Z axis.

Distance between the two passive sphere markers along position sensor Z axis (cm)	-4	-3	-2	0	2	4	7	10	15
Mobile passive sphere marker X coordinate variation during the entire 3-4-3 marker sequence (mm)	5.18	5.38	5.19	4.99	5.00	5.00	5.02	5.01	4.83
Mobile passive sphere marker X coordinate variation during the 4 marker sequence (mm)	2.43	2.23	2.24	2.43	2.42	2.23	2.22	2.20	2.20

of the distance between two reflective markers along the X axis was studied. For the four-marker sequence, the magnitude of the sensor extent along the X axis increased linearly as a function of distance between the two reflective markers whereas almost no variation was observed for the extent magnitude along the Y and Z axes. To determine a meaningful value of the sensor extent when the system reports a 3-marker sequence, linear extrapolation from the 4-marker sequence was used.

Figure 4–6 represents the resulting sensor extent in X, Y and Z directions as a function of distance between the markers. A similar variation of the right and left sensors with the distance between the two passive sphere markers along position sensor Y axis was observed: sensor extent in all directions decreases with distance but the extents along position sensor X axis show the strongest variation (from 2 cm to 5 mm). Compared to this variation, sensor Y and Z extents are almost negligible. A completely different behavior of sensor extent appears in Fig. 4–7 as function of the distance between the two passive sphere markers along position

sensor Z axis. As the mobile passive sphere marker approaches the position sensor, the X component of the left sensor range decreases while the X component of the right sensor range increases strongly. This behavior is due to the fact that the fixed passive sphere marker M_1 is gradually eclipsed by the mobile passive sphere marker M_2. A particular configuration is reached when M_2 overlaps Gh_1 and Gh_2 overlaps M_1 (Fig. 4–8). A similar situation occurs if the mobile passive sphere marker is moved away from the position sensor.

The sensors extents were determined to be 22 mm along position sensor X axis, 0.1 mm along position sensor Y axis, and 0.6 mm along position sensor Z axis.

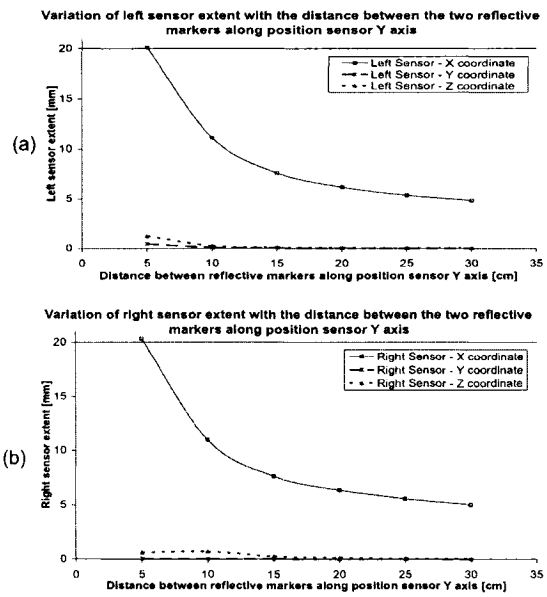

Figure 4–6: Sensor extent variation with the distance between the two passive sphere markers along position sensor Y axis: (a) left sensor, (b) right sensor.

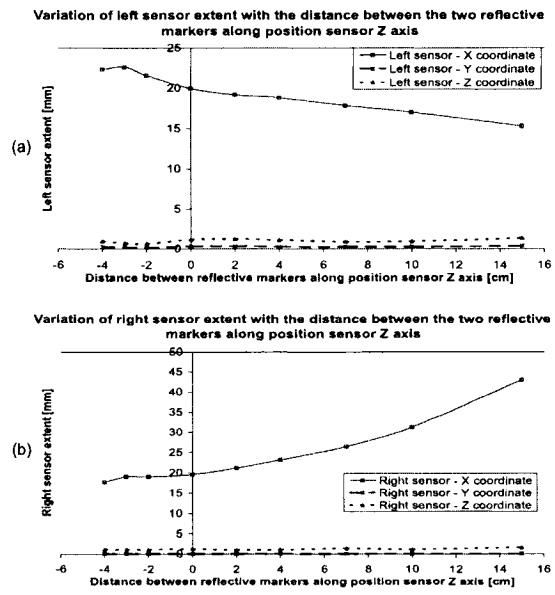

Figure 4–7: Sensor extent variation with the distance between the two passive sphere markers along position sensor Z axis: (a) left sensor, (b) right sensor.

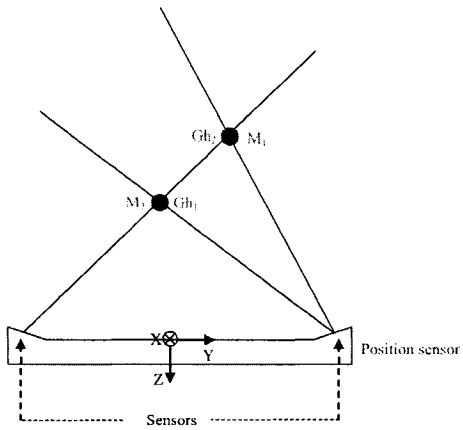

Figure 4–8: Extreme configuration reached when the mobile marker M_2 moves along position sensor Z axis.

4.4 Prediction of ghost marker appearance

The relative position of passive sphere markers along position sensor X axis is the main factor which determines the appearance of ghost markers. If two passive sphere markers and two points within the extents of both sensors lie within the same plane, one or two ghost markers will appear. Using the information acquired about sensors extents, it was found that what really determines the appearance of ghost markers is an infinite "ghost volume". As illustrated in Fig. 4–9, this volume consists of the two infinite lateral quadrants defined by the intersection of the two following planes: (1) the plane containing the fixed passive sphere marker, the point inside the left sensor range corresponding to the minimum X value and the point inside the right sensor range corresponding to the maximum X value; and (2) the plane containing the fixed passive sphere marker, the point inside the left sensor range

corresponding to the maximum X value and the point inside the right sensor range corresponding to the minimum X value.

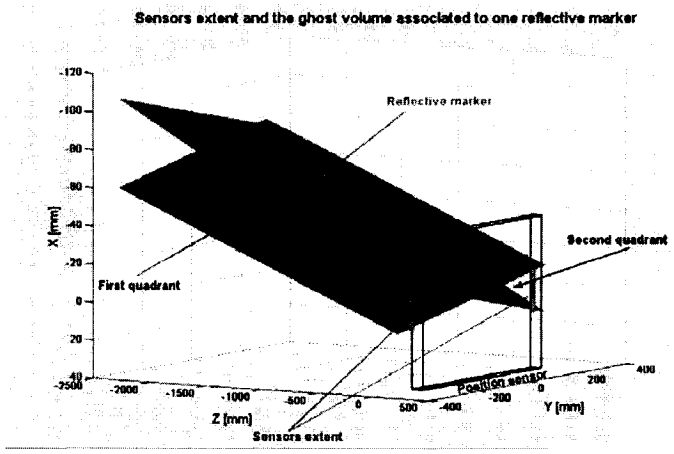

Figure 4–9: Sensor extents and corresponding ghost volume for a given passive sphere marker.

Ghost markers appear each time a passive sphere marker enters the ghost volume associated with another passive sphere marker.

Hence, once the maximum sensors extents is known, a ghost volume will be associated with each passive sphere marker and ghost markers are expected to appear as soon as a second passive sphere marker enters this volume. Moreover, *if passive sphere markers lie on a known surface, the ghost volume will be reduced to a "ghost zone"*, the intersection between this surface and the ghost volume associated to each passive sphere marker. *The ghost zone is an intrinsic property of a marker, and is only dependent on the location of this marker and the shape of the surface to which it belongs.* On the other hand, *the ghost volume is uniquely determined by the position of the marker and the extent of the sensors.*

Thus, *for multiple markers, the pattern required to avoid the appearance of ghost markers can be predicted.* This was done for two patterns built with passive sphere markers: three passive sphere markers taped on a planar surface and two passive sphere markers taped on a anthropomorphic thorax phantom. For these two patterns, the appearance of ghost markers once a passive sphere marker entered in the ghost zone of other passive sphere markers was verified. As the Polaris system was evaluated as a possible tool for real-time tracking of several markers during a CT acquisition, the variation of the shape of the ghost zones was studied as a function of the angle of view of the position sensor as well as the distance between the reflective markers and the position sensor.

4.4.1 Passive sphere markers on a plane

The appearance of ghost markers was studied for different configurations of three passive sphere markers on a plane and for two different angles of view α of the position sensor (Fig. 4–10).

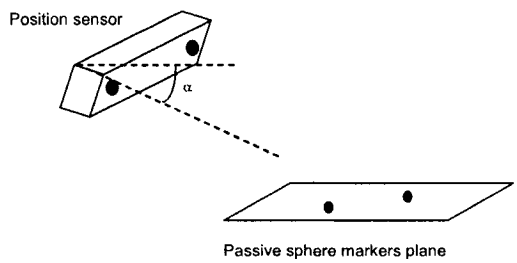

Figure 4–10: Angle of view of the position sensor.

For an angle $\alpha \approx 10°$, if the passive sphere markers were not inside the ghost zones corresponding to other passive sphere markers, no ghost marker was reported

by the position sensor. If one passive sphere marker entered the ghost zone of other passive sphere markers, ghost markers were reported by the position sensor. For an angle of view $\alpha \approx 20°$ ghost markers appeared again as soon as one of the passive sphere markers entered the ghost zone of other passive sphere marker. The only difference from the previous configuration was that the ghost zones were narrower for the smaller angle (Fig. 4–11). This is due to the fact that the intersection between the ghost volume of a marker and the plane to which the marker belongs is narrower for larger angles of view. Hence, *for the same passive sphere marker pattern, the probability of having ghost markers is smaller if the angle of view of the position sensor is larger.*

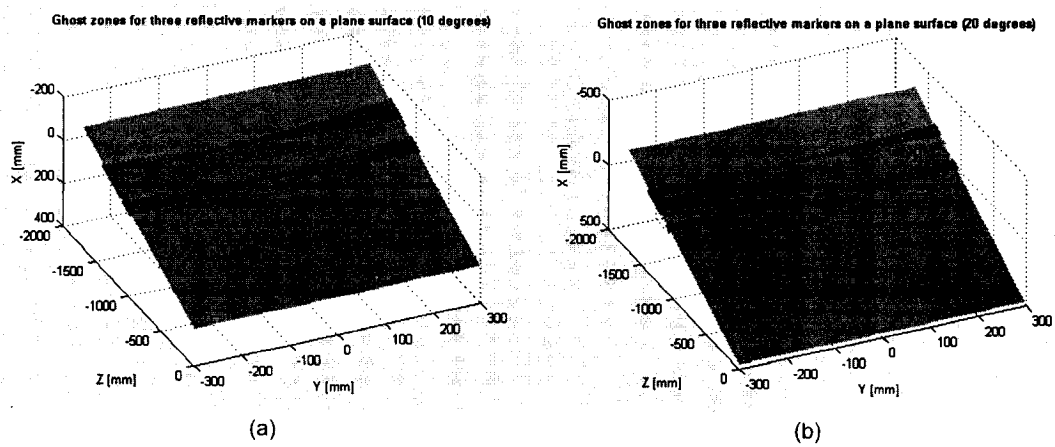

Figure 4–11: Ghost zones for three passive sphere markers lying on a plane: (a) angle of view $\alpha \approx 10°$; (b) angle of view $\alpha \approx 20°$. Larger angles of view lead to narrower ghost zones.

4.4.2 Passive sphere markers on an anthropomorphic thorax phantom

As explained previously, the ghost surfaces for a given set of passive sphere markers are defined by the intersections between the ghost volumes corresponding to those passive sphere markers and the surface on which these passive sphere markers lie. For the case described in Subsection 4.4.1, this surface was a plane and its mathematical equation was determined from the coordinates of the three passive sphere markers lying on it. For the two passive markers taped on the anthropomorphic phantom, the phantom was scanned and its contour was determined in order to acquire the coordinates of the surface points.

Initially, for each set of patterns, each passive sphere markers was located outside the ghost zones of other passive sphere markers. For these configurations no ghost marker were reported by the position sensor. Then, one of the passive sphere markers was placed inside the ghost zone of the other marker and therefore one or two ghost markers were reported by the position sensor. The variation of the shapes of the ghost zones corresponding to the two sets of patterns with position sensor's angle of view was studied. For the two passive sphere markers affixed on the anthropomorphic phantom, the evolution of the ghost zone shapes with the position sensor's relative location and distance to the phantom was also studied.

Figure 4–12 shows the variation of the ghost zone of one passive sphere marker with the angle of view when the position sensor is placed 1.95 m superior from the phantom. Consistent with previous observations, the ghost zone is wider when the angle of view is 15° than at 30°. Variations in distance between the position

sensor and phantom generate a translation of the ghost zones over the surface of the phantom.

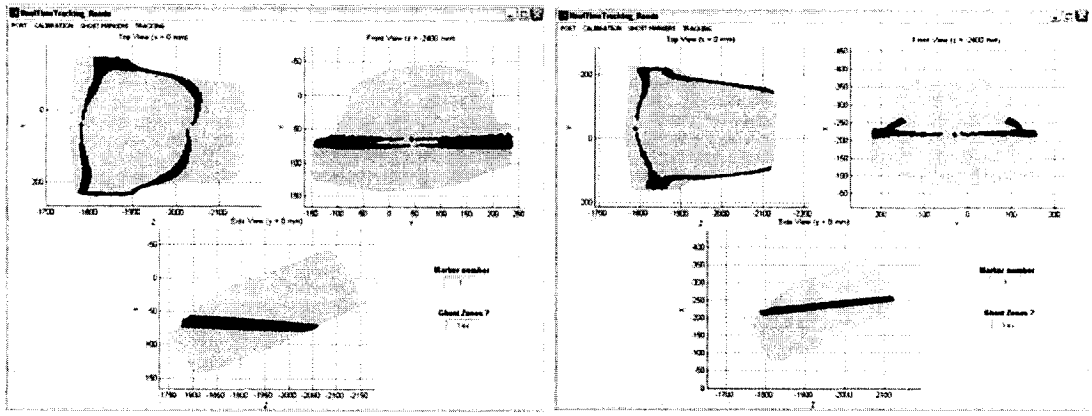

(a) (b)

Figure 4–12: Ghost zone (dark) of one reflective marker when the position sensor is placed superior, at 1.9 m from the anthropomorphic phantom: (a) angle of view of 15° and (b) angle of view of 30°. The light gray areas represent the contour surfaces of the anthropomorphic phantom.

The shape of the ghost zone of the same passive sphere marker changes completely when the position sensor is placed inferior to the phantom (Fig. 4–13). The different results obtained for the inferior location of the position sensor can be explained when considering the definition of the ghost zones. The intersection of the ghost volume with the surface to which the markers belong (the contour of the anthropomorphic phantom) is different when the position sensor views the phantom from the head and from the feet, respectively. This analysis is consistent with the empirical observations made by Dieterich *et al.* [28].

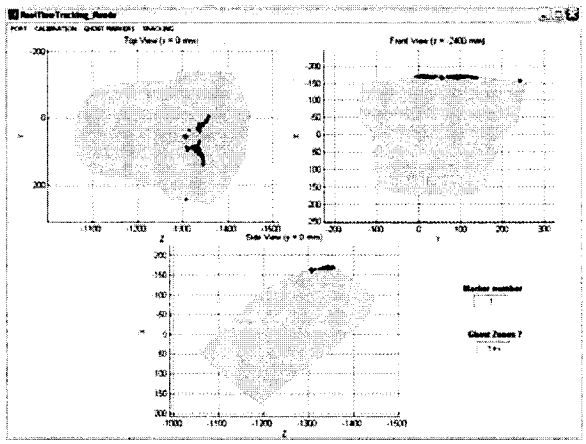

Figure 4–13: Ghost zone (dark) of one reflective marker when the position sensor is placed inferior, at 1.3 m from the anthropomorphic phantom (angle of view of 45°). The light gray areas represent the contour surfaces of the anthropomorphic phantom.

4.4.3 Ghost marker-free patterns

The ability of building ghost marker-free patterns was essential in the evaluation of the Polaris system as a possible tool for the external respiratory signal acquisition during the 4D CT scanning procedure. As several markers are tracked during the CT acquisition and as their position relative to the Polaris system changes continuously during scanning, ghost markers can appear. However, if a ghost marker-free pattern is available at the beginning of each scan, any ghost marker appearing later can be discarded (see also Subsection 5.1.3).

After studying the shape of the ghost zones for the passive sphere markers taped on the anthropomorphic phantom ghost marker-free patterns could be build for each given configuration. The limit of number of markers is reached when the entire surface of the anthropomorphic phantom is covered by ghost zones corresponding to the passive sphere markers that form the pattern. When the position sensor

was placed superior to the anthropomorphic phantom (*i.e.*, phantom is viewed from head downwards, see Fig. 4–14.a), 18 passive sphere markers could be used to build a ghost marker-free pattern (Fig. 4–14.c); the coverage of the phantom's surface by the ghost zones of the passive sphere markers is shown in Fig. 4–14.e.

When the position sensor was placed inferior to the phantom (*i.e.*, phantom is viewed from foot upwards, see Fig. 4–14.b), the same number of markers could be used to build a ghost marker-free pattern (Fig. 4–14.d) but the surface of the anthropomorphic phantom that was not covered by ghost zones was much more limited (Fig. 4–14.f). It can also be noticed that, because of the different orientations of the position sensor with respect to the anthropomorphic phantom, the orientation of the ghost zones is different from one configuration to the other.

After comparing the shape and extent of the ghost zones in Figures 4–14.e and 4–14.f, *the configuration with the position sensor superior to the phantom was chosen for subsequent use of the Polaris system in the 4D CT data acquisition protocol.*

4.5 Summary

This chapter described the implementation of the dual sensor-based Polaris tracking system as a real-time tracking device for the thoracic motion. The accuracy and reproducibility of the Polaris system were evaluated and considered satisfactory for real-time acquisition of the external respiratory signal during a 4D CT data acquisition protocol.

However, for the use of the Polaris system in the implementation of the 4D CT data acquisition procedure, several reflective markers needed to be affixed on the anthropomorphic phantom. The occurrence of "crosstalk" (*i.e.*, ghost markers)

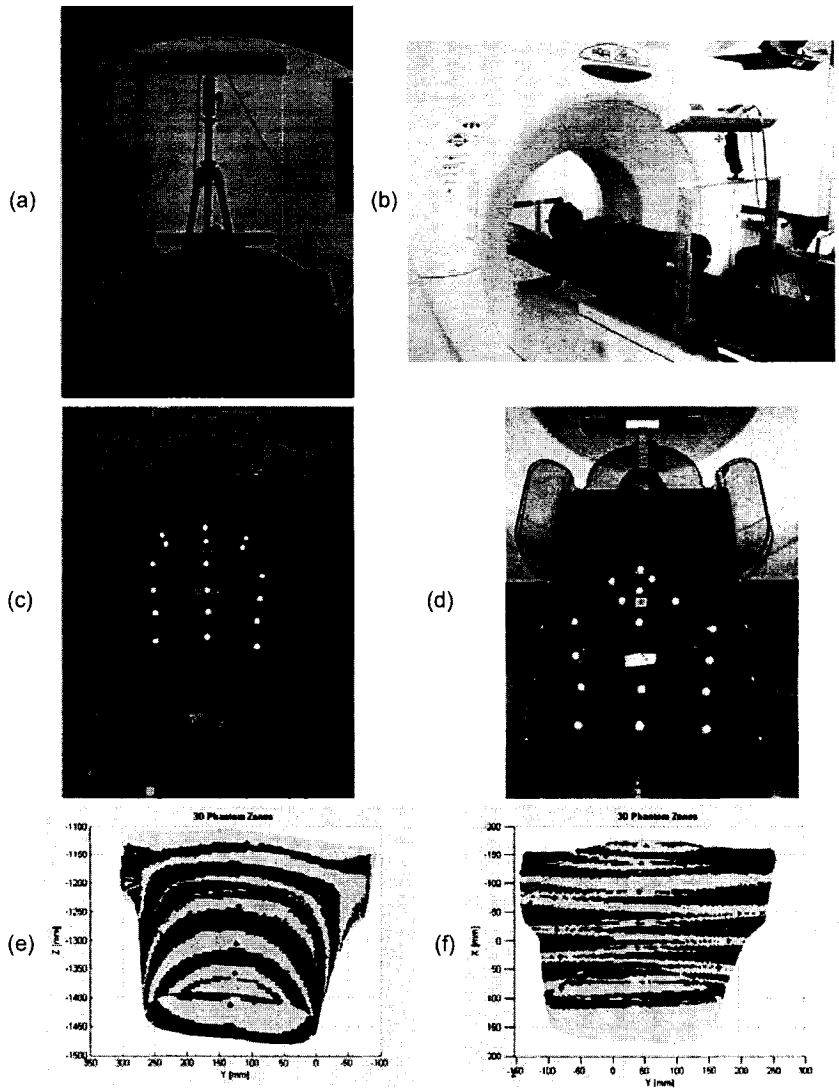

Figure 4–14: Position sensor superior (a) and at 1.3 m from the anthropomorphic phantom, 30° angle of view: ghost marker-free pattern built with 18 reflective markers (c) and coverage of the phantom by the ghost zones of the 18 reflective markers (e). Position sensor inferior (b) and at 1.2 m from the anthropomorphic phantom, 45° angle of view: ghost marker-free pattern built with 18 reflective markers (d) and coverage of the phantom by the ghost zones of the 18 reflective markers (f).

was observed when the Polaris system was used to report the position of multiple reflective markers.

Ghost markers occur when two or more reflective markers are coplanar with each other and with the sensors of the Polaris position sensor. Then, for each pair of two markers which are coplanar with the sensors, three or four markers will be reported by the position sensor. This uncertainty in the number of ghost markers is a result of the finite extent of the sensor, especially along position sensor X axis. A "ghost volume", that contains all possible planes defined by the marker and arbitrary points inside the finite extent of the sensors, was generated for each marker. If another marker enters this volume, ghost markers are reported by the position sensor. A "ghost zone" results from the intersection between the ghost volume and the surface on which the markers lie. Ghost zones can have different shapes, extents and locations, as a function of the shape of the surface on which the markers lie, the angle of view of the position sensor and the distance between the position sensor and the markers to which the ghost zones correspond. The knowledge on the origin of ghost markers was used to avoid their appearance by designing ghost marker-free patterns.

The location of the position sensor was found to be very important in the reduction of the extent of the ghost zones. After studying the shape of the ghost zones for markers taped on an anthropomorphic phantom, it was concluded that the ghost zones were narrower when the position sensor was placed superior to the anthropomorphic phantom, compared to the inferior configuration. Therefore, the superior configuration was chosen for subsequent use of the Polaris system in the 4D CT data acquisition protocol.

CHAPTER 5
4D CT SCANNING PROTOCOL USING A HELICAL SINGLE-SLICE CT SCANNER

Four-dimensional radiotherapy aims to highly conformal dose delivery to lung and breast tumors in the presence of respiratory-induced motion/deformation of the internal anatomy. Four-dimensional radiotherapy accounts for respiratory-induced motion during imaging, planning and radiation delivery and requires a 4D CT image from which the internal anatomy motion as a function of the respiratory phase can be quantified. First, a complete CT data set that contains images from each phase of the respiratory cycle is obtained. Then, based on the anatomic information reconstructed for each respiratory phase, treatment planning is performed for each respiratory phase and the radiation delivery is adapted to the changing anatomy while progressing through the respiratory cycle. Successful implementation of the entire procedure is directly related to the ability to acquire 4D CT data sets with minimal motion artifacts.

The various approaches adopted to acquire 4D CT data sets were described in Section 3.3. Acquisition protocols that use multi-slice CT scanners, operated in either helical or ciné modes, can collect 4D CT data sets with very good spatial and temporal resolution and during fairly short acquisition times. However, CT simulations are currently performed with single-slice CT scanners operated in helical

mode which are readily available in a radio-oncology clinic. It seems therefore more convenient to use this kind of scanners in a 4D CT data acquisition protocol.

This chapter describes a novel 4D CT data acquisition protocol that uses a helical, single-slice CT scanner. The 4D CT data acquisition process is presented in *Section 5.1*: the CT scanning protocol, as well as the choice of the two sets of scanning parameters that were evaluated, are explained in Subsection 5.1.1; Subsection 5.1.2 describes the motion phantom on which the scanning protocol was tested; the use of the Polaris system for real-time acquisition of the external respiratory signal during CT scanning is explained in Subsection 5.1.3. *Section 5.2* details the 4D CT volume reconstruction process and *Section 5.3* describes the image analysis performed on the resulting 4D CT images: the spatial resolution of the 4D CT images is evaluated in Subsection 5.3.1 and a comparison between 4D CT and conventional protocols in scanning the moving phantom is performed in Subsection 5.3.2.

5.1 4D CT data acquisition

5.1.1 CT scanning protocol

A novel CT scanning protocol for 4D CT data acquisition was evaluated: *3 helical scans, each initiated at a different respiratory phase*, are acquired using a single-slice Philips AcQSim CT scanner.

Three quantities are important in achieving an optimal 4D CT data set: spatial resolution, temporal resolution and number of phases that can be reconstructed in a single respiratory cycle [32]. These three quantities are dependent on the respiratory

period T_{res} and the CT scan parameters: slice thickness S, pitch[1] p, gantry rotation period T_{rot} and spacing between slices *INDX*.

The *spatial resolution* of the 4D CT data obtained after one helical CT scan is the gap between slices from successive respiratory cycles, *i.e.*, the gap region in which no CT data are acquired at a particular phase. Ideally, the gap between adjacent slices at the same phase should be minimal or non-existent.

If the pitch p is defined as number of slices per gantry rotation, for a slice thickness S, the table increments a distance pS per gantry rotation. The table therefore travels at a speed pS/T_{rot} and in a single respiratory period T_{res} it will travel a distance pST_{res}/T_{rot}. The gap Z_{gap} between slices from successive respiratory cycles (*i.e.*, spatial resolution) is therefore given by:

$$Z_{gap} = S(p\frac{T_{res}}{T_{rot}} - 1)\,. \tag{5.1}$$

The *temporal resolution* of the 4D CT data obtained after one scan is the time elapsed between the acquisition of successive slices. A lower temporal resolution corresponds to a smaller time interval over which data are acquired for each slice, thus reducing image blurring and motion-induced artifacts.

For a 180° reconstruction algorithm and a fan beam CT geometry with the detector bank subtending an angle Φ, the data for one complete slice are acquired with a gantry rotation of $\pi + \Phi$ [50]. That is, data are acquired in a fraction, $f = (\pi + \Phi)/2\pi$, of a rotation which requires a time fT_{rot}. The temporal resolution

[1] Defined as the ratio of couch advance in one gantry rotation to slice thickness.

is therefore given by:

$$\Delta T = f\, T_{rot} = \frac{\pi + \Phi}{2\pi}\, T_{rot}\,. \tag{5.2}$$

For the scanners with an adjustable fraction f, the smallest value should be used for the best temporal resolution. For the scanner used in this study the only value available was $f = 0.713$, corresponding to a detector angle $\Phi = 76.8°$.

The spatial and temporal resolution, represented by Eqs. (5.1) and (5.2) *must be minimized to achieve an optimal 4D CT data set.* However, Eqs. (5.1) and (5.2) imply that there is a tradeoff with respect to the rotation time T_{rot}. That is, faster rotations yield better temporal resolution but degrade spatial resolution. There is no such tradeoff with regard to the pitch p – a smaller pitch results in a better spatial resolution and does not affect the temporal resolution. However, using a smaller pitch will increase the total time for a scan and will limit the length of the region that can be scanned before the x-ray tube heat is exceeded.

The *number of phases or slices N that can be reconstructed in a single respiratory cycle* is given by the number of slices acquired per second $pS/T_{rot}INDX$ times the period of a breathing cycle. To avoid overlapping between successive respiratory cycles, one less phase or slice has to be considered per respiratory cycle. Therefore N is given by:

$$N = \frac{p\,S}{T_{rot}\,INDX} \cdot T_{res} - 1\,. \tag{5.3}$$

However, the number of slices that can be acquired per breathing cycle is $T_{res}/f\,T_{rot}$ and is usually less than the number of reconstructed slices. Therefore, during the reconstruction process, *reconstructed slices or phases* are generated by interpolating data from neighboring *acquired slices.*

Two CT scanning techniques, whose parameters are summarized in Table 5–1, were evaluated for 4D CT data acquisition.

Table 5–1: Evaluated scanning techniques and their parameters.

Technique	T_{rot} [s]	**ΔT [s]**	p	S [mm]	*INDX*	$T_{res}[s]$	$\mathbf{Z_{gap}}$ **[mm]**	**N**
						4	**15**	**6**
1	1	**0.713**	1	5	3	5	**20**	**7**
						6	**25**	**9**
						4	**9**	**5**
2	1	**0.713**	1	3	2	5	**12**	**7**
						6	**15**	**8**

For both techniques, the standard tube potential for lung acquisitions was used (130 kVp) but, in order to reduce both patient imaging dose and tube heating, the tube current was set to 130 mA (as opposed to 230 mA for standard lung acquisitions). The *small gantry rotation period* offers a temporal resolution of 0.713 s. A *small pitch* was chosen so that the table travels slowly enough to acquire sufficient data for 3D CT image reconstruction over the entire respiratory cycle.

The *slice thickness* and *spacing* offer a compromise between spatial resolution and total time needed for a helical scan. Spatial resolution will be further improved by the 3 helical scan acquisitions: the number of slices acquired per respiratory phase will increase by increasing the number of scans and if each scan starts at a different respiratory phase, the slices added to a given respiratory phase with each scan will be different from the slices already acquired at that respiratory phase.

Scanning a 25-cm long region of the phantom's thorax required 84 slices, 23% tube heating and 3 min when the first technique was used and 125 slices, 33% tube

heating and 5 min when the second technique was used. For each slice, 0.9375-mm square pixels were arranged in a 512x512 matrix.

Table 5–1 shows that spatial resolution decreases when the respiratory period increases. *In what follows the reduced spatial resolution was chosen to illustrate the performances of the 4D CT data acquisition procedure* and therefore a respiratory period of 6 s was used to generate all the results below.

5.1.2 Motion phantom

The 4D CT data acquisition protocol was tested on an anthropomorphic phantom with which a realistic respiratory motion was simulated. The phantom was placed on an inflatable mattress driven by an air pump controlled by a pulsing power supply (Fig. 5–1). The period and amplitude of the induced respiratory motion can be varied, allowing the investigation of a full range of clinical conditions.

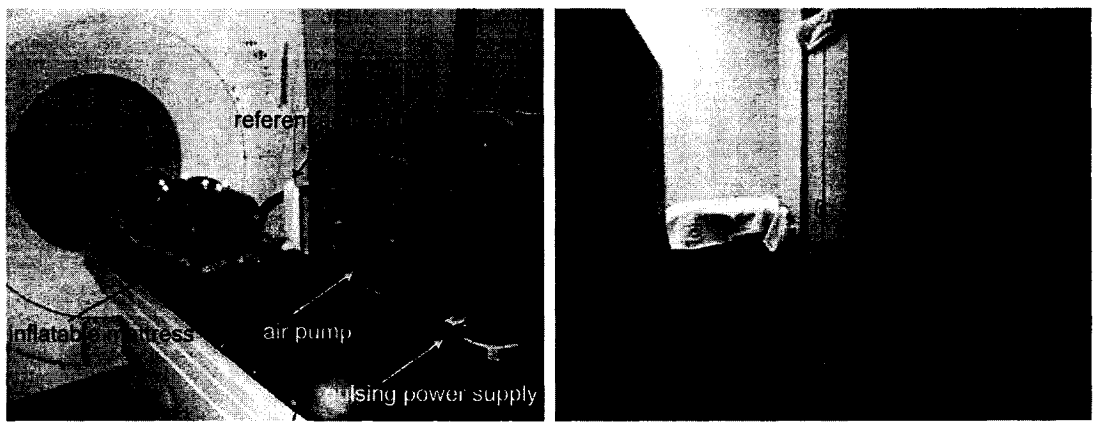

Figure 5–1: Experimental setup: (a) anthropomorphic phantom that mimics patient's respiration motion; (b) location of the Polaris system.

Clinical studies on patients shown respiratory periods ranging from 3 to 6 s and SI, AP and LR respiratory amplitudes of about 1 cm [69, 99, 130]. In what follows, the *AP amplitude and time period of the respiratory motion were set at 1 cm and 6 s, respectively.*

5.1.3 External respiratory signal

For real-time acquisition of the external respiratory signal during CT scanning, *the Polaris tracking system was located behind the CT gantry, superior to the anthropomorphic phantom* (Fig. 5–1).

The motion of 7 reflective markers was measured: 6 markers placed on the anthropomorphic phantom's thorax and 1 reference marker placed on a post attached to the scanner table (Fig. 5–1.a). During the CT acquisition, the respiratory motion of the 6 markers placed on the phantom is obtained by subtracting the displacement due to the table movement (*i.e.*, motion of the reference marker) from the motion reported by the Polaris system for the 6 markers.

The real-time tracking of all 6 markers was not necessary for the anthropomorphic phantom measurements, because any of them can generate the respiratory signal needed for the 4D CT scanning procedure. However, during patients scanning, different amplitudes and correlations with the tumor motion will characterize the respiratory signals coming from the 6 markers. Therefore, tracking them all in real time would allow to choose the best external respiratory signal to be used in the 4D CT data acquisition.

The location of the infrared tracking system and the 7 markers was optimized to obtain a ghost marker-free pattern at the beginning of each scan (Subsection 4.4.3).

As shown in Subsections 4.4.2 and 4.4.3, ghost zones associated to each marker are narrower when the infrared tracking system is placed superior to the phantom and therefore the probability of ghost markers appearance is reduced compared to a configuration where the infrared tracking system was placed inferior to the phantom.

Software was developed in Matlab (The MathWorks Inc.) for the post-acquisition processing of the external respiratory signal:

- The first step in the post-acquisition processing is the representation of the *reference marker position as a function of time* (Fig. 5–2).

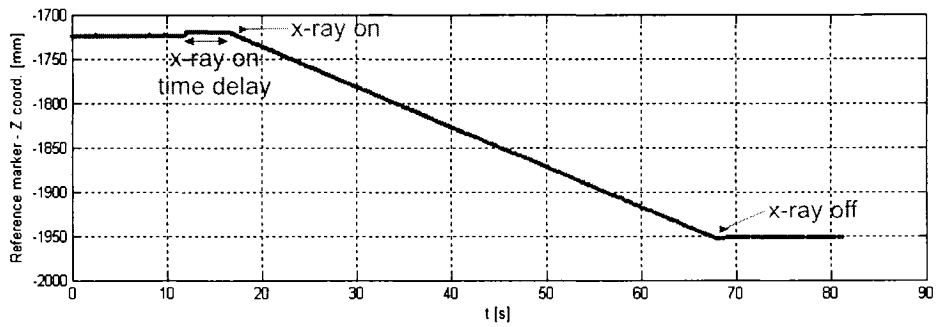

Figure 5–2: Reference marker position as a function of time. The scanner x-ray ON time delay, the beginning and end of the acquisition are indicated.

This allows the determination of the *acquisition time* as well as the *scanner x-ray ON time delay*[2] . The acquisition of a single scan takes 49 s when technique 1 is used and 83 s when technique 2 is used. The scanner x-ray ON average time delay is 4.8 s; the variation of this parameter around its average

[2] The delay between the time of the x-ray ON light and the actual starting time of slice acquisition.

value will complicate later the starting of the three individual scans at different respiratory phases[3] .

- The second step in the post-acquisition processing consists of the *elimination of the ghost markers* from the data flow. Figure 5–3.a shows the markers positions in time, as they were reported by the Polaris system. Towards the end of the scan, as the scanner table moves and the relative position of the markers changes with respect to the infrared tracking system, ghost markers are generated. In Fig. 5–3.b all ghost markers were removed.
- Finally, the movement of the scanner table (*i.e.*, reference marker's movement, see Fig. 5–3.b) is subtracted from marker motion to obtain the external respiratory signal (Fig. 5–3.c).

5.2 4D CT volume reconstruction

The start of the CT scan was used to correlate the CT acquisition with the external respiratory signal: in the Polaris coordinate system, the scan started when the reference marker started to move. Figure 5–4 illustrates the correlation between the respiratory signal and the CT acquisitions during a 4D CT scanning procedure. Using this correlation, the slices can be displayed on the respiratory trace, at the time when their acquisition occurred. In Fig. 5–6 the CT slices (stars) are plotted on the respiratory trace (full line) for both techniques used in the 4D CT acquisitions. As predicted in Subsection 5.1.1, the two techniques led to the same number of

[3] External signals are accepted by the Philips AcQSim CT scanner only during respiratory gating procedures.

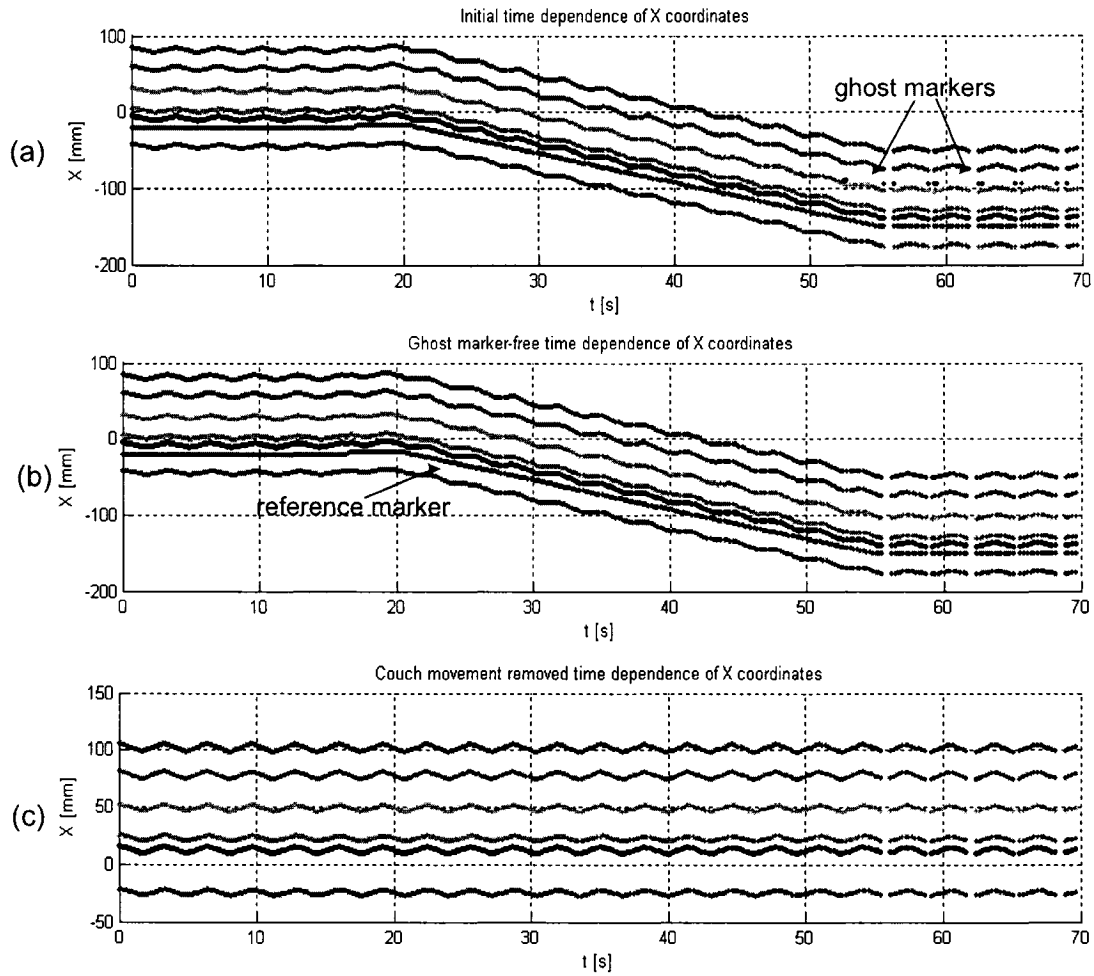

Figure 5–3: Post-acquisition processing of the external respiratory signal: (a) real and ghost markers position in time, as reported by the Polaris system (ghost markers are indicated); (b) real markers position in time; (c) external respiratory signal from all six markers.

phases/slices that can be reconstructed per respiratory cycle, *i.e.*, 9 phases for a 6-s respiratory cycle.

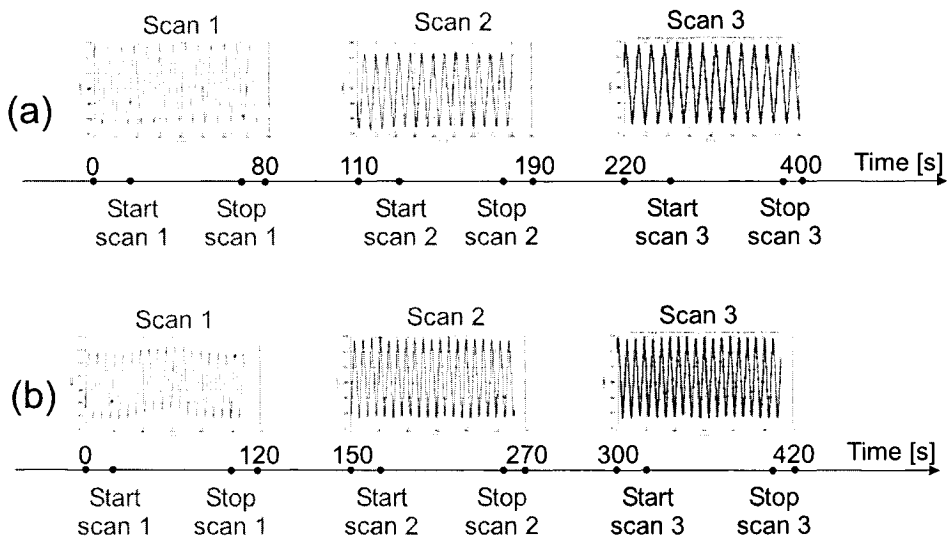

Figure 5–4: Generic timeline diagram illustrating the breathing cycle for each of the three CT acquired with technique 1 (a) and 2 (b).

Each respiratory cycle was then divided into *8 equi-spaced stages*, based on the phase of the respiratory signal (Fig. 5–5).

At the end of the three scans, the CT slices acquired were sorted into eight image bins, according to their corresponding phases in the respiratory cycle. The collection of binned images obtained over a complete respiratory cycle constitutes a 4D CT image set: *images from one bin are used to reconstruct the scanned region at a given moment/phase of the respiratory cycle.*

The purpose of having 3 CT scan acquisitions per 4D CT study was to increase the number of different images in each bin and therefore improve the spatial resolution of the final 4D CT data set. In order to add different slices per phase bin with each scan, the phase of the first slice acquired in each scan had to be different from the other scans belonging to the same 4D CT data acquisition (Fig. 5–6).

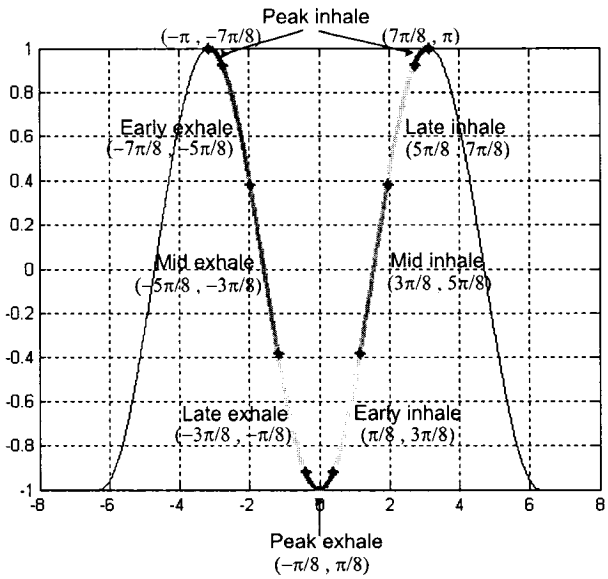

Figure 5–5: Each respiratory cycle is divided into eight equi-spaced stages. The phase extent for each stage is indicated.

Figure 5–7 shows the variation of the 4D CT volume coverage per phase bin as a function of the number of scans acquired with technique 1 (Figs. 5–7.a to 5–7.c) and technique 2 (Figs. 5–7.d to 5–7.f), respectively. The volume coverage for one phase bin was calculated as the ratio of the number of slices acquired to the total number of slices needed to reconstruct the scanned volume at that phase; the total number of slices needed to reconstruct the scanned volume at one phase is equal to the number of slices acquired during one scan (*i.e.*, 84 and 125 slices for technique 1 and 2, respectively). If scanning technique 1 is used, the mean volume coverage is 12.5, 25 and 37.5 % if 1, 2 and 3 scans are used to acquire the 4D CT data, respectively. Almost identical results are obtained if scanning technique 2 is used: the mean volume coverage is 12.5, 25 and 37.4 % for 1, 2 and 3 scans, respectively.

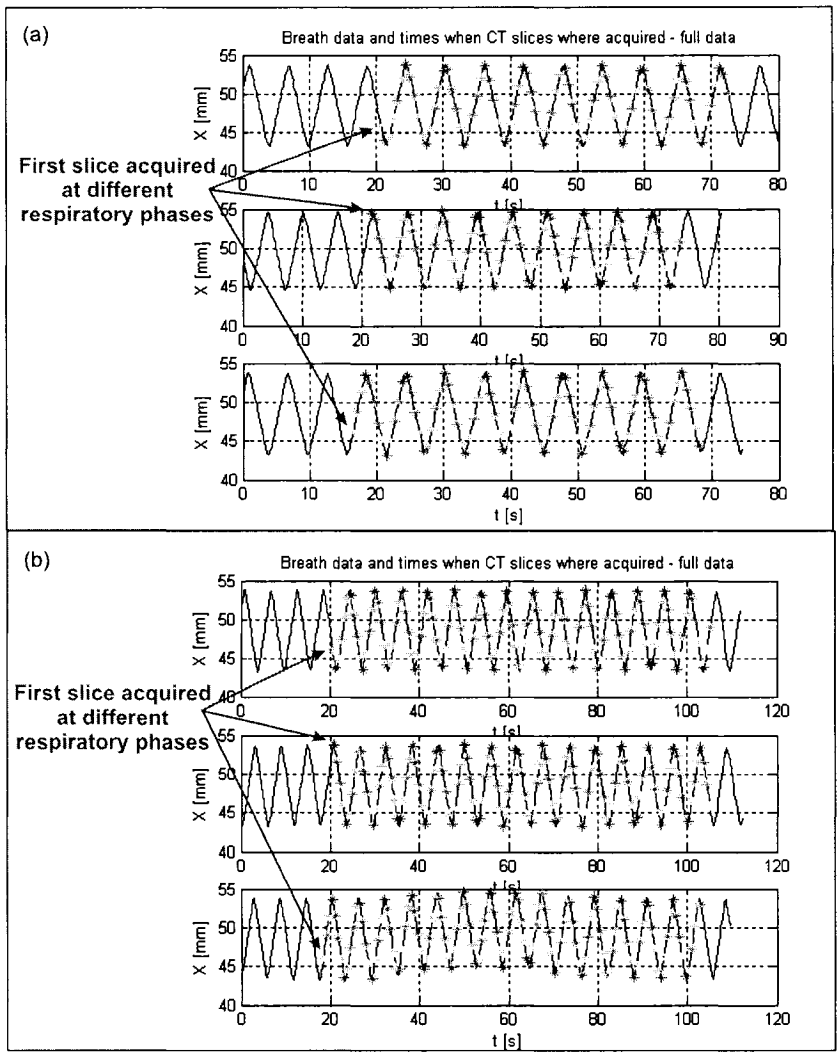

Figure 5–6: Correlation of the CT acquisition with the external respiratory signal – CT slices (stars) displayed on the respiratory trace (full line) for the 3 scans acquired with scanning technique 1 (a) and 2 (b). Slices belonging to different image bins are represented in different colors (see also Fig. 5–5).

The linear increase of the mean volume coverage with the number of scans proves that within each scan new, different slices were added.

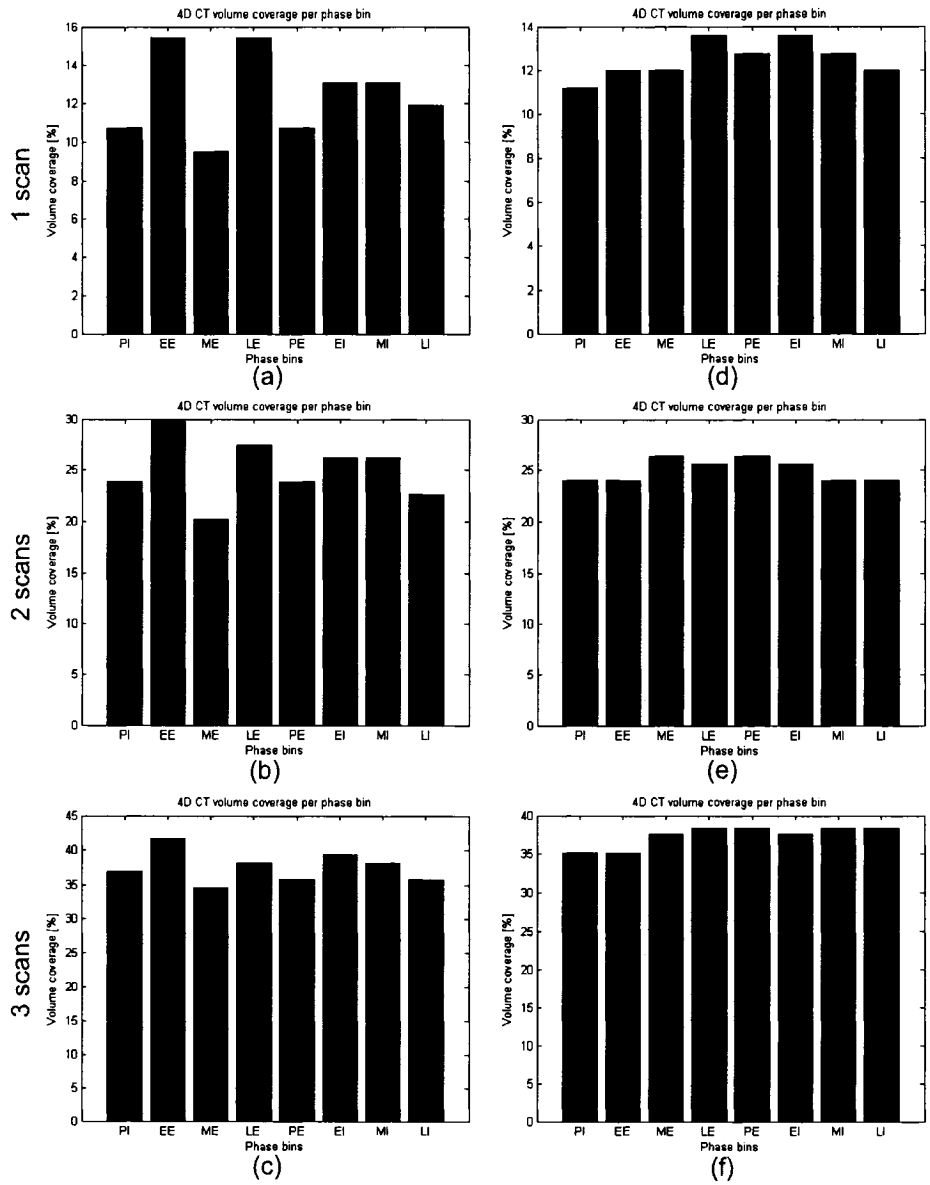

Figure 5–7: 4D CT volume coverage per phase bin when 1, 2 and 3 scans are acquired with technique 1 (a-c) and technique 2 (d-f), respectively. The abbreviations for the phase bins are: PI - peak inhale; EE - early exhale; ME - mid exhale; LE - late exhale; PE - peak exhale; EI - early inhale; MI - mid inhale and LI - late inhale.

Figures 5–8 and 5–9 are an illustration of the volume reconstruction process. The slices acquired at a given respiratory phase (in this case, peak exhale) are shown in Figs. 5–8.a and 5–8.c for technique 1, and Figs. 5–9.a and 5–9.c for technique 2. From these available slices, linear interpolation is used to obtain the scanned volume at peak exhale: Figs. 5–8.b and 5–8.d for technique 1, and Figs. 5–9.b and 5–9.d for technique 2.

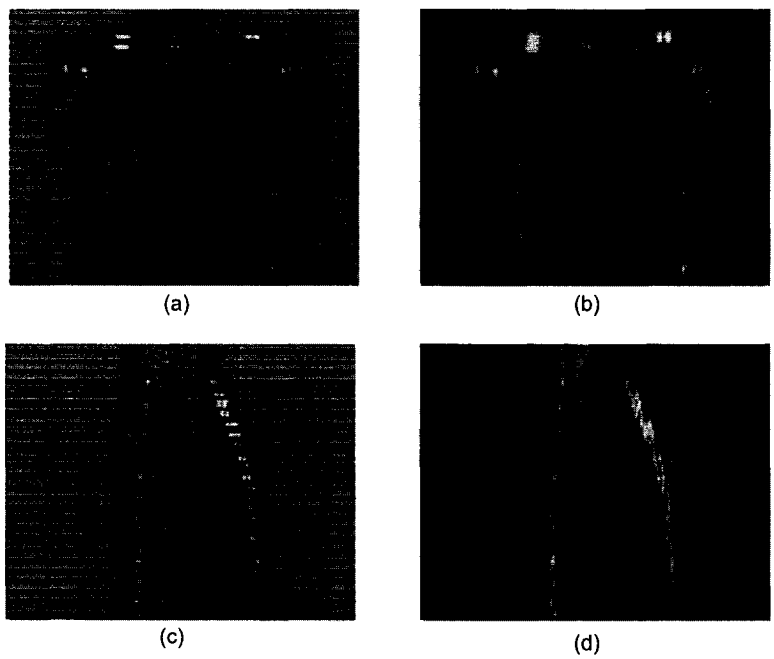

Figure 5–8: Volume reconstruction at peak exhale, when scanning technique 1 was used:
(a) and (b) coronal view; (c) and (d) lateral view (compressed, 256x256 images)
(a) and (c) slices available for volume reconstruction; (b) and (d) reconstructed volume, using linear interpolation.

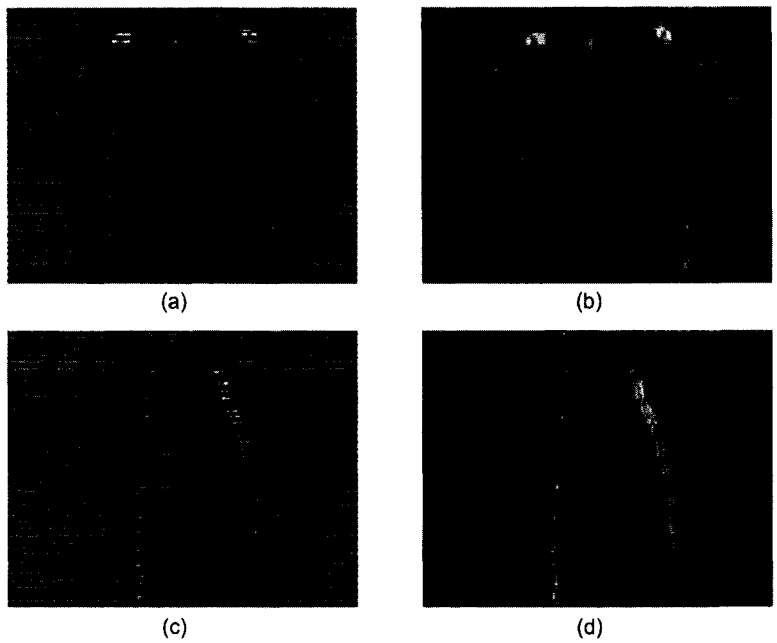

Figure 5–9: Volume reconstruction at peak exhale, when scanning technique 2 was used:
(a) and (b) coronal view; (c) and (d) lateral view (compressed, 256x256 images)
(a) and (c) slices available for volume reconstruction; (b) and (d) reconstructed volume, using linear interpolation.

5.3 4D CT image analysis

5.3.1 Spatial resolution

When images reconstructed from the 4D CT data obtained with scanning techniques 1 and 2 are compared (*e.g.*, Figs. 5–8.b or 5–8.d compared with Figs. 5–9.b or 5–9.d), *the superior quality of 4D CT images acquired with technique 2 is evident.*

Table 5–2 shows how the spatial resolution varies with the number of scans, for each scanning technique.

Table 5–2: Improvement of spatial resolution with the increased number of CT scan acquisitions.

Respiratory phase	Technique 1			Technique 2		
	Average/maximal **spatial resolution** [mm]			**Average**/maximal **spatial resolution** [mm]		
	1 scan	2 scans	**3 scans**	1 scan	2 scans	**3 scans**
Peak inhale	28.1/30.0	12.8/18.0	**8.1**/12.0	17.1/18.0	8.3/12.0	**5.8**/10.0
Early exhale	19.0/27.0	10.3/18.0	**7.2**/12.0	15.9/18.0	8.3/12.0	**5.6**/8.0
Mid exhale	28.3/30.0	14.1/18.0	**8.4**/12.0	15.9/18.0	7.6/12.0	**5.3**/8.0
Late exhale	19.0/27.0	10.8/18.0	**7.9**/12.0	15.1/18.0	8.0/12.0	**5.3**/8.0
Peak exhale	28.5/30.0	12.5/18.0	**8.5**/12.0	16.1/18.0	7.6/12.0	**5.1**/8.0
Early inhale	22.8/30.0	11.4/18.0	**7.7**/12.0	15.1/18.0	7.8/12.0	**5.3**/8.0
Mid inhale	22.5/30.0	11.3/18.0	**7.9**/12.0	16.1/18.0	8.3/12.0	**5.2**/8.0
Late inhale	25.0/30.0	12.5/18.0	**8.1**/12.0	16.0/18.0	8.0/12.0	**5.1**/8.0

The mean (averaged over all the respiratory phases) spatial resolution for *one scan* acquired with technique 1 is 24.2 mm, in agreement with the theoretical value (25 mm) predicted in Table 5–1. Similarly, for technique 2, the experimental spatial resolution is 15.9 mm, fairly close to the theoretical value (15 mm) predicted in Table 5–1.

Over all *3 scans*, scanning technique 2 generates images with a better spatial resolution than scanning technique 1: the mean (over all the respiratory phases) spatial resolution for technique 2 is 5.3 mm, compared to 8.0 mm for technique 1.

5.3.2 Images of the moving phantom obtained with 4D CT and conventional scanning protocols

4D CT images of the moving phantom were compared to images of the static and moving phantom, obtained with conventional scanning.

Figs. 5–10.a and 5–11.a show coronal and lateral views of the conventional scan of the static phantom, acquired with technique 1. When the same conventional scanning is used for the moving phantom, the quality of the images drastically degrades (Figs. 5–10.b and 5–11.b). *When the 4D CT data acquisition protocol is used to scan the moving phantom, the motion artifacts are completely removed from the reconstructed image*: see Figs. 5–10.c and 5–11.c, for images reconstructed at peak exhale and Figs. 5–10.d and 5–11.d, for images reconstructed at peak inhale. The advantages of the 4D CT approach are less visible in the axial view (Fig. 5–12), because there is no phantom motion in the SI direction.

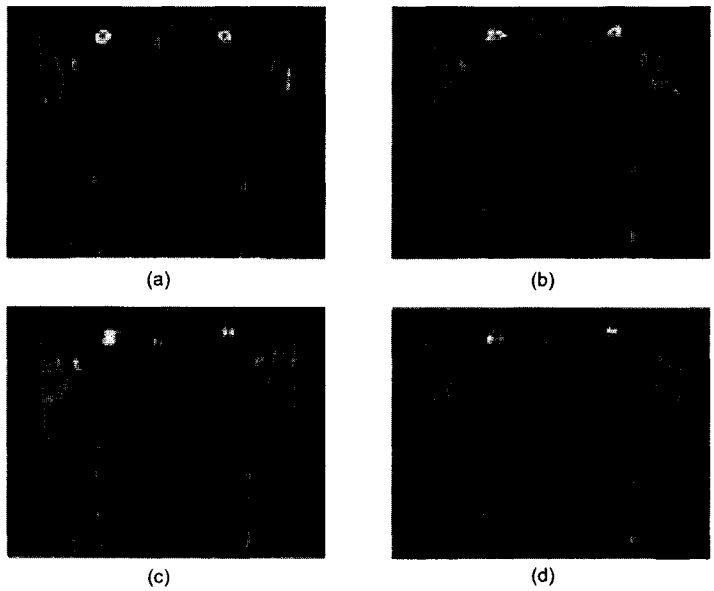

Figure 5–10: Coronal *conventional images* of the (a) static and (b) moving phantom compared to coronal *4D CT images* of the moving phantom at (c) peak exhale and (d) peak inhale (compressed, 256x256 images).
4D CT data were obtained with *scanning technique 1.*

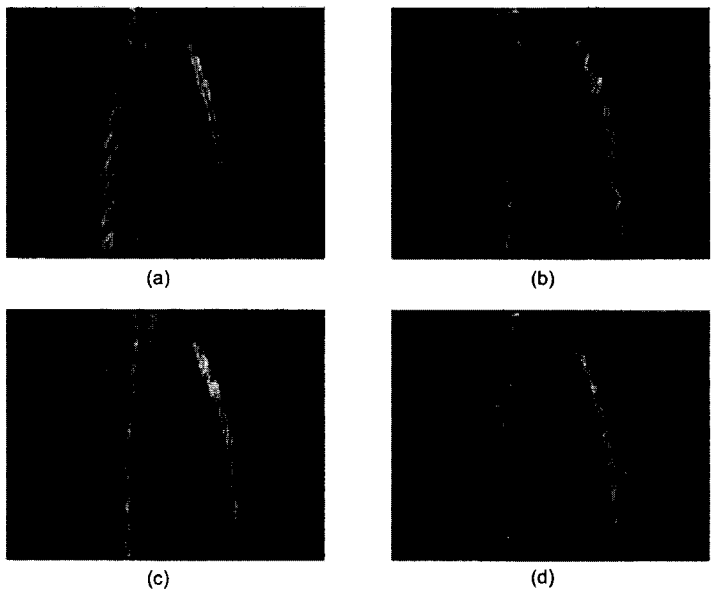

Figure 5–11: Lateral *conventional images* of the (a) static and (b) moving phantom compared to lateral *4D CT images* of the moving phantom at (c) peak exhale and (d) peak inhale (compressed, 256x256 images).
4D CT data were obtained with *scanning technique 1.*

The same comparison, but this time for scanning technique 2, is illustrated in Figs. 5–13 and 5–14. Figs. 5–13.a and 5–14.a show coronal and lateral views of the conventional scan of the static phantom. The conventional images of the moving phantom are shown in Figs. 5–13.b and 5–14.b, and the motion artifacts are clearly visible. Much better images of the moving phantom are obtained when the 4D CT data acquisition protocol is used: Figs. 5–13.c and 5–14.c show 4D CT images reconstructed at peak exhale and Figs. 5–13.d and 5–14.d show 4D CT images reconstructed at peak inhale. As there is no phantom motion in the SI direction,

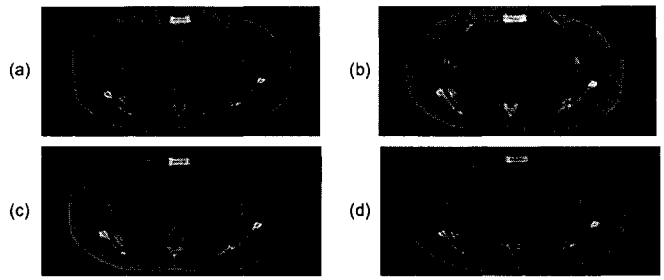

Figure 5–12: Axial *conventional images* of the (a) static and (b) moving phantom compared to axial *4D CT images* of the moving phantom at (c) peak exhale and (d) peak inhale (compressed, 256x256 images).
4D CT data were obtained with *scanning technique 1.*

there is no significant difference between conventional and 4D CT axial images (Fig. 5–15).

From a comparison of Figs. 5–13 and 5–14 with Figs. 5–10 and 5–11, it appears that the *4D CT images of the moving phantom acquired with scanning technique 2 reproduce more accurately the image of the static phantom than the 4D CT images acquired with scanning technique 1.*

5.4 Summary

This chapter presented a novel scanning protocol for 4D CT data acquisition: 3 helical scans are acquired with a single-slice Philips AcQSim CT scanner, simultaneously with the real-time tracking of several markers placed on the torso of an anthropomorphic phantom to which a realistic respiratory motion was induced. Each CT scan was initiated at a different respiratory phase, and at the end of the three scans, CT data was sorted into different phase bins according to the externally recorded respiratory signal. The CT images from each phase bin were then used to reconstruct the scanned volume at 8 respiratory phases.

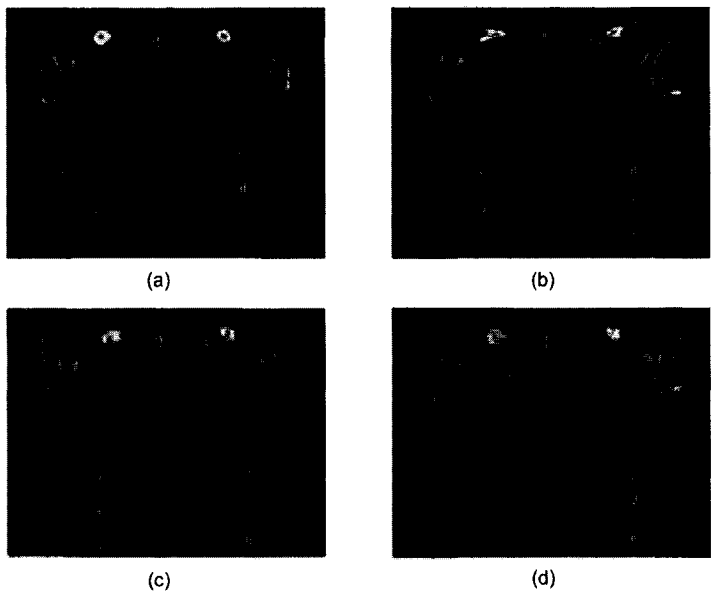

Figure 5–13: Coronal *conventional images* of the (a) static and (b) moving phantom compared to coronal *4D CT images* of the moving phantom at (c) peak exhale and (d) peak inhale (compressed, 256x256 images).
4D CT data were obtained with *scanning technique 2.*

Two scanning techniques were evaluated, with the aim of achieving a good compromise between the spatial and temporal resolution of the final 4D CT data set. Small pitch values were chosen so that the scanner table travels slowly enough to acquire sufficient data over one respiratory cycle. The slice thickness and spacing chosen for each scanning technique offered different levels of compromise between spatial resolution and acquisition time for each helical scan: technique 1 required less scanning time (3 min/scan), but its spatial resolution was quite high (24 mm); the spatial resolution for technique 2 was lower (16 mm) but its acquisition time was

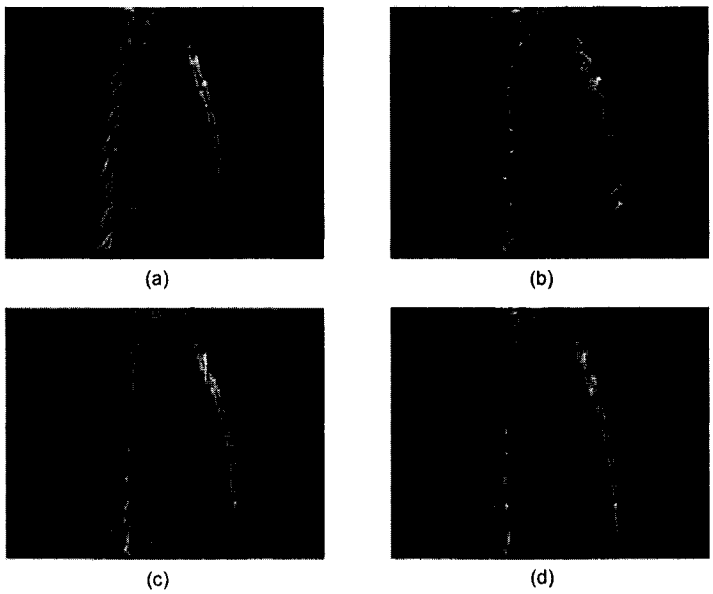

Figure 5–14: Lateral *conventional images* of the (a) static and (b) moving phantom compared to lateral *4D CT images* of the moving phantom at (c) peak exhale and (d) peak inhale (compressed, 256x256 images).
4D CT data were obtained with *scanning technique 2.*

longer (5 min/scan). For both techniques, a low tube current was chosen (130 mA) to reduce both patient imaging dose and tube heating.

The performances of the two techniques were tested on 4D CT acquisitions on a moving anthropomorphic phantom, to which a realistic respiratory motion was induced: 6-s period and 1-cm amplitude in the AP direction. The images in the 4D CT data set showed almost no motion artifacts compared to the conventional spiral CT image.

The two techniques offer the same temporal resolution for the final 4D CT data set: 0.713 s, better than the values reported by other groups [32, 152]. Over all 3

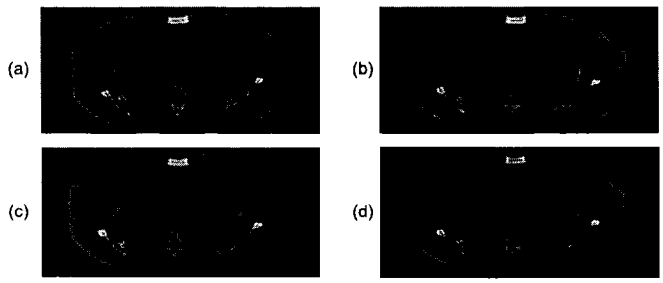

Figure 5–15: Axial *conventional images* of the (a) static and (b) moving phantom compared to axial *4D CT images* of the moving phantom at (c) peak exhale and (d) peak inhale (compressed, 256x256 images).
4D CT data were obtained with *scanning technique 2.*

scans acquired in one 4D CT study, technique 1 and 2 result in spatial resolutions of 8.0 and 5.3 mm, respectively. Of both techniques, only the second one offers a spatial resolution inside the 4-6 mm of spatial resolution reported in the literature [32, 152].

In conclusion, the proposed 4D CT scanning protocol using technique 2 generates 4D CT data sets whose temporal and spatial resolutions are similar with the values reported in the literature. The fact that the technique used for each scan is not very demanding on the x-ray tube, offers an advantage over the existing 4D CT scanning protocols: the scan length could be extended from only 10 cm [32, 152] to 25 cm. In the treatment planning for lung cancer this means that motion/deformation as a function of the respiratory phase can be quantified for the whole anatomy including both lungs as opposed to only a small region around the PTV.

CHAPTER 6
CONCLUSIONS

The main goal of conformal radiation techniques, such as standard 3D conformal radiotherapy and IMRT, is to improve local tumor control through dose escalation to target volumes while at the same time sparing surrounding healthy tissue. Several studies showed that for some sites (*e.g.*, lung, prostate) dose-per-fraction escalation results in a higher probability of tumor control and hence prolonged survival. Conformal radiotherapy allows dose-per-fraction escalation but accurate PTV delineation is essential to achieve this goal. Failure to properly define the PTV will jeopardize the curative intent of the treatment through either inadequate tumor coverage (geographic miss), irradiation of an unnecessary volume of healthy tissue, or both. Reducing the uncertainty in the extent of microscopic disease (*i.e.*, CTV to GTV) as well as the patient setup uncertainty and the organ motion (*i.e.*, PTV to CTV) should potentially lead to increased accuracy in dose delivery.

Respiratory motion is known to be the largest intra-fractional organ motion and the most significant source of uncertainty in treatment planning for thorax and upper abdomen lesions. The many individual characteristics of breathing and the variation in motion associated with tumor location and pathology lead to distinct individual patterns in displacement, direction and phase of respiratory-induced tumor motion. Therefore, there are no general patterns of respiratory behavior and correlation with tumor motion that can be assumed for a particular patient.

In the first part of this thesis the effects of the breathing motion in conformal radiotherapy as well as the various strategies used to minimize these effects were reviewed. If the breathing-induced anatomic changes are not explicitly accounted for in conformal therapies, errors can be introduced during the imaging, planning and delivery steps *(Chapter 2).* The various methods that have been developed to explicitly account for respiration motion in radiotherapy include minimization, correction and incorporation schemes *(Chapter 3).*

Although in some patients simple interventions can be used to reduce organ motion effects, the methods used to compensate for organ motion are often resource intensive. Their implementation has therefore to be weighted against the potential risk that organ motion may compromise clinical outcomes and may potentially mask the advantages of conformal therapies. Moreover, although these approaches may be successful in some patients, it is important to confirm that motion is reduced in all three directions and that the tumor position with the intervention is reproducible before reducing the target margins. Careful prospective trials are mandatory to prove the usefulness of each method before its widespread application.

6.1 Summary of the work performed

Chapter 4 described the implementation of a Polaris system as a real-time tracking device for the acquisition of the external respiratory signal during the 4D CT scanning procedure. First, the accuracy and reproducibility of relative displacement measurements with the Polaris system were evaluated. Then the occurrence of ghost markers, observed when the Polaris system is used to report the position of multiple reflective markers, was explained. It was found that ghost markers appear when two

or more reflective markers are coplanar with each other and with the sensors of the Polaris system. Then, for each pair of two markers which are coplanar with the sensors, three or four markers will be reported by the position sensor. This uncertainty in the number of ghost markers is a result of the finite extent of the sensors.

For each marker, a "ghost volume" that contains all possible planes defined by the marker and arbitrary points inside the finite extent of the sensors was generated. If another marker enters this volume, ghost markers will be reported by the position sensor.

"Ghost zones", resulting from the intersection between the ghost volume and the surface on which the markers lie, can have different shapes, extents and locations, as a function of the shape of the surface on which the markers lie, the angle of view of the position sensor and the distance between the position sensor and the markers to which the ghost zones correspond. The analysis of the shape of the ghost zones as a function of all these parameters was then used to choose the configuration in which the Polaris system should be placed relative to the CT scan. It was concluded that the ghost zones were narrower when the position sensor was placed superior to the anthropomorphic phantom, compared to the inferior configuration. Therefore, the superior configuration was chosen for subsequent use of the Polaris system in the 4D CT scanning procedure.

During the CT acquisition the position of the markers relative to the Polaris system changes continuously and therefore ghost markers can appear. However, using the knowledge of the ghost markers origin, ghost marker-free patterns could

be build at the beginning of each scan and all ghost markers subsequently appearing could be discarded.

Chapter 5 presented a new scanning procedure for 4D CT data acquisition: three subsequent single-slice helical CT scans were acquired while tracking several markers placed on the chest of an anthropomorphic phantom to which a realistic respiratory motion was induced. Each CT scan was initiated at a different respiratory phase, and at the end of the three scans, the 4D CT data set was generated by sorting all the CT slices in 8 phase bins, according to the externally recorded respiratory signal. The images from each bin were then used to reconstruct the scanned volume at a different phase in the respiratory cycle.

Two scanning techniques were evaluated, with the aim of achieving a good compromise between the spatial and temporal resolution of the final 4D CT data set. The small pitch values as well as the slice thickness and spacing chosen for each scanning technique offered different levels of compromise between spatial resolution and acquisition time for each helical scan: one technique required less scanning time but its spatial resolution was quite high while the spatial resolution for the other technique was lower and its acquisition time was longer.

The performance of both techniques were tested on 4D CT acquisitions on a moving anthropomorphic phantom, with which a realistic respiratory motion was simulated. The 4D CT images showed almost no motion artifacts compared to the conventional spiral CT image. While both techniques offered better temporal resolution for the final 4D CT data than the values reported in the literature, only one of the scanning techniques resulted in a spatial resolution comparable with the

ones obtained by other groups. Moreover, the fact that the scanning techniques used are not very demanding on the x-ray tube allows the extension of the scan length from 10 to 25 cm. In the case of a lung lesion, this translates in scanning the whole thorax as opposed to scanning only a small region around the PTV.

The 4D CT data acquisition protocol described can be implemented on any single-slice CT scanner available in a radio-oncology clinic in order to reduce the motion artifacts usually present in conventional CT acquisitions. However, the 4D CT approach requires special staff participation and increases both the CT simulation time and the imaging dose to the patient. Therefore this technique should be implemented only when the conformal therapy is a clear advantage for the patient.

6.2 Future work

The 4D CT scanning procedure was tested on a phantom to which a *regular respiratory motion* was induced and motion artifacts were almost completely removed from the images obtained. However, both the amplitude and period of a patient respiration can vary from one respiratory cycle to another, affecting therefore the reproducibility of internal anatomy motion and hence the quality of the reconstructed volumes.

For this reason, *training patients to breathe in a regular fashion* is mandatory for the implementation of the 4D CT scanning procedure on patients. Providing *audio prompting* (*e.g.*, "Breathe in", "Breathe out") should improve the reproducibility of the respiration period, while showing patients their respiratory waveform (*i.e.*, *visual feedback*) should control the respiration amplitude.

Audio prompting and visual feedback during 4D CT data acquisitions on patients should therefore result in reliable reconstructed volumes at different moments in the respiratory cycle which can then be used to *calculate the intra-fractional motion of both tumor and surrounding organs.* The 4D CT data can also be used to study the dose distribution as a function of the respiratory phase: the treatment plan can be applied to CT data sets at different phases and then the *dose distribution to target volumes and surrounding organs can be assessed.*

REFERENCES

[1] Adler JR Murphy MJ Chang SD et al. Image-guided robotic radiosurgery. *Neurosurgery*, 44:1299-1307, 1999.

[2] Adler JR Chang SD Murphy MJ et al. The Cyberknife: A frameless robotic system for radiosurgery. *Stereo Funct Neurosurg*, 69:124-128, 1997.

[3] Alasti H Petric MP Catton CN et al. Portal imaging for evaluation of daily on-line setup errors and off-line organ motion during conformal irradiation of carcinoma of the prostate. *Int J Radiat Oncol Biol Phys*, 49:869-884, 2001.

[4] Aoyama H Shirato H Nishioka T et al. Magnetic resonance imaging system for three-dimensional conformal radiotherapy and its impact on gross tumor volume delineation of central nervous system tumors. *Int J Radiat Oncol Biol Phys*, 50:821-827, 2001.

[5] Balter JM Ten Haken RK Lawrence TS et al. Uncertainties in CT-based radiation therapy treatment planning associated with patient breathing. *Int J Radiat Oncol Biol Phys*, 36:167-174, 1996.

[6] Barnes EA Murray BR Robinson DM et al. Dosimetric evaluation of lung tumor immobilization using breath hold at deep inspiration. *Int J Radiat Oncol Biol Phys*, 50:1091-1098, 2001.

[7] Beckham WA Keall PJ Siebers JV. A fluence-convolution method to calculate radiation therapy dose distributions that incorporate random set-up error. *Phys Med Biol*, 47:3465-3473, 2002.

[8] Bel A Vos PH Rodrigus PTR et al. High precision prostate cancer irradiation by clinical application of an off-line patient setup verification procedure, using portal imaging. *Int J Radiat Oncol Biol Phys*, 35:321-332, 1996.

[9] Bel A Petrascu O Van de Vondel I et al. A computerized remote table control for fast on-line patient repositioning: Implementation and clinical feasibility. *Med Phys*, 27:354-358, 2000.

[10] Berson AM Emery R Rodriguez L et al. Clinical experience using respiratory gated radiation therapy: Comparison of free-breathing and breath-hold techniques. *Int J Radiat Oncol Biol Phys*, 60:419-426, 2004.

[11] Bortfeld T Jiang SB Rietzel E. Effects of motion on the total dose distribution. *Semin Radiat Oncol*, 14:41-51, 2004.

[12] Bortfeld T Jokivarsi K Goitein M et al. Effects of intra-fraction motion on IMRT dose delivery: Statistical analysis and simulation. *Phys Med Biol*, 47:2203-2220, 2002.

[13] Bouchet LG Meeks SL Goodchild G et al. Calibration of three-dimensional ultrasound images for guided radiation therapy. *Phys Med Biol*, 46:559-577, 2001.

[14] Brenner DJ Martinez AA Edmundson GK et al. Direct evidence that prostate tumors show high sensitivity to fractionation (low α/β ratio), similar to late-responding normal tissue. *Int J Radiat Oncol Biol Phys*, 52:6-13, 2002.

[15] Bryan PJ Custar S Haaga JR et al. Respiration movement of the pancreas: An ultrasonic study. *J Ultrasound Med*, 3:317-320, 1984.

[16] Buchali A Koswig S Dinges S et al. Impact of the filling status of the bladder and rectum on their integral dose distribution and the movement of the uterus in the treatment planning of gynecological cancer. *Radiother Oncol*, 52:29-34, 1999.

[17] Chen QS Weinhous MS Deibel FC et al. Fluoroscopic study of tumor motion due to breathing: Facilitating precise radiation therapy for lung cancer patients. *Med Phys*, 28:1850-1856, 2001.

[18] Christensen GE Carlson B Chao KS et al. Image-based dose planning of intracavitary brachytherapy: Registration of serial-imaging studies using deformable anatomic templates. *Int J Radiat Oncol Biol Phys*, 51:227-243, 2001.

[19] Davies SC Hill AL Holmes RB et al. Ultrasound quantification of respiratory organ motion in the upper abdomen. *Br J Radiol*, 67:1096-1102, 1994.

[20] Dawson LA Balter J. Interventions to reduce organ motion effects in radiation delivery. *Semin Radiat Oncol*, 14(1):76-80, 2004.

[21] Dawson LA Litzenberg DW Brock KK et al. A comparison of ventilatory prostate movement in four treatment position. *Int J Radiat Oncol Biol Phys*, 48:319-323, 2000.

[22] Dawson LA Brock KK Kazanjian S et al. The reproducibility of organ position using active breathing control (ABC) during liver radiotherapy. *Int J Radiat Oncol Biol Phys*, 51:1410-1421, 2001.

[23] De Boer HC van Sornsen de Koste JR Senan S et al. Analysis and reduction of 3D systematic and random setup errors during the simulation and treatment of lung cancer patients with CT-based external beam radiotherapy dose planning. *Int J Radiat Oncol Biol Phys*, 49:857-868, 2001.

[24] De Neve W Van den Heuvel F De Beukeleer M et al. Routine clinical on-line portal imaging followed by immediate field adjustment using a tele-controlled patient couch. *Radiother Oncol*, 24:45-54, 1992.

[25] Dhanantwari AC Stergiopoulos S Iakovidis I. Correcting organ motion artifacts in x-ray CT medical imaging systems by adaptive processing. I. Theory. *Med Phys*, 28:1562-1576, 2001.

[26] Dhanantwari AC Stergiopoulos S Zamboglou N et al. Correcting organ motion artifacts in x-ray CT systems based on tracking of motion phase by the spatial overlap correlator. II. Experimental study. *Med Phys*, 28:1577-1596, 2001.

[27] DiBiase SJ Hosseinzadeh K Gullapalli RP et al. Magnetic resonance spectroscopic imaging-guided brachytherapy for localized prostate cancer. *Int J Radiat Oncol Biol Phys*, 52:429-438, 2002.

[28] Dieterich S Tang J Rodgers J et al. Skin respiratory motion tracking for stereotactic radiosurgery using the CyberKnife. *Computer Assisted Radiology and Surgery*, 130-136, 2003.

[29] Ding M Li J Deng J et al. Dose correlation for thoracic motion in radiation therapy of breast cancer. *Med Phys*, 30:2520-2529, 2003.

[30] Ekberg L Holmberg O Wittgren L et al. What margins should be added to the clinical target volume in radiotherapy treatment planning for lung cancer? *Radiother Oncol*, 48:71-77, 1998.

[31] Engelsman M Damen E De Jaeger K et al. The effect of breathing and set-up errors on the cumulative dose to a lung tumor. *Radiother Oncol*, 60:95-105, 2001.

[32] Ford EC Mageras GS Yorke E et al. Respiration-correlated spiral CT: A method of measuring respiratory-induced anatomic motion for radiation treatment planning. *Med Phys*, 30:88-97, 2003.

[33] Ford EC Mageras GS Yorke E et al. Evaluation of respiratory movement during gated radiotherapy using film and electronic portal imaging. *Int J Radiat Oncol Biol Phys*, 52:522-531, 2002.

[34] Gagné IM Robinson DM. The impact of tumor motion upon CT image integrity and target delineation. *Med Phys*, 31:3378-3392, 2004.

[35] Giraud P Elles S Helfre S et al. Conformal radiotherapy for lung cancer: different delineation of the gross tumor volume (GTV) by radiologists and radiation oncologists. *Radiother Oncol*, 62(1):27-36, 2002.

[36] Giraud P De Rycke Y Dubray B et al. Conformal radiotherapy (CRT) planning for lung cancer: Analysis of intrathoracic organ motion during extreme phases of breathing. *Int J Radiat Oncol Biol Phys*, 51:1081-1092, 2001.

[37] Hanley J Debois MM Mah D et al. Deep inspiration breath-hold technique for lung tumors: The potential value of target immobilization and reduced lung density in dose escalation. *Int J Radiat Oncol Biol Phys*, 45:603-611, 1999.

[38] Hector C Webb S Evans P. A simulation of the effects of set-up error and changes in breast volume on conventional and intensity-modulated treatments in breast radiotherapy. *Phys Med Biol*, 46(5):1451-1471, 2001.

[39] Hector C Webb S Evans P. The dosimetric consequences of inter-fractional patient movement on conventional and intensity-modulated breast radiotherapy treatments. *Radiother Oncol*, 54(1):57-64, 2000.

[40] Herfarth KK Debus J Lohr F et al. Extracranial stereotactic radiation therapy: set-up accuracy of patients treated for liver metastases. *Int. J. Radiation Oncology Biol. Phys.*, 46:329-335, 2000.

[41] Hernando ML Marks LB Bentel GC et al. Radiation-induced pulmonary toxicity: a dose-volume histogram analysis in 201 patients with lung cancer. *Int J Radiat Oncol Biol Phys*, 51:650-659, 2001.

[42] Hill DL Batchelor PG Holden M et al. Medical image registration. *Phys Med Biol*, 46:R1-45, 2001.

[43] Hof H Herfarth KK Münter M et al. Stereotactic single-dose radiotherapy of stage I nonsmall-cell lung cancer (NSCLC). *Int. J. Radiation Oncology Biol. Phys.*, 56:335-341, 2003.

[44] Hurkmans C Borger J Pieters B et al. Variability in target volume delineation on CT scans of the breast. *Int J Radiat Oncol Biol Phys*, 50(5):1366-1372, 2001.

[45] Hurkmans C Remeijer P Lebesque J Mijnheer B. Set-up verification using portal imaging; review of current clinical practice. *Radiother Oncol*, 58(2):105-120, 2001.

[46] ICRU Report 50. International Commission on Radiation Units and Measurements. Prescribing, recording and reporting photon beam therapy. 1993.

[47] ICRU Report 62. International Commission on Radiation Units and Measurements. Prescribing, recording and reporting photon beam therapy. Supplement to ICRU Report 50. 1999.

[48] Jaffray DA Drake DG Moreau M et al. A radiographic and tomographic imaging system integrated into a medical linear accelerator for localization of bone and soft-tissue targets. *Int J Radiat Oncol Biol Phys*, 45:773-789, 1999.

[49] Jiang SB Pope C Al Jarrah K et al. An experimental investigation on intra-fractional organ motion effects in lung IMRT treatments. *Phys Med Biol*, 48:1773-1784, 2003.

[50] Kak AC Slaney M. *Principles of Computerized Tomographic Imaging.* Edited by R. Cotellessa, IEEE, New York, 1988.

[51] Keall P Mageras GS Balter J et al. The management of respiratory motion in radiation oncology. *Report of AAPM Task Group 76 of the Radiation Therapy Committee.*

[52] Keall PJ Kini VR Vedam S et al. Motion adaptive x-ray therapy: a feasibility study. *Phys Med Biol*, 46:1-10, 2000.

[53] Keall PJ Starkschall G Shukla H et al. Acquiring 4D thoracic CT scans using a multislice helical method. *Phys Med Biol*, 49:2053-2067, 2004.

[54] Keall PJ. 4-dimensional computed tomography imaging and treatment planning. *Semin Radiat Oncol*, 14:81-90, 2004.

[55] Keall PJ Siebers JV Joshi S et al. Monte Carlo as a four-dimensional radiotherapy treatment-planning tool to account for respiratory motion. *Phys Med Biol*, 49:3639-3648, 2004.

[56] Kim DJW Murray BR Halperin R et al. Held-breath self-gating technique for radiotherapy of non-small-cell lung cancer: a feasibility study. *Int J Radiat Oncol Biol Phys*, 49:43-49, 2001.

[57] Kini VR Vedam SS Keall PJ et al. Patient training in respiratory-gated radiotherapy. *Med Dosim*, 28:7-11, 2003.

[58] Kitamura K Shirato H Shimizu S et al. Registration accuracy and possible migration of internal fiducial gold marker implanted in prostate and liver treated with real-time tumor-tracking radiation therapy (RTRT). *Radiother Oncol*, 62:275-281, 2002.

[59] Korin HW Ehman RL Riederer SJ et al. Respiratory kinematics of the upper abdominal organs: A quantitative study. *Magn Reson Med*, 23:172-178, 1992.

[60] Kubo HD Hill BC. Respiration gated radiotherapy treatment: A technical study. *Phys Med Biol*, 41:83-91, 1996.

[61] Kubo HD Len PM Minohara S et al. Breathing-synchronized radiotherapy program at the University of California Davis Cancer Center. *Med Phys*, 27:346-353, 2000.

[62] Langen K Jones D. Organ motion and its management. *Int J Radiat Oncol Biol Phys*, 50(1):265-278, 2001.

[63] Lattanzi J McNeeley S Pinover W et al. A comparison of daily CT localization to a daily ultrasound-based system in prostate cancer. *Int J Radiat Oncol Biol Phys*, 43:719-725, 1999.

[64] Lax I Blomgren H Larson D et al. Extracranial stereotactic radiosurgery of localized targets. *J Radiosurg*, 1:135-148, 1998.

[65] Levitt SH Khan FM. The rush to judgment: Does the evidence support the enthusiasm over three-dimensional conformal radiation therapy and dose escalation in the treatment of prostate cancer? *Int J Radiat Oncol Biol Phys*, 51:871-879, 2001.

[66] Li JG Xing L. Inverse planning incorporating organ motion. *Med Phys*, 27:1573-1578, 2000.

[67] Lorin S Grusell E Tilly N et al. Development of a compact proton scanning system in Uppsala with a moveable second magnet. *Phys Med Biol*, 45:1151-1163, 2000.

[68] Low DA Nystrom M Kalinin E et al. A method for the reconstruction of four-dimensional synchronized CT scans acquired during free breathing. *Med Phys*, 30:1254-1263, 2003.

[69] Lu W Mackie TR. Tomographic motion detection and correction directly in sinogram space. *Phys Med Biol*, 47:1267-1284, 2002.

[70] Lu W Parikh PJ El Naqa IM et al. Quantitation of the reconstruction quality of a four-dimensional computed tomography process for lung cancer patients. *Med Phys*, 32:890-901, 2005.

[71] Lu W Oliveira GH Mackie TR. Motion-encoded dose calculation through fluence/sinogram modification. *Med Phys*, 32:118-127, 2005.

[72] Lujan AE Balter JM Ten Haken RK. A method for incorporating organ motion due to breathing into 3D dose calculations in the liver: sensitivity to variations in motion. *Med Phys*, 30:2643-2649, 2003.

[73] Lujan AE Larsen EW Balter JM et al. A method for incorporating organ motion due to breathing into 3D dose calculations. *Med Phys*, 26:715-720, 1999.

[74] Mackie TR Kapatoes J Ruchala K et al. Image guidance for precise conformal radiotherapy. *Int J Radiat Oncol Biol Phys*, 56:89-105, 2003.

[75] Mageras GS Yorke E. Deep inspiration breath hold and respiratory gating strategies for reducing organ motion in radiation treatment. *Semin Radiat Oncol*, 14(1):65-75, 2004.

[76] Mageras GS Kutcher GJ Leibel SA et al. A method of incorporating organ motion uncertainties into three-dimensional conformal treatment plans. *Int J Radiat Oncol Biol Phys*, 35:333-342, 1996.

[77] Mageras GS Yorke E Rosenzweig K et al. Fluoroscopic evaluation of diaphragmatic motion reduction with a respiratory gated radiotherapy system. *J Applied Clin Med Phys*, 2:191-200, 2001.

[78] Mageras GS Fuks Z Leibel SA et al. Computerized design of target margins for treatment uncertainties in conformal radiotherapy. *Int J Radiat Oncol Biol Phys*, 43:437-445, 1999.

[79] Malone S Crook JM Kendal WS et al. Respiratory-induced prostate motion: Quantification and characterization. *Int J Radiat Oncol Biol Phys*, 48:105-109, 2000.

[80] Manning MA Wu Q Cardinale RM et al. The effect of setup uncertainty on normal tissue sparing with IMRT for head-and-neck cancer. *Int J Radiat Oncol Biol Phys*, 51:1400-1409, 2001.

[81] Martinez AA Yan D Lockman D et al. Improvement in dose escalation using the process of adaptive radiotherapy combined with three-dimensional conformal or intensity-modulated beams for prostate cancer. *Int J Radiat Oncol Biol Phys*, 50:1226-1234, 2001.

[82] McCarter SD Beckham WA. Evaluation of the validity of a convolution method for incorporating tumor movement and set-up variations into the radiotherapy treatment planning system. *Phys Med Biol*, 45:923-931, 2000.

[83] McKenzie AL. How should breathing motion be combined with other errors when drawing margins around clinical target volumes. *Br J Radiol*, 73:973-977, 2000.

[84] Medin PM Solberg TD De Salles A et al. Investigation of a minimally invasive method for treatment of spinal malignancies with linac stereotactic radiation therapy: Accuracy and animal studies. *Int J Radiat Oncol Biol Phys*, 52:1111-1122, 2002.

[85] Mehta M Scrimger R Mackie R. A new approach to dose escalation in non-small-cell lung cancer. *Int J Radiat Oncol Biol Phys*, 49:23-33, 2001.

[86] Minohara S Kanai T Endo M et al. Respiratory gated irradiation system for heavy-ion radiotherapy. *Int J Radiat Oncol Biol Phys*, 47:1097-1103, 2000.

[87] Miralbell R Nouet P Rouzaud M et al. Radiotherapy of bladder cancer: Relevance of bladder volume changes in planning boost treatment. *Int J Radiat Oncol Biol Phys*, 41:741-746, 1998.

[88] Murphy MJ Adler JR Bodduluri M et al. Image-guided radiosurgery for the spine and pancreas. *Comp Aided Surg*, 5:278-288, 2000.

[89] Murphy MJ. Tracking moving organs in real time. *Semin Radiat Oncol*, 14:91-100, 2004.

[90] Murphy MJ Chang S Gibbs I et al. Image-guided radiosurgery in the treatment of spinal metastases. *Neurosurg Focus*, 11:1-7, 2001.

[91] Mutic S Dempsey JF Bosch WR et al. Multimodality image registration quality assurance for conformal three-dimensional treatment planning. *Int J Radiat Oncol Biol Phys*, 51:255-260, 2001.

[92] Nederveen A Lagendijk J Hofman P. Detection of fiducial gold markers for automatic on-line megavoltage position verification using a marker extraction kernel (MEK). *Int J Radiat Oncol Biol Phys*, 47:1435-1442, 2000.

[93] Negoro Y Nagata Y Aoki T et al. The effectiveness of an immobilization device in conformal radiotherapy for lung tumor: reduction of respiratory tumor movement and evaluation of the daily setup accuracy. *Int J Radiat Oncol Biol Phys*, 50:889-898, 2001.

[94] Neicu T Shirato H Seppenwoolde Y et al. Synchronized moving aperture radiation therapy (SMART): Average tumour trajectory for lung patients. *Phys Med Biol*, 48:587-598, 2003.

[95] Northern Digital Inc. 103 Randall Drive, Waterloo, Ontario N2V 1C5, Canada. *http://www.ndigital.com*

[96] Ohara K Okumura T Akisada M et al. Irradiation synchronized with respiration gate. *Int J Radiat Oncol Biol Phys*, 17:853-857, 1989.

[97] Onishi H Kuriyama K Komiyama T et al. A new irradiation system for lung cancer combining linear accelerator, computed tomography, patient self-breathholding, and patient-directed beam-control without respiratory monitoring devices. *Int J Radiat Oncol Biol Phys*, 56:14-20, 2003.

[98] Ozhasoglu C Murphy MJ. Issues in respiratory motion compensation during external-beam radiotherapy. *Int J Radiat Oncol Biol Phys*, 52:1389-1399, 2002.

[99] Pan T Lee TY Rietzel E et al. 4D-CT imaging of a volume influenced by respiratory motion on multi-slice CT. *Med Phys*, 31:333-340, 2004.

[100] Pan T. Comparison of helican and ciné acquisitions for 4D-CT imaging with multislice CT. *Med Phys*, 32:627-634, 2005.

[101] Pemler P Besserer J Lombriser N et al. Influence of respiration-induced organ motion on dose distributions in treatments using enhanced dynamic wedges. *Med Phys*, 28:2234-2240, 2001.

[102] Pirzkall A McNight TR Graves EE et al. MR-spectroscopy guided target delineation for high-grade gliomas. *Int J Radiat Oncol Biol Phys*, 50:915-928, 2001.

[103] Pisani L Lockman D Jaffray D et al. Setup error in radiotherapy: On-line correction using electronic kilovoltage and megavoltage radiographs. *Int J Radiat Oncol Biol Phys*, 47:825-839, 2000.

[104] Purdy JA. Current ICRU definitions of volumes: limitations and future directions. *Semin Radiat Oncol*, 14(1):27-40, 2004.

[105] Ramsey CR Arwood D Scaperoth D et al. Clinical application of digitally-reconstructed radiographs generated from magnetic resonance imaging for intracranial lesions. *Int J Radiat Oncol Biol Phys*, 45:797-802, 1999.

[106] Remeijer P Geerlof E Ploeger L et al. 3-D portal image analysis in clinical practice: An evaluation of 2-D and 3-D analysis techniques as applied to 30 prostate cancer patients. *Int J Radiat Oncol Biol Phys*, 46:1281-1290, 2000.

[107] Remouchamps VM Letts N Vicini F et al. Initial clinical experience with moderate deep inspiration breath hold using an active breathing control (ABC) device in the treatment of patients with left-sided breast cancer using external beam irradiation. *Int J Radiat Oncol Biol Phys*, 56:704-715, 2003.

[108] Rietzel E Pan T Chen GTY et al. Four-dimensional computed tomography: Image formation and clinical protocol. *Med Phys*, 32:874-889, 2005.

[109] Ritchie CJ Hseih J Gard MF et al. Predictive respiratory gating: A new method to reduce motion artifacts on CT scans. *Radiology*, 190:847-852, 1994.

[110] Ritchie CJ Godwin JD Crawford CR et al. Minimum scan speeds for suppression of motion artifacts in CT. *Radiology*, 185:37-42, 1992.

[111] Ross CS Hussey DH Pennington EC et al. Analysis of movement of intrathoracic neoplasms using ultrafast computerized tomography. *Int J Radiat Oncol Biol Phys*, 18:671-677, 1990.

[112] Rosenzweig KE Hanley J Mah D et al. The deep inspiration breath hold technique in the treatment of inoperable non-small cell lung cancer. *Int J Radiat Oncol Biol Phys*, 48:81-87, 2000.

[113] Ruchala KJ Olivera GH Kapatoes JM et al. Megavoltage CT image reconstruction during tomotherapy treatments. *Phys Med Biol*, 45:3545-3562, 2000.

[114] Samson MJ van Sornsen de Koste JR de Boer HCJ et al. An analysis of anatomic landmark mobility and setup deviations in radiotherapy for lung cancer. *Int J Radiat Oncol Biol Phys*, 43:827-832, 1999.

[115] Schwartz LH Richaud J Buffat L et al. Kidney mobility during respiration. *Radiother Oncol*, 32:84-86, 1994.

[116] Schweikard A Glosser G Bodduluri M et al. Robotic motion compensation for respiratory movement during radiosurgery. *Comp Aided Surg*, 5:263-277, 2000.

[117] Seiler PG Blattmann H Kirsch S et al. A novel tracking technique for the continuous precise measurement of tumor positions in conformal radiotherapy. *Phys. Med. Biol.*, 45:N103-N110, 2000.

[118] Seppenwoolde Y Lebesque JV de Jaeger K et al. Comparing different NTCP models that predict the incidence of radiation pneumonitis. *Int J Radiat Oncol Biol Phys*, 55:724-735, 2003.

[119] Seppenwoolde Y Shirato H Kitamura K et al. Precise and real-time measurement of 3D tumor motion in lung due to breathing and heartbeat, measured during radiotherapy. *Int J Radiat Oncol Biol Phys*, 53:822-834, 2002.

[120] Seppi EJ Munro P Johnsen SW et al. Megavoltage cone-beam computed tomography using a high-efficiency image receptor. *Int J Radiat Oncol Biol Phys*, 55:793-803, 2003.

[121] Serago CF Chungbin SJ Buskirk SJ et al. Initial experience with ultrasound localization for positioning prostate cancer patients for external beam radiotherapy. *Int J Radiat Oncol Biol Phys*, 53:1130-1138, 2002.

[122] Sharp GC Jiang SB Shimizu S et al. Prediction of respiratory tumour motion for real-time image-guided radiotherapy. *Phys Med Biol*, 49:425-440, 2004.

[123] Sherouse G Novins KL Chaney EL. Computation of digitally reconstructed radiographs for use in radiotherapy. *Int J Radiat Oncol Biol Phys*, 18:651-658, 1990.

[124] Shimizu S Shirato H Kagei K et al. Impact of respiratory movement on the computed tomographic images of small lung tumors in three-dimensional (3D) radiotherapy. *Int J Radiat Oncol Biol Phys*, 46:1127-1133, 2000.

[125] Shimizu S Shirato H Kitamura K et al. Use of an implanted marker and real-time tracking of the marker for the positioning of prostate and bladder cancers. *Int J Radiat Oncol Biol Phys*, 48:1591-1597, 2000.

[126] Shimizu S Shirato H Ogura S et al. Detection of lung tumor movement in real-time tumor-tracking radiotherapy. *Int J Radiat Oncol Biol Phys*, 51:304-310, 2001.

[127] Shirato H Shimizu S Kunieda T et al. Physical aspects of a real-time tumor-tracking system for gated radiotherapy. *Int J Radiat Oncol Biol Phys*, 48:1187-1195, 2000.

[128] Siewerdsen JH Jaffray DA. Cone-beam computed tomography with a flat-panel imager: Magnitude and effects of x-ray scatter. *Med Phys*, 28:220-231, 2001.

[129] Sixel KE Aznar MC Ung YC et al. Deep inspiration breath hold to reduce irradiated heart volume in breast cancer patients. *Int J Radiat Oncol Biol Phys*, 49:199-204, 2001.

[130] Sonke JJ Zijp L Remeijer P et al. Respiratory correlated cone beam CT. *Med Phys*, 32:1176-1186, 2005.

[131] Stevens CW Munden RF Forster KM et al. Respiratory-driven lung tumor motion is independent of tumor size, tumor location, and pulmonary function. *Int J Radiat Oncol Biol Phys*, 51:62-68, 2001.

[132] Stromberg JS Sharpe MB Leonard HK et al. Active breathing control (ABC) for Hodgkins disease: reduction in normal tissue irradiation with deep inspiration and implications for treatment. *Int J Radiat Oncol Biol Phys*, 48:797-806, 2000.

[133] Stroom JC Koper PCM Korevaar GA et al. Internal organ motion in prostate cancer patients treated in prone and supine treatment position. *Radiother Oncol*, 51:237-248, 1999.

[134] Stroom JC Olofsen-van Acht MJJ Quint S et al. On-line setup corrections during radiotherapy of patients with gynecologic tumors. *Int J Radiat Oncol Biol Phys*, 46:499-506, 2000.

[135] Stroom JC de Boer HCJ Huizenga H et al. Inclusion of geometrical uncertainties in radiotherapy treatment planning by means of coverage probability. *Int J Radiat Oncol Biol Phys*, 43:905-919, 1999.

[136] Suramo I Päivänsalo M Myllylä V. Cranio-caudal movements of the liver, pancreas and kidneys in respiration. *Acta Radiol Diag*, 25:129-131, 1984.

[137] Swindell W Simpson RG Oleson JR. Computed tomography with a linear accelerator with radiotherapy applications. *Med Phys*, 10:416-420, 1983.

[138] Tai P Van Dyk J Yu E et al. Variability of target volume delineation in cervical esophageal cancer. *Int J Radiat Oncol Biol Phys*, 42:227-288, 1998.

[139] Turner SL Swindell R Bowl N et al. Bladder movement during radiation therapy for bladder cancer: Implications for treatment planning. *Int J Radiat Oncol Biol Phys*, 39:355-360, 1997.

[140] Uematsu M Shioda A Suda A et al. Intrafractional tumor position stability during computed tomography (CT)-guided frameless stereotactic radiation therapy for lung or liver cancers with a fusion of CT and linear accelerator (FOCAL) unit. *Int J Radiat Oncol Biol Phys*, 48:443-448, 2000.

[141] Uematsu M Shioda A Tahara K et al. Focal, high dose, and fractionated modified stereotactic radiation therapy for lung carcinoma patients: a preliminary experience. *Cancer*, 82:1062-1070, 1998.

[142] Underberg R Lagerwaard F Cuijpers J et al. Four-dimensional CT scans for treatment planning in stereotactic radiotherapy for stage I lung cancer. *Int J Radiat Oncol Biol Phys*, 60:1283-1290, 2004.

[143] Valicenti RK Sweet JW Hauck WW et al. Variation of clinical target volume definition in three-dimensional radiation therapy for prostate cancer. *Int J Radiat Oncol Biol Phys*, 44:931-935, 1999.

[144] Van de Steene J Linthout N de Mey J et al. Definition of gross tumor volume in lung cancer: inter-observer variability. *Radiother Oncol*, 62(1):37-49, 2002.

[145] Van Herk M Witte M van der Geer J et al. Biologic and physical fractionation effects of random geometric errors. *Int J Radiat Oncol Biol Phys*, 57:1460-1471, 2003.

[146] Van Herk M Remeijer P Rasch C et al. The probability of correct target dosage: Dose-population histograms for deriving treatment margins in radiotherapy. *Int J Radiat Oncol Biol Phys*, 47:1121-1135, 2000.

[147] Van Herk M Remeijer P Lebesque JV. Inclusion of geometric uncertainties in treatment plan evaluations. *Int J Radiat Oncol Biol Phys*, 52:1407-1422, 2002.

[148] van Sornsen de Koste JR Lagerwaard FJ Nijssen-Visser MR et al. Tumor location cannot predict the mobility of lung tumors: A 3D analysis of data generated from multiple CT scans. *Int J Radiat Oncol Biol Phys*, 56:348-354, 2003.

[149] van Sornsen de Koste JR Lagerwaard FJ Schuchhard-Schipper RH et al. Dosimetric consequences of tumor mobility in radiotherapy of stage I non-small cell lung cancer – an analysis of data generated using "slow" CT scans. *Radiother Oncol*, 61:93-99, 2001.

[150] Vedam SS Kini VR Keall PJ et al. Quantifying the predictability of diaphragm motion during respiration with a non-invasive external marker. *Med Phys*, 30:505-513, 2003.

[151] Vedam SS Keall PJ Docef A et al. Predicting respiratory motion for four-dimensional radiotherapy. *Med Phys*, 31:2274-2283, 2004.

[152] Vedam SS Keall PJ Kini VR, et al. Acquiring a four-dimensional computed tomography dataset using an external respiratory signal. *Phys Med Biol*, 48:45-62, 2003.

[153] Wagman R Yorke E Giraud P et al. Reproducibility of organ position with respiratory gating for liver tumors: Use in dose-escalation. *Int J Radiat Oncol Biol Phys*, 55:659-668, 2003.

[154] Wong JW Sharpe MB Jaffray DA et al. The use of active breathing control (ABC) to reduce margin for breathing motion. *Int J Radiat Oncol Biol Phys*, 44:911-919, 1999.

[155] Yan D Vicini F Wong J et al. Adaptive radiation therapy. *Phys Med Biol*, 42:123-132, 1997.

[156] Yan D Lockman D Brabbins D et al. An off-line strategy for constructing a patient-specific planning target volume in adaptive treatment process for prostate cancer. *Int J Radiat Oncol Biol Phys*, 48:289-302, 2000.

[157] Yan D Lockman D. Organ/patient geometric variation in external beam radiotherapy and its effects. *Med Phys*, 28:593-602, 2001.

[158] Yang JN Mackie TR Reckwerdt P et al. An investigation of tomotherapy beam delivery. *Med Phys*, 24:425-436, 1997.

[159] Yu CX Jaffray DA Wong JW. The effects of intra-fraction organ motion on the delivery of dynamic intensity modulation. *Phys Med Biol*, 43:91-104, 1998.

[160] Zelefsky MJ Crean D Mageras GS et al. Quantification and predictors of prostate position variability in 50 patients evaluated with multiple CT scans during conformal radiotherapy. *Radiother Oncol*, 50:225-234, 1999.

Index

List of Abbreviations

3D: Three-dimensional

3D CRT: Three-dimensional conformal radiation therapy

4D CT: Four-dimensional computed tomography

4D RT: Four-dimensional radiotherapy

ABC: Active breathing control

AP: Anterior-posterior

BP: Backprojection

CT: Computed tomography

CTV: Clinical target volume

DIBH: Deep-inspiration breath hold

DRR: Digitally reconstructed radiograph

EPID: Electronic portal imaging detector

FBP: Filtered backprojection

GTV: Gross tumor volume

ICRU: International Commission on Radiation Units and Measurements

IM: Internal margin

IMRT: Intensity-modulated radiation therapy

kVCT: Kilovoltage CT

mDIBH: Moderate deep-inspiration breath hold

MLC: Multileaf collimator

MRI: Magnetic resonance imaging

MVCT: Megavoltage CT

NDI: Northern Digital Inc.

PDF: Probability density function

PET: Positron emission tomography

PTV: Planning target volume

RL: Right-left

RPM: Varian's real-time position management respiratory gating system

RTRT: Real Time Tumor-Tracking Radiation Therapy

SD: Standard deviation

SI: Superior-inferior

SM: Setup margin

SRT: Stereotactic radiation therapy

TCP: Tumor control probability

TVO: Total volume occupied